UNIVERSITAT DE BARCELONA

Microphysiological Systems for the Evaluation of Biomaterials in Regenerative Therapies

Adrián López Canosa

PhD thesis

Microphysiological Systems for the Evaluation of Biomaterials in Regenerative Therapies

Author

Adrián López Canosa

Directors

Prof. Elisabeth Engel López

Dr. Oscar Castaño Linares

UNIVERSITAT DE BARCELONA

Microphysiological Systems for the Evaluation of Biomaterials in Regenerative Therapies

Memòria presentada per optar al grau de doctor per la Universitat de Barcelona

Programa de doctorat en Biomedicina

Autor

Adrián López Canosa

Directors

Prof. Elisabeth Engel López

Dr. Oscar Castaño Linares

Tutor

Prof. Josep Samitier Martí

Institut de Bioenginyeria de Catalunya

Universitat de Barcelona – Facultat de Física, Departament d'Enginyeria Electrònica i Biomèdica

UNIVERSITAT DE BARCELONA

Abstract

The design of bioresponsive materials capable of stimulating the body's innate regenerative potential is opening unprecedented possibilities to treat tissue and organ failure, which is one of the most important burdens of healthcare systems worldwide. Unfortunately, their development is hampered by the lack of adequate preclinical models, which are essential in the successful transition of a biomaterial to the clinical trials phase. Most of the experiments rely on animal models, which usually fail to predict the material interactions with the human body, as they are unable to recapitulate the complexities of our physiology. During the last decades, the advancements in the field of microtechnology have allowed to create advanced cell culture systems capable of replicating tissue and organ-level physiology by mimicking relevant conditions such as cell organization or microenvironmental cues. These platforms, known as microphysiological systems (MPS), have shown in different studies their great potential in predicting mechanisms of action, safety, and efficacy of different drugs, attracting a lot of attention from the pharmaceutical industry and regulatory agencies.

However, few studies have explored the possibility of using microphysiological systems for the preclinical testing of biomaterials. The goal of this thesis is to fill this knowledge gap by developing microfluidic cell culture systems that allow to reliably predict the actual *in vivo* response of different materials. One of the proposed platforms is aimed at assessing the potential of a biomaterial to stimulate endothelial progenitor cell recruitment in a bone tissue microenvironment. This is a critical step in the neovascularization and bone regeneration process that has not been properly studied due to the lack of adequate models. The proposed device allowed to identify the role of calcium ions in stimulating the recruitment of rat endothelial progenitor cells (rEPC) to the site of injury, which is mediated by an increase in the release of osteopontin, a chemotactic and mitogenic protein produced by rat bone-marrow mesenchymal stromal cells (BM-rMSC). The platform was also used to evaluate a calcium-releasing biomaterial based on electrospun polylactic acid (PLA) fibers with calcium-phosphate (CaP) nanoparticles. The results show a significant increase in terms of rEPC recruitment and the release of osteopontin and other pro-angiogenic and inflammatory proteins by BM-rMSC with respect to a regular PLA control, which is in close agreement with previous experiments performed in a murine *in vivo* model.

The other platform proposed in this thesis is aimed at providing a physiologically relevant model of cardiac tissue to study a myocardial ischemia-reperfusion injury. There are currently no

reliable *in vitro* models to mimic this disease, making these contributions extremely relevant for cardiac regeneration studies. A first prototype of the platform based on the combination of aligned electrospun PLA fibers with a user-friendly electrical stimulation setup in a microfluidic cell culture platform produced a biomimetic cardiac tissue in 2D. This was confirmed by the high anisotropy of the tissue constructs, based on the co-culture of neonatal mouse cardiomyocytes with cardiac fibroblasts, as well as the upregulation of several key cardiac markers such as contractile and structural proteins. In order to make the model more physiologically relevant, a second device was developed to obtain human-derived 3D tissues. This platform is based on the self-assembling of primary cardiac fibroblasts (hCF) co-cultured with human pluripotent stem cell-derived cardiomyocytes (hPSC-CM) in a fibrin-based hydrogel around two microposts structures, which exert a passive mechanical tension that stimulates tissue maturation and cell alignment. We first performed a screening using 2D assays based on hPSC-CM monolayers to select the best environmental conditions to mimic an ischemia-reperfusion injury. We then characterized the response of the human-derived cardiac organoids to an ischemia-reperfusion injury, consisting of an 8 h culture period at 0 % oxygen in an ischemic solution that replicates the acidic and hyperkalemic conditions observed *in vivo,* followed by a refreshment with fully supplemented cell media and recovery of 21 % environmental oxygen concentrations. We observed a drastic increase in cell death by necrosis and apoptosis as well as a strong fibrotic response, characterized by an increase in hCF proliferation, differentiation towards myofibroblasts and collagen I deposition. Taken together, we believe that the platforms developed in this thesis constitute an extremely valuable and versatile tool to perform preclinical studies, offering a promising alternative to animal studies for the development of new biomaterials and drug discovery.

Table of contents

List of figures and tables

List of abbreviations

2D: two dimensional

3D: three dimensional

ADME: absorption, distribution, metabolism, and excretion

ANG: angiotensin

ATP: adenosine triphosphate

bFGF: basic fibroblast growth factor

BMP: bone morphogenetic protein

BM-rMSC: bone marrow rat mesenchymal stromal cells

BrdU: bromodeoxyuridine

β-TCP: beta-tricalcium phosphate

CAD: computer aided design

CaP: calcium phosphates

CM: cardiomyocytes

CRISPR-Cas9: clustered regularly interspaced short palindromic repeats associated with protein 9

Cx-43: connexin 43

DNA: deoxyribonucleic acid

EC: endothelial cells

ECM: extracellular matrix

ESC: embryonic stem cells

FITC: fluorescein isothiocyanate

HIF: hypoxia inducible factor

HuDMEC: human dermal microvascular endothelial cells

HUVEC: human umbilical vein endothelial cells

IL: interleukin

iPSC: induced pluripotent stem cells

IRI: ischemia-reperfusion injury

ISO: international organization for standardization

LDH: lactate dehydrogenase

LV: left ventricle

MHC: myosin heavy chain

MI: myocardial infarction

miRNA: micro ribonucleic acid

MLC: myosin light chain

MPS: microphysiological system

MRI: magnetic resonance imaging

MTT: 3-(4,5-dimethylthiazol-2-yl)-2,5-diphenyltetrazolium bromide

NMR: nuclear magnetic resonance

PCL: polycaprolactone

PCR: polymerase chain reaction

PDMS: polydimethylsiloxane

PEG: polyethylene glycol

PLA: polylactic acid

PLLA: poly(L-lactide) acid

rEPC: rat endothelial progenitor cells

RGD: arginine-glycine-aspartic acid

RNA: ribonucleic acid

ROS: reactive oxygen species

S1P: sphingosine-1-phosphate

SEM: scanning electron microscopy

siRNA: small interfering ribonucleic acid

TGF-β: transforming growth factor beta

TMRM: tetramethyl-rhodamine methyl ester

TNF-α: tumour necrosis factor alfa

TTC: triphenyl tetrazolium chloride

VEGF: vascular endothelial growth factor

vWF: von Willebrand factor

ZO-1: zonula occludens 1

1

General Objectives

1.1 Motivation and objectives

The significant progress made during the last decades in biomedical engineering, a discipline that applies the principles of engineering to medicine and biology to provide technological solutions for the diagnosis, monitoring, and therapy of human health conditions, is drastically changing the paradigm of how medicine is practiced. The development of materials for medical applications has greatly broadened the possibilities to treat organ and tissue failure. Substitute heart valves, hip prosthesis, or vascular stents have made their way into common clinical practice, saving the lives of millions of patients worldwide. The design of smart materials capable of interacting with the human body to trigger innate regenerative pathways is gaining a lot of momentum in the last years [1] as it allows to stimulate tissue repair in a safer and more cost-effective way than generating artificial tissues for implantation, which also poses additional regulatory challenges [2]. However, a successful translation of the designed materials from the lab to the clinic is generally hampered by the lack of reliable models of the human physiology during preclinical development [3].

The conventional cell culture assays traditionally used in a laboratory environment are unable to recapitulate many critical characteristics of real tissues. One of the most important ones is the lack of a dynamic environment, which hampers the study of how different stimuli such as shear stress, substrate stiffness or cyclical mechanical deformations affect tissue development and function [4]. Therefore, animal experiments are still required to obtain data that can be reliably extrapolated to humans. However, these assays have many drawbacks that limit their applicability, such as their really high cost, the important differences with humans (genetic, metabolic, and physiological) and the ethical concerns related to the use of animals [5]. Fortunately, during the last decades, the advancements in micro- and nanotechnology have allowed to create advanced cell culture platforms in which the different cues affecting tissue

development can be readily modelled. These devices, known as microphysiological systems or organs-on-chip, are based on the use microfluidic technology to precisely control the physicochemical cell microenvironment, including shear stress, chemical gradients, strain, etc. [6]. These models have attracted a lot of attention from the pharmaceutical and biotechnological industries, as they offer a promising alternative to reduce animal experimentation, not only for the unprecedented level of control over microenvironmental cues but also for their high-throughput capabilities and cost-effectiveness, as the amount of required reagents such as cells, culture media or drugs is drastically reduced [7]. Moreover, the combination of these systems with the latest advancements in cell biology such as induced pluripotent stem cells, opens the door to the creation of highly personalized pathological models to study regenerative therapies.

The main goal of this doctoral thesis is the creation of microphysiological models to evaluate regenerative strategies based on the use of instructive biomaterials, with a special focus on the study of bone-tissue vascularization and myocardial ischemia-reperfusion injury. To meet this goal, the following sub-objectives must be addressed:

- Design and fabrication of microfluidic cell culture devices using computer-aided design technologies and standard microfabrication processes.
- Simulation of the devices by finite element analysis and experimental validation of the results in order to obtain a reliable computational model of the system that could be used to optimize the design and the range of experimental conditions.
- Generation of the cellular microenvironment to generate a highly biomimetic model of bone-tissue vascularization and myocardial ischemia-reperfusion injury by selecting the appropriate cells and supporting extracellular matrix to be cultured inside the microfluidic devices.

1.2 Dissertation outline

This doctoral thesis is divided into six chapters whose content is summarized below:

- The first chapter is the present one, in which we give a general background and explain the main motivations and objectives of this thesis, as well as a summary of each chapter.
- In the second chapter, we provide a general introduction to biomaterials and tissue engineering, with a detailed description of the *in situ* approach as well as the main strategies for bone and cardiac tissue regeneration. Current preclinical models to test biomaterials are also discussed and the concept of microphysiological systems is presented along with the state of the art of the field.

- In the third chapter, we describe a microphysiological system to study the potential of calcium-releasing materials biomaterials to recruit endothelial progenitor cells, a critical step of the vascularization process in a bone tissue microenvironment. The effect of calcium ions in the proliferation and migration of rat endothelial progenitor cells (rEPC) and mesenchymal stromal cells (BM-rMSC) derived from the bone marrow was studied in both monoculture and co-culture conditions, as well as the role of osteopontin in mediating the recruitment of rEPC. A finite element model for the transport of this protein was created and experimentally validated to show that paracrine cell communication was taking place between both cell types in our device. As a proof of concept, the platform was used to study polylactic acid (PLA)-based biomaterials, showing that the incorporation of calcium phosphate nanoparticles stimulates rEPC recruitment and pro-angiogenic and pro-inflammatory cytokine release by BM-rMSC.

- In the fourth chapter, a microphysiological platform to obtain a highly biomimetic cardiac tissue model based on a combination of aligned electrospun nanofibers with a user-friendly electrical stimulation setup is presented. An experimentally validated 3D computational model of the electrical field shows that the platform can closely match the results obtained with the gold standard planar electrode technology using inexpensive rod-shaped biocompatible stainless-steel electrodes. The functionality of the platform was validated by co-culturing neonatal mouse cardiomyocytes with cardiac fibroblasts, resulting in a tissue with a high degree of anisotropy and significant upregulation of several key genes involved in conductive and structural cardiac properties.

- In the fifth chapter, a microphysiological model of cardiac ischemia-reperfusion injury (IRI) is described. The presented platform is based on the generation of 3D cardiac organoids by the self-assembling of human pluripotent stem cell-derived cardiomyocytes co-cultured with primary cardiac fibroblasts in a fibrin-based hydrogel around micropost structures. A preliminary screening using 2D monolayers of hPSC-CM was performed to select the best conditions to mimic the IRI in terms of environmental oxygen concentrations and media composition. The effects of the injury were assessed in the 3D cardiac tissues in terms of cell death and fibrotic response.

- The sixth chapter summarizes the overall contributions of this thesis, offering some general conclusions based on the results generated in the experimental work as well as future perspectives and improvements to continue with the work presented through this dissertation.

The research content of this doctoral thesis was carried out at the Biomaterials for Regenerative Therapies group of the Institute for Bioengineering of Catalonia (IBEC), under the supervision of Prof. Elisabeth Engel López and Dr. Oscar Castaño Linares. The author gratefully

acknowledges the Spanish Ministry of Education, Culture and Sport (MECD) for the financial support through the Formación de Profesorado Universitario program (FPU 2017/06161). The work included in the fifth chapter was performed at the Department for Applied Stem Cell Research of the University of Twente (UT, Enschede, The Netherlands) in collaboration with Prof. Robert Passier thanks to a FPU mobility grant awarded by the Spanish MECD.

1.3 References

[1] A. Persidis 1999 Tissue engineering *Nat. Biotechnol.* **17** 508–510.

[2] Gaharwar A K, Singh I, Khademhosseini A 2020 Engineered biomaterials for in situ tissue regeneration *Nat. Rev. Mater.* **5** 686–705.

[3] Pan E, Bogumil D, Cortessis V, Yu S, Nieva J 2020 A systematic review of the efficacy of preclinical models of lung cancer drugs *Front. Oncol.* **10** 591-610.

[4] Huh D, Hamilton G A, Ingber DE 2011 From 3D cell culture to organs-on-chips,*Trends Cell Biol.* **21** 745–754.

[5] Van Norman G A 2019 Limitations of animal studies for predicting toxicity in clinical trials: is it time to rethink our current approach? *JACC Basic to Transl. Sci.* **4** 845–854.

[6] Bhatia S N, Ingber D E 2014 Microfluidic organs-on-chips *Nat. Biotechnol.* **32** 760–772.

[7] Esch E W, Bahinski A, Huh D 2015 Organs-on-chips at the frontiers of drug discovery *Nat. Rev. Drug Discov.* **14** 248–260.

2

General Introduction

Tissue and organ failure caused by diseases, injuries or developmental defects has become one of the greatest economical and healthcare concerns [1]. Nowadays, the most common approach used in clinical practice to deal with these problems is to transplant a tissue or organ from a donor. However, this strategy cannot meet the current demands due to the aging of the general population, the lack of donors, and diverse logistic constraints related to organ transportation [2]. The emergence of tissue engineering during the last decades has provided a promising alternative to develop therapies and products for the repair or replacement of damaged tissue and organs [3]. First developments in this area were focused on the development of tissues for implantation (*ex vivo* approach) by combining the patient's own cells with a scaffold made with biomaterials, which are materials capable of interacting with biological systems to eventually form a tissue construct. This strategy has shown limited success due to many limiting factors such as the poor engraftment efficacy, high cost, immunogenicity and strict regulatory hurdles [4].

In order to overcome these problems, the concept of *in situ* or endogenous tissue engineering was developed, which is aimed at creating biomaterials or scaffolds capable of stimulating the innate regenerative programs of the human body [5]. One of the main limitations of the successful translation of these materials to the clinic is the high failure rates during clinical trials, which stem from the poor predictability of current preclinical studies [6]. Recent advancements in microfabrication have allowed to create innovative *in vitro* models known as microphysiological systems (MPS) or organs-on-a-chip (OoC) that are able to recapitulate tissue and organ level physiology to emulate the conditions of the actual human *in vivo* microenvironment [7]. Throughout this chapter, we will introduce the framework of tissue engineering and describe in detail the *in situ* approach, with a particular emphasis on its applications for bone vascularization and cardiac tissue regeneration. The second section of this chapter will be devoted to the introduction of preclinical testing of biomaterials, while the third and last section will give the reader an overview of the concept of MPS.

2.1 Introduction to biomaterials and tissue engineering

2.1.1 Traditional approach to tissue engineering

The scientific field devoted to the study of materials aimed at interacting with biological systems for a medical purpose, generally known as **biomaterials**, has come a long way since the first developments in the area (dating back to 1960). It has become a highly relevant field of study due to the increasing economical and healthcare concerns related to the shortage of organ donors and aging of the general population [8]. The traditional approach used in this disciple is known as ***ex vivo* tissue engineering**, which is based on the combination of biomaterials with cells and biomolecules outside the body to obtain a tissue construct for implantation [9,10]. The main elements needed in this approach are thus the following (see **Fig.1**):

- **Cells:** the different types of cell sources used to create the tissue constructs can be obtained from a small biopsy. These include embryonic stem cells (ESC), which are derived from discarded human embryos, human induced pluripotent stem cells (hiPSC), derived by genetic reprogramming of somatic cells, and autologous or allogeneic adult tissue stem cells [11]. The first two types are pluripotent and can give rise to any cell lineage in the body, while the latter are multipotent (can give rise to a limited set of cell types).

- **Scaffold:** this term refers to the biomaterial that constitutes the three-dimensional structure of the tissue. It provides the biophysical and biochemical properties to provide integrity and support, as well as signals capable of driving cell fate such as surface topography or growth factors [12]. They can be made of different materials (such as polymers, ceramics, metals or composites) of synthetic or natural origin (or a combination of both sources) in different conformations, ranging from hydrogels to fibrous scaffolds or nanoparticles using a variety of fabrication technologies [13]. One of the most commonly used is the electrospinning technique, which is based on the use of electrical forces to draw charged threads of polymer solutions to a collector in order to obtain a fibrous scaffold [14]; another one is 3D printing, which is a process to deposit inks (polymers, cells, or combination of the two) in predefined patterns in a layer-by-layer approach to create a three-dimensional structure [15].

2.1.2 *In situ* approach to tissue engineering

The classical tissue engineering framework has many drawbacks, such as its high cost, the need for compatible cell sources that do not elicit an immune reaction in the patient, complex culture conditions or the poor homing and engraftment efficacy of the implants [16]. This motivated the development of a new approach known as ***in situ* tissue engineering**, which is based on the use of bioresponsive materials that can stimulate the body's innate regenerative potential. This strategy eliminates the need for harvested cells, which drastically reduces costs

and regulatory issues. Scalability, reproducibility, and shelf life of the implants are also much higher [5].

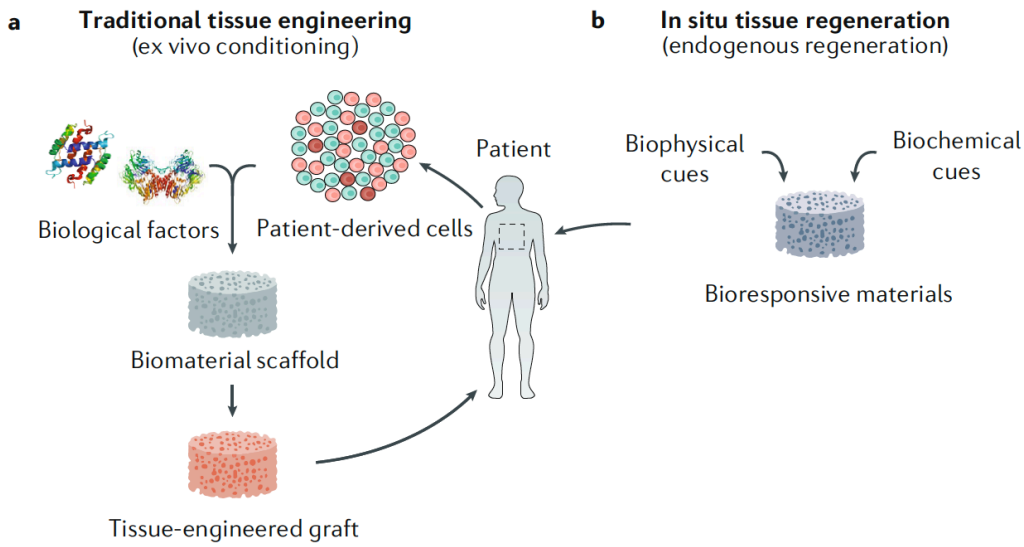

Figure 1 Comparison of the two main strategies in tissue engineering. (a) Traditional *ex vivo* approach using scaffolds pre-seeded with cells before implantation. **(b)** *In situ* approach based on the use of bioresponsive materials that are able to stimulate the own body's regenerative potential. *Adapted from [5].*

In order to better understand this tissue engineering strategy, it is important to understand how tissue regeneration works. It is a highly complex process involving mainly three different but overlapping steps: the first one is inflammation, which generally starts with the activation of tissue-resident macrophages due to the detection of wound- and pathogen-associated molecules. Shortly after this, circulating immune cells (such as neutrophils, monocytes, etc.) are recruited to the site of injury [17]. Depending on their role, these cells can be categorized as pro-inflammatory, when they are in charge of cleaning dead cells and infectious pathogens, or anti-inflammatory, when they lead to ECM remodeling and endogenous stem cell differentiation [18]. The second phase involves the migration and proliferation of endogenous progenitor and stem cells to the site of injury, which will orchestrate the replacement of the ECM by the deposition of new proteins and the formation of vascularized networks [19]. The final stage is tissue remodeling, which comprises the degradation, reorganization, and resynthesis of the incipient ECM into a newly formed tissue. In some adult tissues (such as cardiac tissue), the regenerative capacity is limited, and the final tissue is mainly composed of a non-functional collagen scar [20].

In the context of *in situ* tissue engineering, biomaterials have to interact with the cellular microenvironment in order to orchestrate the regeneration process. This can be achieved by two approaches. The first one involves **extracellular signalling,** which occurs by means of the biophysical and biochemical properties of the materials [5]. In the first category, one of the most important parameters to take into account is the stiffness of the material, as it has been shown to

influence a wide range of parameters such as cell attachment, migration, proliferation, differentiation or cytokine release [21]. These changes are driven by mechanotransduction phenomena mediated by transmembrane receptors (such as integrins) and cytoskeleton components (such as microfilaments) [22]. Other important biophysical parameters are also the microstructure or degradation products of the material [23]. Regarding the biochemical properties of the materials, they can be regulated by the incorporation of bioactive molecules such as cell-adhesion proteins (or the active peptides from these proteins) [24] or growth factors, such as human bone morphogenetic protein 2 (BMP-2) to induce osteogenesis [25] or vascular endothelial growth factor (VEGF) to stimulate angiogenesis [26,27]. The second approach used in the context of *in situ* tissue engineering is the **intracellular reprogramming,** which can be achieved using a range of different techniques such as the use of polymeric nanoparticles for the delivery of transcription factors [28] or RNA based therapeutics [29] or gene editing tools like the clustered regularly interspaced short palindromic repeats-associated protein 9 (CRISPR-Cas9) to activate or silence specific genes [30,31].

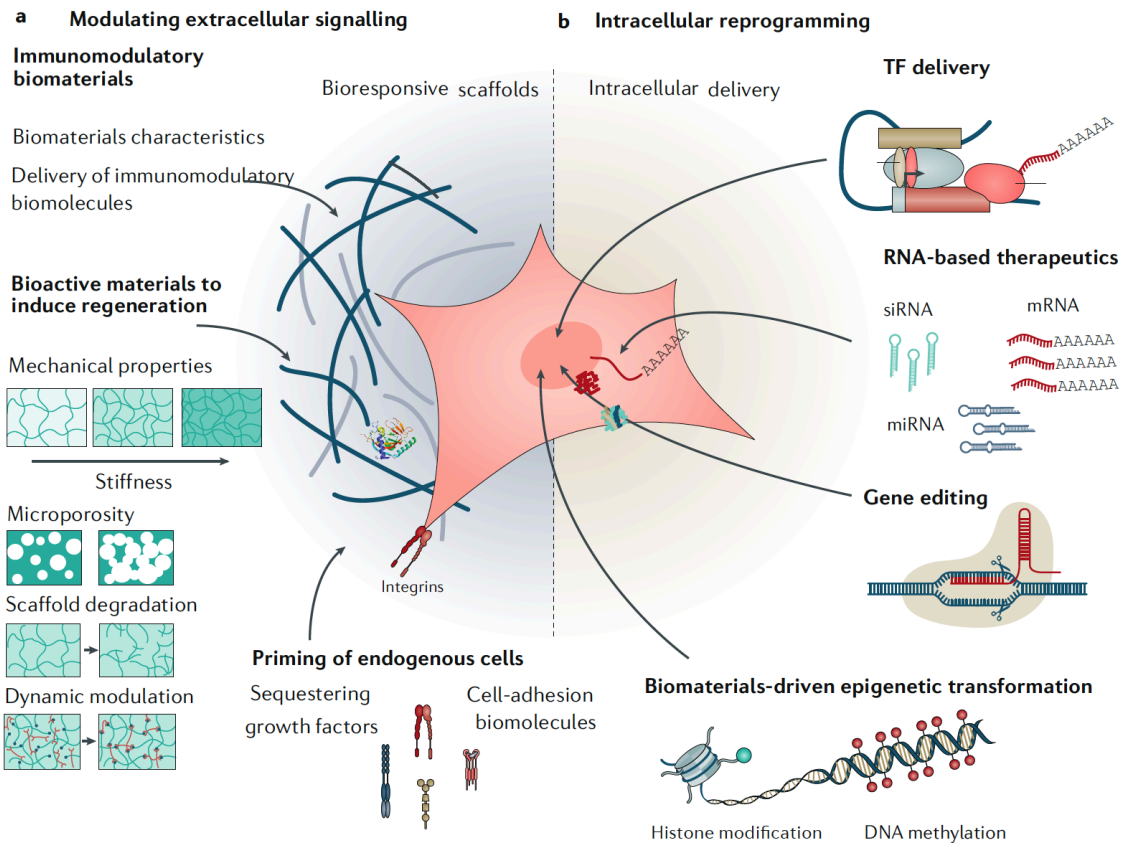

Figure 2 Strategies for *in situ* tissue regeneration. (a) Manipulation of the extracellular cell environment using biophysical (stiffness, porosity, degradation…) and biochemical cues (growth factors, adhesion sequences…) to stimulate endogenous progenitor cell migration and differentiation. **(b)** Intracellular reprogramming of endogenous progenitor cells using biomolecules to alter gene expression (transcription factors, RNA…). *Adapted from [5].*

2.1.3 Strategies for bone vascularization

The field of bone tissue engineering is focused on designing biomaterials that can be easily implanted in the bone defect and remodelled by the patient's own cells [32]. The most widely used biomaterials for bone-tissue engineering can be grouped into four categories:

- **Metals:** historically, they have been the materials most commonly used for bone implants due to their excellent mechanical properties. The surface of these materials is generally modified by mechanically creating a certain microtopography or performing chemical treatments in order to stimulate calcium phosphate deposition, which promotes implant integration with the host bone tissue and reduces inflammation [33,34]. The most widely used metals are titanium, magnesium and their alloys [35,36]. One of the main problems of metallic materials is related to their really high elastic modulus and monolithic structure, which prevents tissue ingrowth and can lead to stress shielding and bone reabsorption [37].

- **Polymers:** they are generally classified as naturally derived (such as collagen) or synthetic polymers. The main problems related to the use of natural polymers are their low mechanical strength and their high batch-to-batch compositional variability and potential immunogenicity, as they are extracted from living sources [38]. To overcome these issues, synthetic polymers can be used, which offer much more possibilities for chemical modifications, including the addition of cell-binding sites and metalloprotease-sensitive domains [39]. Some examples include poly (ε-caprolactone) (PCL) [40,41] or poly (L-lactic acid) (PLLA) [42,43].

- **Bioceramics:** the most widely used materials in this category are calcium phosphates because they mimic the inorganic phase of bone. Their most common presentations are hydroxyapatite (HAp) and *β*-tricalcium phosphate ceramics (β-TCP*)*, which are commonly injected as bone cements or used as implant coatings [44]. Another different type of material is bioactive glasses, which are generally made of silicates containing different elements such as calcium, phosphates, and borates [45].

- **Composites:** These materials are composed of a polymer phase, which can be modified with bioactive molecules such as adhesion sequences [46], with embedded nanoparticles, generally based on bioceramic materials such as calcium phosphates or silicates [47,48]. The addition of the particles enhances de overall mechanical and bioactive properties of the materials [49], which can be modulated by blending polymers with different degradation rates [50].

One of the strategies used to stimulate bone tissue vascularization is based on the tuning of biophysical material properties, such as the stiffness or the microstructure, which have been shown to play a central role in controlling cell migration and vascularization [51-53]. Degradation products from the material also have a huge influence on vascularization. For instance, the release

of bioactive ions by bioceramic materials resulting from their degradation (such as calcium) has been suggested to induce the recruitment of endothelial progenitor cells [54,55], while copper [56,57] and cobalt [58,59] ions have been shown to induce angiogenesis by stimulating hypoxia-related pathways and the overexpression of proteins such as the vascular endothelial growth factor (VEGF) or the basic fibroblast growth factor (bFGF). Regarding biochemical modifications of the scaffolds, there are several possibilities: one of them is to add bioactive peptides (such as RGD) to facilitate endothelial cell adhesion to the material and improve cell survival and proliferation [60,61]. Another option is to incorporate proteins closely involved in vascularization, such as growth factors, mainly VEGF [62,63], or anti-inflammatory cytokines, such as interleukin 4 (IL-4) [64]. Finally, it has also been shown that the use of miRNAs or siRNA to intracellularly reprogram cells to control the expression levels of genes related to angiogenesis is also possible [65,66].

2.1.4 Strategies for cardiac tissue regeneration

Ischemic heart disease is the leading cause of death worldwide, representing around 9 million deaths per year [67]. This condition is caused by the blockage of a coronary artery, causing a lack of oxygen and nutrient supply that eventually leads to cardiac cells (cardiomyocytes) death. As adult human cardiomyocytes have an extremely limited regenerative capacity, the damaged tissue is replaced by a fibrotic scar [68]. This loss of functional cardiac tissue translates into a decrease in the pumping force exerted by the heart, which leads to a remodeling process that causes further problems such as cardiac dilatation, mechanical dysfunction and eventually fatal heart failure [69].

Tissue engineering strategies used to tackle heart disease were focused in the first place on *ex vivo* approaches for implantation using different cell types. Initial attempts were focused on the transplantation of non-cardiac cells due to the difficulties of obtaining enough quantities of functional cardiomyocytes *in vitro* [70]. However, unsuccessful results shifted the focus of research towards cardiac-derived cells. The discovery of embryonic stem cells (ESC), pluripotent cells obtained from the interior of early embryos [71], and induced pluripotent stem cells (iPSC), obtained from the reprogramming of somatic cells [72], opened unprecedented possibilities to obtain a large number of CM that combined with polymeric materials in the form of injectable hydrogels or fibrous cell patches could be used for transplantation [73,74], showing improved cardiac function [75-77]. Nevertheless, the use of cardiac patches based on stem cells has several drawbacks that hugely limit their clinical applicability, mainly their low engraftment efficacy, the high risk of ventricular tachycardia and the tumorigenic and immunogenic potential [78,79].

Due to all the limitations of the *ex vivo* strategies, different researchers considered the possibility of implanting acellular materials for the *in situ* modulation of the cardiac

microenvironment. The most extended approach is the use of injectable scaffolds, due to the possibility of delivery directly to the site of injury using a catheter, eliminating the need for a surgical intervention [80]. These scaffolds generally consist of acellular polymeric hydrogels [81-85], whose effects have been attributed to their potential to increase the ventricular wall thickness [86,87] and their bioactivity, which helps in stimulating angiogenesis and cell survival [88]. The delivery of biochemical cues such as growth factors or exosomes has also been explored to stimulate angiogenesis and increase regional coronary flow [89,90], as well as the use of biomolecules for the intracellular reprogramming of resident cardiac cells, mainly transcription factors to transform fibroblast to cardiomyocyte-like cells and reduce fibrosis [91,92]. The main challenges for translating these approaches from animal models to the clinic remain the low delivery/reprogramming efficiencies, the immaturity and heterogenicity of the cardiac cell population [93] and the longer times needed to obtain cardiomyocyte-like cells in humans, which can be attributed to epigenetic barriers and the longer developmental periods [94].

2.2 Preclinical testing of biomaterials

As has been discussed in the previous section, the first developments in the biomaterials field have been focused on designing inert materials that could be used as passive elements to fill defects or provide a mechanical support. However, the development of tissue engineering made them an active part of the regeneration process, capable of stimulating cell growth and differentiation, which requires an in-depth analysis of their interactions with biological systems before their implantation into humans is even considered. This stage is known as preclinical testing and involves a full characterization of the material in terms of its physical, chemical, and biological properties. To perform the preclinical testing, researchers have to follow the guidelines established by the International Organisation for Standardisation (ISO) through the ISO-10993 [95], which covers the tests to assess the toxicity and functionality of the biomaterial from the original implant conformation to the formation of the new tissue, including any degradation by-products.

There are two stages in the preclinical testing of biomaterials: the first one is known as ***in vitro* testing**, as it is based on culturing cells outside the body under conditions that support their growth and differentiation. It offers short-term (days to weeks) information on many early cell responses, such as cell adhesion or changes in morphology or phenotype. Longer-term responses can be simulated by artificially aging the materials using high-temperature or enzyme solutions [96]. Regarding cell type, primary cells obtained from tissues are generally the alternative with the highest degree of biomimicry, but the difficulty of obtaining adequate numbers for the multiple tests requires making immortalized cell lines the model of choice, as they replicate faster without losing their phenotype. The particular cell lineage will be dependent on the selected application:

for instance, if the material is going to be used for orthopaedics, the most adequate cell types would be either mesenchymal stem cells or osteoblasts [97].

The main concern when performing *in vitro* biomaterial testing is to study its biocompatibility, which ensures that it will not have any toxic effect when implanted in the host. This is especially critical when no previous preclinical or clinical safety data is available regarding the nature and duration of biomaterial-tissue contact [95]. Some general steps in assessing biocompatibility involve evaluating cytotoxicity and cell death [98,99] or performing genotoxicity testing, which is aimed at elucidating possible negative interactions of the implant with the host genetic material [100]. The second step in a preclinical study is known as *in vivo* testing, as it involves the implantation of the materials in animal models to further validate results obtained during *in vitro* testing. Some examples of these tests include genotoxicity testing [101], carcinogenicity [96,102], hemocompatibility [103] or irritation [104]. There are also some specific assays to evaluate the functionality of the implanted biomaterials in eliciting a certain physiological response. In this thesis, we are interested in two specific processes, bone vascularization and cardiac ischemia-reperfusion. The particular preclinical models used to evaluate these physiological phenomena will be addressed in detail in the specific chapters.

2.3 Microphysiological systems

As detailed in the previous section, current preclinical models based on cell lines and animal models are highly limited in predicting the pathophysiology of human disease, personalized drug responses and off-target toxicities [105]. This lack of adequate preclinical models has translated into a dramatic decrease in the number of new drugs approved, which has risen a lot of concern within the pharmaceutical industry over the last 20 years [106,107]. A lot of research has been performed during the last decades in order to generate models that could faithfully recapitulate the actual *in vivo* response in humans. Breakthrough discoveries in the field of stem cell biology have led to the development of increasingly complex cell culture models known as organoids, which are self-assembled 3D cultures of stem cells that organize and differentiate into multiple cell types that can mimic the actual tissue complexity [108]. This was a big milestone in tissue engineering that allowed us to better understand signalling pathways and drug responses with an unprecedented level of biomimicry compared to the traditional 2D assays [109,110]. However, traditional organoid cultures have several limitations, such as the great difficulty of harvesting samples for biochemical and genetic analysis (especially luminal content), the lack of multiscale architecture and tissue-tissue interfaces or the absence of microenvironmental cues (flow, mechanical contractions, electrical stimuli, etc.) that greatly influence tissue development and function [111].

Nevertheless, the advancements in microfabrication technologies during the last decades have opened up unprecedented possibilities to address these issues. One of the main driving forces that led to the convergence between microtechnology and tissue engineering, was the discovery of polydimethylsiloxane by George Whitesides in the 90s [112]. It is a highly biocompatible, optically transparent elastomer that can be easily processed to obtain micrometric devices at a really low cost. The method used to obtain the devices is known as soft-lithography and consists in pouring the PDMS over a silicon mould fabricated with methods commonly used in the microelectronics industry (such as photolithography). The polymer is then crosslinked by temperature and unmoulded, generating as a result hollow chambers where cells can be cultured. PDMS is generally irreversibly bonded to a flat smooth substrate such as glass, resulting in a closed system in which cell media can be easily perfused [113]. This sort of microsystems in which liquids can be perfused (commonly referred to as "microfluidic systems") are characterized by the laminar nature of the flow, which means that viscous forces dominate over the inertial ones, making fluid behaviour predictable and easy to control [114].

The first study using a microfluidic device to mimic organ-level human physiology was published by Michael Shuler and collaborators in 2004, in which the culture and interaction between lung and liver cells were mimicked in a silicon chip [115]. This motivated a range of other studies trying to mimic other organs such as the muscles [116], bones [117], or the kidney [118]. The field established itself around 2010 when Donald Ingber and collaborators published the first microfluidic chip capturing organ-level functions of the human lung, introducing for the first time the term **organ-on-a-chip** [119], which has been used interchangeably with **microphysiological system** ever since [105]. These advanced systems have allowed to overcome many of the limitations of traditional organoid cultures, such as replicating tissue interfaces such as vascular or endothelial barriers [120], replicating the organization of complex elongated tissues cells such as the heart or the liver [121-123] and the incorporation of actuators for precise fluidic mechanical and structural control as well as sensors for continuous monitoring of the tissue function [105]. In fact, research in microphysiological systems has attracted tremendous interest from the pharmaceutical industry and regulatory agencies and resulted in the creation of more than 28 companies in the last decade [124].

The proposed devices can be categorized into three main groups depending on the target tissue and drug mechanisms to be elucidated. The first category is **tissue barriers,** which can be modelled using different strategies. The first one involves the use of stretchable thin polymeric membranes, like 10 µm PDMS membranes (see **Fig.3-a**), which have been used to mimic the alveolar-capillary interface, including the cyclic mechanical strain cell are subjected to in the lungs [119]. This approach has been expanded to model other organ interfaces in which cyclic

mechanical deformations and perfusion play a key role, such as the intestinal barrier [125]. The second alternative is based on the injection of hydrogels, such as collagen or fibrin, in devices with built-in microchannel networks (see **Fig.3-b**), which are later seeded with endothelial cells to replicate the vascular networks [120,126]. The intrinsic three-dimensional nature of these systems allows for studying complex interactions between specialized cells and the vasculature, for instance in human kidney tubule models [127,128]. The third option is to resuspend endothelial cells in the hydrogel to create a self-assembled microvascular network (see **Fig.3-c**) that can be perfused through their anastomose with the lateral microfluidic channels [129,130]. This approach allows the creation of different compartments in which multiple cell types can be incorporated and their interactions monitored through confocal microscopy [131]. For instance, the blood-brain barrier [132] or cancer cell extravasation in a tumour microenvironment [133] has been modelled with this approach.

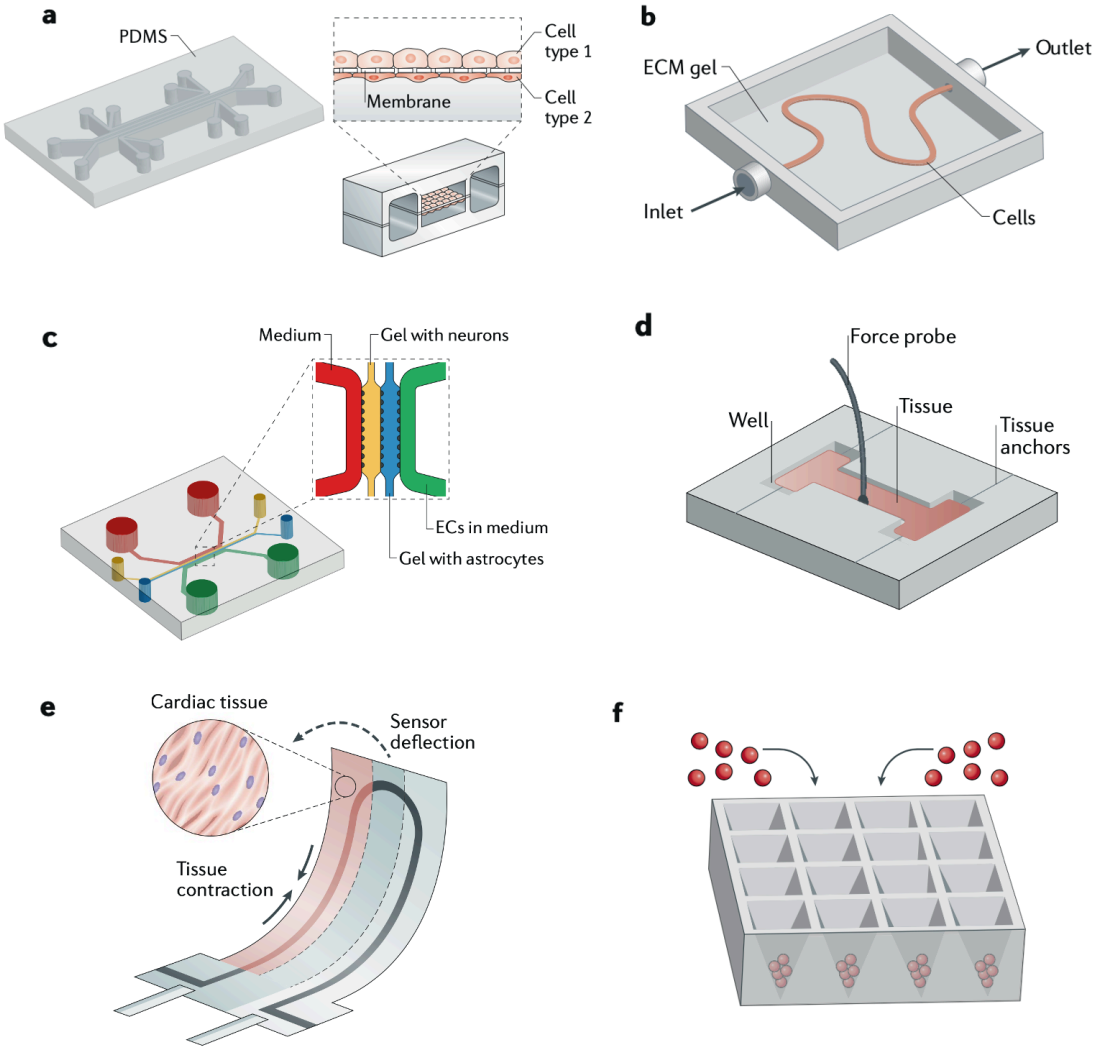

Figure 3 Microphysiological system architectures. (a) Reproduction of the alveolar-capillary interface using a flexible PDMS membrane and side vacuum channels to mimic lung contractions. **(b)** Endothelial vessel model based on the hydrogel patterning method. **(c)** Self-assembled tissue interface to mimic the blood-brain barrier. **(d)**

Parenchymal heart tissue model relying on cardiac cell self-assembling between elastic parallel rods. **(e)** Cardiac tissue grown on a flexible cantilever with embedded strain sensors. **(f)** Spherical parenchymal liver tissue generated using the hanging drop method. *Adapted from [105].*

The second category is **parenchymal tissues,** which are the bulk functional substance of an organ. Contrary to tissue interfaces, an organized 3D architecture is essential for the functionality of these model. Parenchymal tissues can be broadly categorized as elongated or spherical. A representative example of the first category is the cardiac muscle tissue, which is highly organized in anisotropic cardiac bundles [134]. The most widely used approach to achieve this level of organization is to inject the cardiac cells resuspended in a hydrogel (commonly collagen) between two elastic posts (see **Fig.3-d**), which drive CMs elongation due to the passive tension generated [135,136]. The bending of the posts also serves as a way to estimate the force exerted by tissue contraction [137,138]. A different approach is to seed the CM on top of flexible cantilevers with embedded strain sensors (see **Fig.3-e**), which allows for the simultaneous application of electrical stimulation and recording of contractile activity [139]. Regarding the second category, common spherical tissues are the liver, pancreas or tumours, which can be created using the hanging drop technology to create cell aggregates in suspension [140–142] (see **Fig.3-f**) or microfluidic traps [143,144]. The last category within microphysiological systems is the **body-on-a-chip** devices, in which several tissues are fluidically connected in order to mimic complex inter-organ interactions and assess how drugs are absorbed, distributed, metabolized and eliminated from the body (ADME profile) [105]. Different platforms have been proposed to achieve this goal, from complex systems in which 13 organs, including barrier (such as the skin or intestinal barrier or the lung) and parenchymal tissues (such as the liver or kidney) [145], to simpler systems with a couple of organs to better evaluate their interactions, for example the liver and pancreas to model the pathogenesis of diabetes type 2 [146]. One of the main challenges faced by these systems is how to correctly escalate different physiological parameters such as the tissue size or interface surface proportions [147].

This thesis builds on the current state of the art in the microphysiological systems field and puts forward innovative models that can be used to perform preclinical studies with biomaterials, an area of application that has been minimally explored with this technology. We believe that such models can be of great use in the design and testing of new biomaterials for regenerative therapies.

2.4 References

[1] Persidis A 1999 Tissue engineering *Nat. Biotechnol.* **17** 508–10.

[2] Vanholder R, Dominguez-Gil B, Busic M, Cortez-Pinto H, Craig J C, Jager K J, Mahillo B, Stel V S, Valentin M O, Zoccali C and Oniscu G C 2021 Organ donation and

transplantation: a multi-stakeholder call to action *Nat. Rev. Nephrol.* **5** 1–15.

[3] Langer R and Vacanti J P 1993 Tissue engineering *Science* **260** 920–6.

[4] Lanza R, Langer R and Vacanti J P 2020 Principles of tissue engineering *Elsevier* **5 ed** 53-61.

[5] Gaharwar A K, Singh I and Khademhosseini A 2020 Engineered biomaterials for in situ tissue regeneration *Nat. Rev. Mater.* **5** 686–705.

[6] Pan E, Bogumil D, Cortessis V, Yu S and Nieva J 2020 A systematic review of the efficacy of preclinical models of lung cancer drugs *Front. Oncol.* **10** 591-599.

[7] Bhatia S N and Ingber D E 2014 Microfluidic organs-on-chips *Nat. Biotechnol.* **32** 760–72.

[8] Ratner B D and Bryant S J 2004 Biomaterials: where we have been and where we are going *Annu. Rev. Biomed. Eng.* **6** 41–75.

[9] Hench L L and Wilson J 1984 Surface-active biomaterials *Science (80-.).* **226** 630–6.

[10] Hench L L and Polak J M 2002 Third-generation biomedical materials *Science (80).* **295** 1014–7.

[11] Okita K, Ichisaka T and Yamanaka S 2007 Generation of germline-competent induced pluripotent stem cells *Nature* **448** 313–7.

[12] Kowalski P S, Bhattacharya C, Afewerki S and Langer R 2018 Smart biomaterials: recent advances and future directions *ACS Biomater. Sci. Eng.* **4** 3809–17.

[13] Khademhosseini A and Langer R 2016 A decade of progress in tissue engineering *Nat. Protoc.* **11** 1775–81.

[14] Pham Q P, Sharma U and Mikos A G 2006 Electrospinning of polymeric nanofibers for tissue engineering applications: a review *Tissue Eng.* **12** 1197–211.

[15] Murphy S V and Atala A 2014 3D bioprinting of tissues and organs *Nat. Biotechnol.* **32** 773–85.

[16] Williams D F 2019 Challenges with the development of biomaterials for sustainable tissue engineering *Front. Bioeng. Biotechnol.* **7** 127-137.

[17] Gurtner G C, Werner S, Barrandon Y and Longaker M T 2008 Wound repair and regeneration *Nature* **453** 314–21.

[18] Eming S A, Wynn T A and Martin P 2017 Inflammation and metabolism in tissue repair and regeneration *Science (80-.).* **356** 1026–30.

[19] Castaño O, Perez-Amodio S, Navarro-Requena C, Mateos-Timoneda M A and Engel E 2018 Instructive microenvironments in skin wound healing: Biomaterials as signal releasing platforms *Adv. Drug Deliv. Rev.* **129** 95–117.

[20] Pinet K and McLaughlin K A 2019 Mechanisms of physiological tissue remodeling in animals: Manipulating tissue, organ, and organism morphology *Dev. Biol.* **451** 134–45.

[21] Reilly G C and Engler A J 2010 Intrinsic extracellular matrix properties regulate stem cell differentiation *J. Biomech.* **43** 55–62.

[22] Wang N, Tytell J D and Ingber D E 2009 Mechanotransduction at a distance: Mechanically coupling the extracellular matrix with the nucleus *Nat. Rev. Mol. Cell Biol.* **10** 75–82.

[23] Griffin D R, Weaver W M, Scumpia P O, Di Carlo D and Segura T 2015 Accelerated wound healing by injectable microporous gel scaffolds assembled from annealed building blocks *Nat. Mater.* **14** 737–44.

[24] Chen Z, Wu C, Gu W, Klein T, Crawford R and Xiao Y 2014 Osteogenic differentiation of bone marrow MSCs by β-tricalcium phosphate stimulating macrophages via BMP2 signalling pathway *Biomaterials* **35** 1507–18.

[25] Gibbs D M R, Black C R M, Hulsart-Billstrom G, Shi P, Scarpa E, Oreffo R O C and Dawson J I 2016 Bone induction at physiological doses of BMP through localization by clay nanoparticle gels *Biomaterials* **99** 16–23.

[26] Waters R, Pacelli S, Maloney R, Medhi I, Ahmed R P H and Paul A 2016 Stem cell secretome-rich nanoclay hydrogel: A dual action therapy for cardiovascular regeneration *Nanoscale* **8** 7371–6.

[27] Dawson J I, Kanczler J M, Yang X B, Attard G S and Oreffo R O C 2011 Clay gels for the delivery of regenerative microenvironments *Adv. Mater.* **23** 3304–8.

[28] Biswas A, Liu Y, Liu T, Fan G and Tang Y 2012 Polyethylene glycol-based protein nanocapsules for functional delivery of a differentiation transcription factor *Biomaterials* **33** 5459–67.

[29] Paunovska K, Da Silva Sanchez A J, Sago C D, Gan Z, Lokugamage M P, Islam F Z, Kalathoor S, Krupczak B R and Dahlman J E 2019 Nanoparticles containing oxidized cholesterol deliver mRNA to the liver microenvironment at clinically relevant doses *Adv. Mater.* **31** 8341-51.

[30] Cong L, Ran F A, Cox D, Lin S, Barretto R, Habib N, Hsu P D, Wu X, Jiang W, Marraffini L A and Zhang F 2013 Multiplex genome engineering using CRISPR/Cas systems *Science* **339** 819–23.

[31] Mali P, Yang L, Esvelt K M, Aach J, Guell M, DiCarlo J E, Norville J E and Church G M 2013 RNA-guided human genome engineering via Cas9 *Science* **339** 823–6.

[32] Kretlow J D, Young S, Klouda L, Wong M and Mikos A G 2009 Injectable biomaterials for regenerating complex craniofacial tissues *Adv. Mater.* **21** 3368–93.

[33] Jo Y K, Choi B H, Kim C S and Cha H J 2017 Diatom-inspired silica nanostructure coatings with controllable microroughness using an engineered mussel protein glue to accelerate bone growth on titanium-based implants *Adv. Mater.* **29** 46-55.

[34] Ma Q L, Zhao L Z, Liu R R, Jin B Q, Song W, Wang Y, Zhang Y S, Chen L H and Zhang Y M 2014 Improved implant osseointegration of a nanostructured titanium surface via mediation of macrophage polarization *Biomaterials* **35** 9853–67.

[35] Li J, Wen J, Li B, Li W, Qiao W, Shen J, Jin W, Jiang X, Yeung K W K and Chu P K 2018 Valence state manipulation of cerium oxide nanoparticles on a titanium surface for modulating cell fate and bone formation *Adv. Sci.* **5** 678-693.

[36] Takizawa T, Nakayama N, Haniu H, Aoki K, Okamoto M, Nomura H, Tanaka M, Sobajima A, Yoshida K, Kamanaka T, Ajima K, Oishi A, Kuroda C, Ishida H, Okano S, Kobayashi S, Kato H and Saito N 2018 Titanium fiber plates for bone tissue repair *Adv. Mater.* **30** 608-619.

[37] Koons G L, Diba M and Mikos A G 2020 Materials design for bone-tissue engineering *Nat. Rev. Mater.* **5** 584–603.

[38] Loessner D, Meinert C, Kaemmerer E, Martine L C, Yue K, Levett P A, Klein T J, Melchels F P W, Khademhosseini A and Hutmacher D W 2016 Functionalization, preparation and use of cell-laden gelatin methacryloyl-based hydrogels as modular tissue culture platforms *Nat. Protoc.* **11** 727–46.

[39] Papageorgiou P, Vallmajo-Martin Q, Kisielow M, Sancho-Puchades A, Kleiner E and Ehrbar M 2019 Expanded skeletal stem and progenitor cells promote and participate in induced bone regeneration at subcritical BMP-2 dose *Biomaterials* **217** 278-291.

[40] Hasani-Sadrabadi M M, Sarrion P, Nakatsuka N, Young T D, Taghdiri N, Ansari S, Aghaloo T, Li S, Khademhosseini A, Weiss P S and Moshaverinia A 2019 Hierarchically patterned polydopamine-containing membranes for periodontal tissue engineering *ACS Nano* **13** 3830–8.

[41] Li L, Li J, Guo J, Zhang H, Zhang X, Yin C, Wang L, Zhu Y and Yao Q 2019 3D molecularly functionalized cell-free biomimetic scaffolds for osteochondral regeneration *Adv. Funct. Mater.* **29** 356-368.

[42] Zhang S, Ma B, Liu F, Duan J, Wang S, Qiu J, Li D, Sang Y, Liu C, Liu D and Liu H 2018 Polylactic acid nanopillar array-driven osteogenic differentiation of human adipose-derived stem cells determined by pillar diameter *Nano Lett.* **18** 2243–53.

[43] Feng P, Wu P, Gao C, Yang Y, Guo W, Yang W and Shuai C 2018 A multimaterial scaffold with tunable properties: toward bone tissue repair *Adv. Sci.* **5** 817-832.

[44] Felix Lanao R P, Leeuwenburgh S C G, Wolke J G C and Jansen J A 2011 Bone response to fast-degrading, injectable calcium phosphate cements containing PLGA microparticles *Biomaterials* **32** 8839–47.

[45] Hench L L 2006 The story of Bioglass *J. Mater. Sci. Mater. Med.* **17** 967–78.

[46] Luo Z, Pan J, Sun Y, Zhang S, Yang Y, Liu H, Li Y, Xu X, Sui Y and Wei S 2018 Injectable 3D porous micro-scaffolds with a bioengine for cell transplantation and tissue regeneration *Adv. Funct. Mater.* **28** 335-348.

[47] Lei M, Qu X, Liu H, Liu Y, Wang S, Wu S, Bentley W E, Payne G F and Liu C 2019 Programmable electrofabrication of porous Janus films with tunable Janus balance for anisotropic cell guidance and tissue regeneration *Adv. Funct. Mater.* **29** 65-80.

[48] Jakus A E, Rutz A L, Jordan S W, Kannan A, Mitchell S M, Yun C, Koube K D, Yoo S C, Whiteley H E, Richter C P, Galiano R D, Hsu W K, Stock S R, Hsu E L and Shah R N 2016 Hyperelastic “bone”: A highly versatile, growth factor-free, osteoregenerative, scalable, and surgically friendly biomaterial *Sci. Transl. Med.* **8** 358-373.

[49] Diba M, Camargo W A, Brindisi M, Farbod K, Klymov A, Schmidt S, Harrington M J, Draghi L, Boccaccini A R, Jansen J A, van den Beucken J J J P and Leeuwenburgh S C G 2017 Composite colloidal gels made of bisphosphonate-functionalized gelatin and bioactive glass particles for regeneration of osteoporotic bone defects *Adv. Funct. Mater.* **27** 438-450.

[50] Wang S, Kempen D H R, De Ruiter G C W, Cai L, Spinner R J, Windebank A J, Yaszemski M J and Lu L 2015 Molecularly engineered biodegradable polymer networks with a wide range of stiffness for bone and peripheral nerve regeneration *Adv. Funct. Mater.* **25** 2715–24.

[51] Engler A J, Sen S, Sweeney H L and Discher D E 2006 Matrix elasticity directs stem cell lineage specification *Cell* **126** 677–89.

[52] Cui H, Zhu W, Holmes B and Zhang L G 2016 Biologically inspired smart release system based on 3D bioprinted perfused scaffold for vascularized tissue regeneration *Adv. Sci.* **3** 58-68.

[53] Karageorgiou V and Kaplan D 2005 Porosity of 3D biomaterial scaffolds and osteogenesis *Biomaterials* **26** 5474–91.

[54] Aguirre A, González A, Planell J A, Engel E 2010 Extracellular calcium modulates in vitro bone marrow-derived Flk-1+ CD34+ progenitor cell chemotaxis and differentiation through a calcium-sensing receptor *Biochem. Biophys. Res. Commun.* **393** 156-61.

[55] Aguirre A, González A, Navarro M, Castaño O, Planell J A, Engel E 2012 Control of microenvironmental cues with a smart biomaterial composite promotes endothelial progenitor cell angiogenesis *Eur. Cells Mater.* **24** 90–106.

[56] Wu C, Zhou Y, Xu M, Han P, Chen L, Chang J and Xiao Y 2013 Copper-containing mesoporous bioactive glass scaffolds with multifunctional properties of angiogenesis capacity, osteostimulation and antibacterial activity *Biomaterials* **34** 422–33.

[57] Stahli C, Muja N and Nazhat S N 2013 Controlled copper ion release from phosphate-based glasses improves human umbilical vein endothelial cell survival in a reduced nutrient environment *Tissue Eng. - Part A* **19** 548–57.

[58] Kargozar S, Lotfibakhshaiesh N, Ai J, Mozafari M, Brouki Milan P, Hamzehlou S, Barati M, Baino F, Hill R G and Joghataei M T 2017 Strontium- and cobalt-substituted bioactive glasses seeded with human umbilical cord perivascular cells to promote bone regeneration via enhanced osteogenic and angiogenic activities *Acta Biomater.* **58** 502–14.

[59] Lee I H, Yu H S, Lakhkar N J, Kim H W, Gong M S, Knowles J C and Wall I B 2013 Development, characterisation and biocompatibility testing of a cobalt-containing titanium phosphate-based glass for engineering of vascularized hard tissues *Mater. Sci. Eng. C* **33** 2104–12.

[60] Wacker B, Alford S, Scott E, Thakur M, Longmore G, Elbert D 2008 Endothelial cell migration on RGD-peptide containing PEG hydrogels in the presence of sphingosine 1-phosphate *Biophys J.* **94** 273-285.

[61] Martino M M, Mochizuki M, Rothenfluh D A, Rempel S A, Hubbell J A and Barker T H 2009 Controlling integrin specificity and stem cell differentiation in 2D and 3D environments through regulation of fibronectin domain stability *Biomaterials* **30** 1089–97.

[62] Anderson S, Siegman S, Segura T 2011 The effect of vascular endothelial growth factor (VEGF) presentation within fibrin matrices on endothelial cell branching *Biomaterials* **32** 7432-7443.

[63] Dashnyam K, Jin G Z, Kim J H, Perez R, Jang J H and Kim H W 2017 Promoting angiogenesis with mesoporous microcarriers through a synergistic action of delivered

silicon ion and VEGF *Biomaterials* **116** 145–57.

[64] Spiller K L, Nassiri S, Witherel C E, Anfang R R, Ng J, Nakazawa K R, Yu T and Vunjak-Novakovic G 2015 Sequential delivery of immunomodulatory cytokines to facilitate the M1-to-M2 transition of macrophages and enhance vascularization of bone scaffolds *Biomaterials* **37** 194–207.

[65] Li Y, Fan L, Liu S, Liu W, Zhang H, Zhou T, Wu D, Yang P, Shen L, Chen J and Jin Y 2013 The promotion of bone regeneration through positive regulation of angiogenic-osteogenic coupling using microRNA-26a *Biomaterials* **34** 5048–58.

[66] Mora-Raimundo P, Lozano D, Manzano M and Vallet-Regi M 2019 Nanoparticles to knockdown osteoporosis-related gene and promote osteogenic marker expression for osteoporosis treatment *ACS Nano* **13** 5451–64.

[67] Roth G A, Johnson C, Abajobir A, Abd-Allah F, Abera S F, Abyu G, Ahmed M, Aksut B, Alam T, J, Kim D, Kolte D, Kosen S, Krohn K J, Kumar G A, Kwan G F, Lal D K, Larsson A, Linn S, Lopez A, et al 2017 Global, regional, and national burden of cardiovascular diseases for 10 causes, 1990 to 2015 *J. Am. Coll. Cardiol.* **70** 1–25.

[68] Hashimoto H, Olson E N and Bassel-Duby R 2018 Therapeutic approaches for cardiac regeneration and repair *Nat. Rev. Cardiol.* **15** 585–600.

[69] Cohn J N, Ferrari R and Sharpe N 2000 Cardiac remodeling-concepts and clinical implications: a consensus paper from an International Forum on Cardiac Remodeling *J. Am. Coll. Cardiol.* **35** 569–82.

[70] Behfar A, Crespo-Diaz R, Terzic A and Gersh B J 2014 Cell therapy for cardiac repair-lessons from clinical trials *Nat. Rev. Cardiol.* **11** 232–46.

[71] Murry C E and Keller G 2008 Differentiation of embryonic stem cells to clinically relevant populations: lessons from embryonic development *Cell* **132** 661–80.

[72] Takahashi K, Tanabe K, Ohnuki M, Narita M, Ichisaka T, Tomoda K and Yamanaka S 2007 Induction of pluripotent stem cells from adult human fibroblasts by defined factors *Cell* **131** 861–72.

[73] Kawamura M, Miyagawa S, Fukushima S, Saito A, Miki K, Funakoshi S, Yoshida Y, Yamanaka S, Shimizu T, Okano T, Daimon T, Toda K and Sawa Y 2017 Enhanced therapeutic effects of human iPS cell derived-cardiomyocyte by combined cell-sheets with omental flap technique in porcine ischemic cardiomyopathy model *Sci. Rep.* **7** 824-835.

[74] Chow A, Stuckey D J, Kidher E, Rocco M, Jabbour R J, Mansfield C A, Darzi A, Harding S E, Stevens M M and Athanasiou T 2017 Human induced pluripotent stem cell-derived

cardiomyocyte encapsulating bioactive hydrogels improve rat heart function post myocardial infarction *Stem Cell Reports* **9** 1415–22.

[75] Shiba Y, Gomibuchi T, Seto T, Wada Y, Ichimura H, Tanaka Y, Ogasawara T, Okada K, Shiba N, Sakamoto K, Ido D, Shiina T, Ohkura M, Nakai J, Uno N, Kazuki Y, Oshimura M, Minami I and Ikeda U 2016 Allogeneic transplantation of iPS cell-derived cardiomyocytes regenerates primate hearts *Nature* **538** 388–91.

[76] Kawamura M, Miyagawa S, Miki K, Saito A, Fukushima S, Higuchi T, Kawamura T, Kuratani T, Daimon T, Shimizu T, Okano T and Sawa Y 2012 Feasibility, safety, and therapeutic efficacy of human induced pluripotent stem cell-derived cardiomyocyte sheets in a porcine ischemic cardiomyopathy model *Circulation* **126** 29-37.

[77] Qiao H, Zhang H, Yamanaka S, Patel V V., Petrenko N B, Huang B, Muenz L R, Ferrari V A, Boheler K R and Zhou R 2011 Long-term improvement in postinfarct left ventricular global and regional contractile function is mediated by embryonic stem cell-derived cardiomyocytes *Circ. Cardiovasc. Imaging* **4** 33–41.

[78] Sougawa N, Miyagawa S, Fukushima S, Kawamura A, Yokoyama J, Ito E, Harada A, Okimoto K, Mochizuki-Oda N, Saito A and Sawa Y 2018 Immunologic targeting of CD30 eliminates tumourigenic human pluripotent stem cells, allowing safer clinical application of hiPSC-based cell therapy *Sci. Rep.* **8** 1–12.

[79] Miura K, Okada Y, Aoi T, Okada A, Takahashi K, Okita K, Nakagawa M, Koyanagi M, Tanabe K, Ohnuki M, Ogawa D, Ikeda E, Okano H and Yamanaka S 2009 Variation in the safety of induced pluripotent stem cell lines *Nat. Biotechnol.* **27** 743–745.

[80] Rane A A and Christman K L 2011 Biomaterials for the treatment of myocardial infarction: a 5-year update *J. Am. Coll. Cardiol.* **58** 2615–29.

[81] Leor J, Tuvia S, Guetta V, Manczur F, Castel D, Willenz U, Petnehazy O, Landa N, Feinberg M S, Konen E, Goitein O, Tsur-Gang O, Shaul M, Klapper L and Cohen S 2009 Intracoronary injection of in situ forming alginate hydrogel reverses left ventricular remodeling after myocardial infarction in swine *J. Am. Coll. Cardiol.* **54** 1014–23.

[82] McLaughlin S, McNeill B, Podrebarac J, Hosoyama K, Sedlakova V, Cron G, Smyth D, Seymour R, Goel K, Liang W, Rayner K J, Ruel M, Suuronen E J and Alarcon E I 2019 Injectable human recombinant collagen matrices limit adverse remodeling and improve cardiac function after myocardial infarction *Nat. Commun.* **10** 1–14.

[83] Huang K, Ozpinar E W, Su T, Tang J, Shen D, Qiao L, Hu S, Li Z, Liang H, Mathews K, Scharf V, Freytes D O and Cheng K 2020 An off-the-shelf artificial cardiac patch improves

cardiac repair after myocardial infarction in rats and pigs *Sci. Transl. Med.* **12** 538-567.

[84] Samsamshariat S A, Hashemzadeh M, Samsamshariat Z and Movahed M R 2005 Cardiovascular and hemodynamic effect of polyethylene glycol in Rats *Cardiovasc. Revascularization Med.* **6** 70–72.

[85] Contessotto P, Orbanic D, da Costa M, Jin C, Owens P, Chantepie S, Chinello C, Newell J, Magni F, Papy-Garcia D, Karlsson N G, Kilcoyne M, Dockery P, Rodriguez-Cabello J C and Pandit A 2021 Elastin-like recombinamers-based hydrogel modulates post-ischemic remodeling in a non-transmural myocardial infarction in sheep *Sci. Transl. Med.* **13** 53–80.

[86] Wall S T, Walker J C, Healy K E, Ratcliffe M B and Guccione J M 2006 Theoretical impact of the injection of material into the myocardium: A finite element model simulation *Circulation* **114** 2627–35.

[87] Tous E, Ifkovits J L, Koomalsingh K J, Shuto T, Soeda T, Kondo N, Gorman J H, Gorman R C and Burdick J A 2011 Influence of injectable hyaluronic acid hydrogel degradation behavior on infarction-induced ventricular remodeling *Biomacromolecules* **12** 4127–35.

[88] Radisic M and Christman K L 2013 Materials science and tissue engineering: repairing the heart *Mayo Clinic Proceedings* **88** 884–98.

[89] Garbayo E, Gavira J J, De Yebenes M G, Pelacho B, Abizanda G, Lana H, Blanco-Prieto M J and Prosper F 2016 Catheter-based intramyocardial injection of FGF1 or NRG1-loaded MPs improves cardiac function in a preclinical model of ischemia-reperfusion *Sci. Rep.* **6** 932-944.

[90] Harada K, Friedman M, Lopez J J, Wang S Y, Li J, Prasad P V., Pearlman J D, Edelman B R, Sellke F W and Simons M 1996 Vascular endothelial growth factor administration in chronic myocardial ischemia *Am. J. Physiol. - Hear. Circ. Physiol.* **270** 39–45.

[91] Song K, Nam Y J, Luo X, Qi X, Tan W, Huang G N, Acharya A, Smith C L, Tallquist M D, Neilson E G, Hill J A, Bassel-Duby R and Olson E N 2012 Heart repair by reprogramming non-myocytes with cardiac transcription factors *Nature* **485** 599–604.

[92] Ieda M, Fu J D, Delgado-Olguin P, Vedantham V, Hayashi Y, Bruneau B G and Srivastava D 2010 Direct reprogramming of fibroblasts into functional cardiomyocytes by defined factors *Cell* **142** 375–86.

[93] Sadahiro T, Yamanaka S and Ieda M 2015 Direct cardiac reprogramming: progress and challenges in basic biology and clinical applications *Circ. Res.* **116** 1378–91.

[94] Zhou J X and Huang S 2011 Understanding gene circuits at cell-fate branch points for rational cell reprogramming *Trends Genet.* **27** 55–62.

[95] Boutrand J P 2019 Biocompatibility and performance of medical devices *Elsevier* **2nd ed** 65-95.

[96] Di Silvio L 2009 Cellular response to biomaterials *Elsevier* **1st ed** 508-538.

[97] Zhi Lin Sun, Wataha J C and Hanks C T 1997 Effects of metal ions on osteoblast-like cell metabolism and differentiation *J. Biomed. Mater. Res.* **34** 29–37.

[98] Riss T, Niles A, Moravec R, Karassina N and Vidugiriene J 2004 Cytotoxicity assays: in vitro methods to measure dead cells *NIH Assay Guidance Manual* **1st ed** 1-15.

[99] Oancea M, Mazumder S, Crosby M E and Almasan A 2006 Apoptosis assays *Methods Mol. Med.* **129** 279–90.

[100] Gatehouse D, Haworth S, Cebula T, Gocke E, Kier L, Matsushima T, Melcion C, Nohmi T, Ohta T, Venitt S and Zeiger E 1994 Recommendations for the performance of bacterial mutation assays *Mutat. Res. Mutagen. Relat. Subj.* **312** 217–33.

[101] Sommer S, Buraczewska I and Kruszewski M 2020 Micronucleus assay: the state of art and future directions *Int. J. Mol. Sci.* **21** 1534-53.

[102] Tamaoki N 2001 The rasH2 transgenic mouse: nature of the model and mechanistic studies on tumorigenesis *Toxicol. Pathol.* **29** 81–9.

[103] Yang Y, Franzen S F and Olin C L 1996 In vivo comparison of hemocompatibility of materials used in mechanical heart valves *J. Heart Valve Dis.* **5** 532–7.

[104] Perkins M A, Osborne R, Rana F R, Ghassemi A and Robinson M K 1999 Comparison of in vitro and in vivo human skin responses to consumer products and ingredients with a range of irritancy potential *Toxicol. Sci.* **48** 218–29.

[105] Zhang B, Korolj A, Lai B F L and Radisic M 2018 Advances in organ-on-a-chip engineering *Nat. Rev. Mater.* **3** 257–78.

[106] Paul S M, Mytelka D S, Dunwiddie C T, Persinger C C, Munos B H, Lindborg S R and Schacht A L 2010 How to improve RD productivity: The pharmaceutical industry's grand challenge *Nat. Rev. Drug Discov.* **9** 203–14.

[107] Adams C P and Brantner V V 2010 Spending on new drug development *Health Econ.* **19** 130–41.

[108] Takasato M, Er P X, Chiu H S, Maier B, Baillie G J, Ferguson C, Parton R G, Wolvetang E J, Roost M S, De Sousa Lopes S M C and Little M H 2015 Kidney organoids from human iPS cells contain multiple lineages and model human nephrogenesis *Nature* **526** 564–8.

[109] Sato T and Clevers H 2013 Growing self-organizing mini-guts from a single intestinal stem

cell: mechanism and applications *Science* **340** 1190–4.

[110] Mroue R and Bissell M J 2013 Three-dimensional cultures of mouse mammary epithelial cells *Methods Mol. Biol.* **945** 221–50.

[111] Huh D, Hamilton G A and Ingber D E 2011 From 3D cell culture to organs-on-chips *Trends Cell Biol.* **21** 745–54.

[112] Qin D, Xia Y and Whitesides G M 2010 Soft lithography for micro- and nanoscale patterning *Nat. Protoc.* **5** 491–502.

[113] Esch E W, Bahinski A and Huh D 2015 Organs-on-chips at the frontiers of drug discovery *Nat. Rev. Drug Discov.* **14** 248–60.

[114] Whitesides G M 2006 The origins and the future of microfluidics *Nature* **442** 368–73.

[115] Viravaidya K, Sin A and Shuler M L 2004 Development of a microscale cell culture analog to probe naphthalene toxicity *Biotechnol. Prog.* **20** 316–23.

[116] Lam M T, Huang Y C, Birla R K and Takayama S 2009 Microfeature guided skeletal muscle tissue engineering for highly organized 3-dimensional free-standing constructs *Biomaterials* **30** 1150–5.

[117] Jang K, Sato K, Igawa K, Chung U I and Kitamori T 2008 Development of an osteoblast-based 3D continuous-perfusion microfluidic system for drug screening *Anal. Bioanal. Chem.* **390** 825–32.

[118] Jang K J and Suh K Y 2010 A multi-layer microfluidic device for efficient culture and analysis of renal tubular cells *Lab Chip* **10** 36–42.

[119] Huh D, Matthews B D, Mammoto A, Montoya-Zavala M, Yuan Hsin H and Ingber D E 2010 Reconstituting organ-level lung functions on a chip *Science* **328** 1662–8.

[120] Zheng Y, Chen J, Craven M, Choi N W, Totorica S, Diaz-Santana A, Kermani P, Hempstead B, Fischbach-Teschl C, Lopez J A and Stroock A D 2012 In vitro microvessels for the study of angiogenesis and thrombosis *Proc. Natl. Acad. Sci. U. S. A.* **109** 9342–7.

[121] Wittmann K and Fischbach C 2017 Contextual control of adipose-derived stem cell function: implications for engineered tumor models *ACS Biomater. Sci. Eng.* **3** 1483–93.

[122] Khetani S R and Bhatia S N 2008 Microscale culture of human liver cells for drug development *Nat. Biotechnol.* **26** 120–6.

[123] Shlomai A, Schwartz R E, Ramanan V, Bhatta A, De Jong Y P, Bhatia S N and Rice C M 2014 Modeling host interactions with hepatitis B virus using primary and induced pluripotent stem cell-derived hepatocellular systems *Proc. Natl. Acad. Sci. U. S. A.* **111**

12193–8.

[124] Zhang B and Radisic M 2017 Organ-on-a-chip devices advance to market *Lab Chip* **17** 2395–420.

[125] Kimura H, Yamamoto T, Sakai H, Sakai Y and Fujii T 2008 An integrated microfluidic system for long-term perfusion culture and on-line monitoring of intestinal tissue models *Lab Chip* **8** 741–6.

[126] Ligresti G, Nagao R J, Xue J, Choi Y J, Xu J, Ren S, Aburatani T, Anderson S K, MacDonald J W, Bammler T K, Schwartz S M, Muczynski K A, Duffield J S, Himmelfarb J and Zheng Y 2016 A novel three-dimensional human peritubular microvascular system *J. Am. Soc. Nephrol.* **27** 2370–81.

[127] Adler M, Ramm S, Hafner M, Muhlich J L, Gottwald E M, Weber E, Jaklic A, Ajay A K, Svoboda D, Auerbach S, Kelly E J, Himmelfarb J and Vaidya V S 2016 A quantitative approach to screen for nephrotoxic compounds in vitro *J. Am. Soc. Nephrol.* **27** 1015–28.

[128] Weber E J, Chapron A, Chapron B D, Voellinger J L, Lidberg K A, Yeung C K, Wang Z, Yamaura Y, Hailey D W, Neumann T, Shen D D, Thummel K E, Muczynski K A, Himmelfarb J and Kelly E J 2016 Development of a microphysiological model of human kidney proximal tubule function *Kidney Int.* **90** 627–37.

[129] Hsu Y H, Moya M L, Hughes C C W, George S C and Lee A P 2013 A microfluidic platform for generating large-scale nearly identical human microphysiological vascularized tissue arrays *Lab Chip* **13** 2990–8.

[130] Phan D T T, Wang X, Craver B M, Sobrino A, Zhao D, Chen J C, Lee L Y N, George S C, Lee A P and Hughes C C W 2017 A vascularized and perfused organ-on-a-chip platform for large-scale drug screening applications *Lab Chip* **17** 511–20.

[131] Jusoh N, Oh S, Kim S, Kim J and Jeon N L 2015 Microfluidic vascularized bone tissue model with hydroxyapatite-incorporated extracellular matrix *Lab Chip* **15** 3984–8.

[132] Adriani G, Ma D, Pavesi A, Kamm R D and Goh E L K 2017 A 3D neurovascular microfluidic model consisting of neurons, astrocytes and cerebral endothelial cells as a blood-brain barrier *Lab Chip* **17** 448–59.

[133] Zervantonakis I K, Hughes-Alford S K, Charest J L, Condeelis J S, Gertler F B and Kamm R D 2012 Three-dimensional microfluidic model for tumor cell intravasation and endothelial barrier function *Proc. Natl. Acad. Sci. U. S. A.* **109** 13515–20.

[134] Legant W R, Pathak A, Yang M T, Deshpande V S, McMeeking R M and Chen C S 2009 Microfabricated tissue gauges to measure and manipulate forces from 3D microtissues

Proc. Natl. Acad. Sci. U. S. A. **106** 10097–102.

[135] Zimmermann W H, Melnychenko I, Wasmeier G, Didie M, Naito H, Nixdorff U, Hess A, Budinsky L, Brune K, Michaelis B, Dhein S, Schwoerer A, Ehmke H and Eschenhagen T 2006 Engineered heart tissue grafts improve systolic and diastolic function in infarcted rat hearts *Nat. Med.* **12** 452–458.

[136] Jackman C P, Carlson A L and Bursac N 2016 Dynamic culture yields engineered myocardium with near-adult functional output *Biomaterials* **111** 66–79.

[137] Vunjak-Novakovic G, Bhatia S, Chen C and Hirschi K 2013 HeLiVa platform: integrated heart-liver-vascular systems for drug testing in human health and disease *Stem Cell Res. Ther.* **4** 8-14.

[138] Stoehr A, Hirt M N, Hansen A, Seiffert M, Conradi L, Uebeler J, Limbourg F P and Eschenhagen T 2016 Spontaneous formation of extensive vessel-like structures in murine engineered heart tissue *Tissue Eng. - Part A* **22** 326–35.

[139] Lind J U, Busbee T A, Valentine A D, Pasqualini F S, Yuan H, Yadid M, Park S J, Kotikian A, Nesmith A P, Campbell P H, Vlassak J J, Lewis J A, Parker 2017 Instrumented cardiac microphysiological devices via multimaterial three-dimensional printing *Nat. Mater.* **16** 303–8.

[140] Wagner I, Materne E M, Brincker S, Sussier U, Fradrich C, Busek M, Sonntag F, Sakharov D A, Trushkin E V, Tonevitsky A G, Lauster R and Marx U 2013 A dynamic multi-organ-chip for long-term cultivation and substance testing proven by 3D human liver and skin tissue co-culture *Lab Chip* **13** 3538–47.

[141] Kim J Y, Fluri D A, Marchan R, Boonen K, Mohanty S, Singh P, Hammad S, Landuyt B, Hengstler J G, Kelm J M, Hierlemann A and Frey O 2015 3D spherical microtissues and microfluidic technology for multi-tissue experiments and analysis *J. Biotechnol.* **205** 24–35.

[142] Kelm J M, Timmins N E, Brown C J, Fussenegger M and Nielsen L K 2003 Method for generation of homogeneous multicellular tumor spheroids applicable to a wide variety of cell types *Biotechnol. Bioeng.* **83** 173–80.

[143] Jackson-Holmes E L, McDevitt T C and Lu H 2017 A microfluidic trap array for longitudinal monitoring and multi-modal phenotypic analysis of individual stem cell aggregates *Lab Chip* **17** 3634–42.

[144] Jackson E L and Lu H 2016 Three-dimensional models for studying development and disease: moving on from organisms to organs-on-a-chip and organoids *Integr. Biol.* **8** 672–

83.

[145] Miller P G and Shuler M L 2016 Design and demonstration of a pumpless 14 compartment microphysiological system *Biotechnol. Bioeng.* **113** 2213–27.

[146] Bauer S, Wennberg Huldt C, Kanebratt K P, Durieux I, Gunne D, Andersson S, Ewart L, Haynes W G, Maschmeyer I, Winter A, Ammala C, Marx U and Andersson T B 2017 Functional coupling of human pancreatic islets and liver spheroids on-a-chip: towards a novel human ex vivo type 2 diabetes model *Sci. Rep.* **7** 1–11.

[147] Wikswo J P, Curtis E L, Eagleton Z E, Evans B C, Kole A, Hofmeister L H and Matloff W J 2013 Scaling and systems biology for integrating multiple organs-on-a-chip *Lab Chip* **13** 3496–511.

3

Microfluidic 3D Platform to Evaluate Endothelial Progenitor Cell Recruitment by Bioactive Materials

In this chapter, we start by introducing the current preclinical models used to evaluate neovascularization and present the state of the art regarding microphysiological vascular models, showing the clear lack of adoption of these systems for testing biomaterials. The rest of the chapter is focused on describing our contribution to the field by presenting a novel microfluidic-based 3D model to evaluate the effect of bioactive biomaterials capable of releasing signaling cues (such as ions or proteins) in the recruitment of endogenous endothelial progenitor cells, a key step in the vascularization process. The usability of the platform is demonstrated using experimentally-validated finite element models and migration and proliferation studies with rat endothelial progenitor cells (rEPCs) and bone marrow-derived rat mesenchymal stromal cells (BM-rMSCs). As a proof of concept of biomaterial evaluation, the response of rEPCs to an electrospun composite made of polylactic acid with calcium phosphates nanoparticles (PLA+CaP) was compared in a co-culture microenvironment with BM-rMSC to a regular PLA control. Our results show a significantly higher rEPCs migration and the upregulation of several pro-inflammatory and proangiogenic proteins in the case of the PLA+CaP. The effects of osteopontin (OPN) on the rEPCs migratory response were also studied using this platform, suggesting its important role in mediating their recruitment to a calcium-rich microenvironment. This new tool could be applied to screen the capacity of a variety of bioactive scaffolds to induce vascularization and accelerate the preclinical testing of biomaterials.

3.1 Introduction

3.1.1 Preclinical models to study neovascularization

Neovascularization can occur by two mechanisms: during embryogenesis, blood vessel formation occurs by the migration of angioblasts (endothelial precursors generated in the bone marrow), which assemble into networks and differentiate into endothelial cells (EC), a process known as vasculogenesis (see **Fig.4-a**). This process also takes place in adult development by the recruitment of endothelial progenitor cells (EPCs) from the bone marrow [1]. After the formation of this primary network, vascularization can also occur by the cell sprouting from pre-existing vessels, a process known as angiogenesis (see **Fig.4-b**). This process involves proliferation, migration, tube formation, and anastomoses (creation of a functional connection with the pre-existing vasculature) [2].

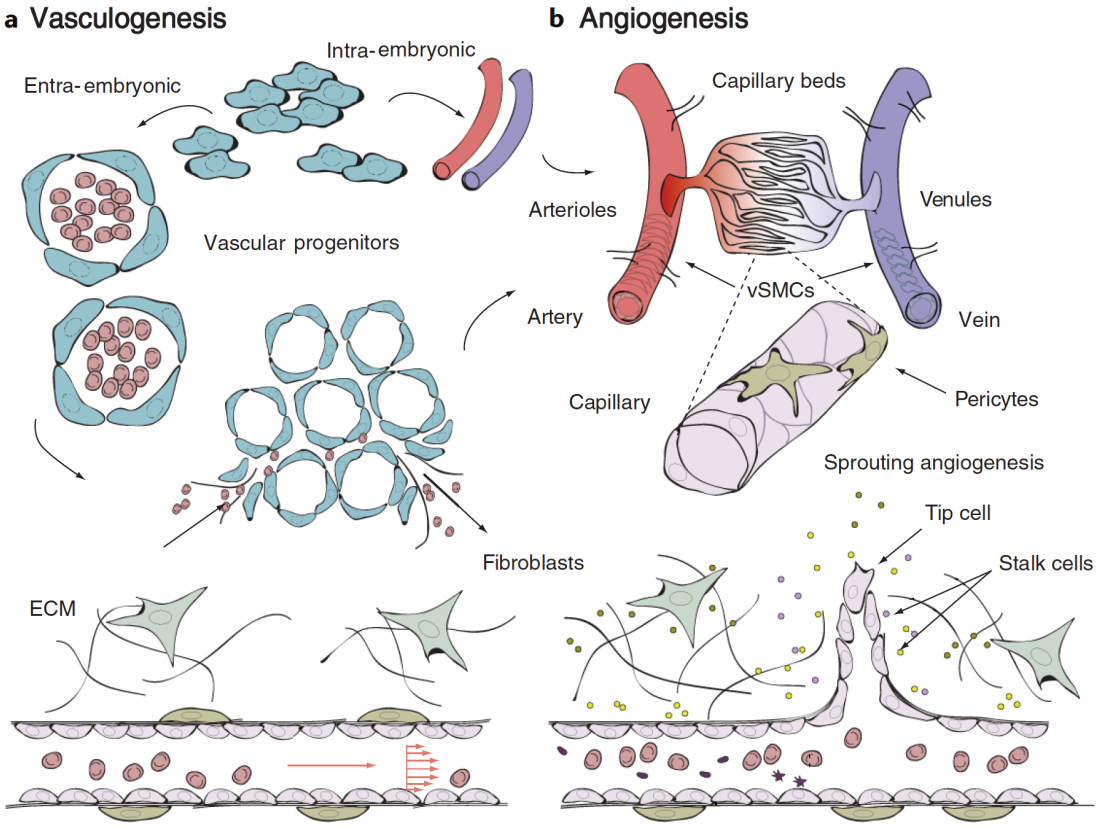

Figure 4 Neovasculature formation *in vivo*. (a) Vasculogenesis occurs when endothelial progenitor cells generated in the bone marrow travel through the bloodstream to the site of injury, forming networks and eventually differentiating into mature endothelial cells. **(b)** Angiogenesis occurs when endothelial cells remodel their extracellular matrix and start proliferating and migrating from the preexisting vessel, generating endothelial sprouts. *Adapted from [3].*

Maturation towards larger vessels occurs due to the action of supporting cells, mainly pericytes (for capillaries), fibroblasts and smooth muscle cells (for larger vessels such as arteries), which play a key role in stabilizing and controlling the growth of the endothelial network. These cells

tend to wrap around the endothelial wall and be involved in the secretion of ECM proteins, mainly collagen and elastin [4]. Neovascularization is a complex process orchestrated by a myriad of signalling molecules such as adhesion proteins, growth factors and inhibitors [5]. Among them, the vascular endothelial growth factor (VEGF) is one of the most relevant proteins driving EC recruitment and proliferation [6]. This growth factor is secreted by many different cells including fibroblasts, macrophages or lymphocytes and its release can be activated by oncogenes, cytokines and environmental conditions, such as oxygen depletion (hypoxia) through the release of the hypoxia-inducible factor (HIF-1), or mechanical cues like the shear flow [7]. Understanding neovascularization is therefore a critical point when evaluating a biomaterial for regeneration. On the one hand, preclinical ***in vitro* assays** are mainly based on the use of EC are aimed at studying the three main stages involved in vasculature formation:

- **Proliferation assays**: These assays are widely used due to their high reproducibility, high-throughput and precise quantification [8]. There are mainly two possibilities to quantify proliferation, either determining the net cell number using electronic counters (such as the Coulter counter) or colorimetric tests such as the MTT assay; or alternatively quantifying DNA synthesis using DNA-binding molecules such as in the bromodeoxyuridine (BrdU) assay, in which cell division is directly correlated to the amount of BrdU [9]. One of the main concerns with these tests is that the synthesis of DNA does not only occur during cell proliferation or that a decrease in cell number could be due to cytotoxic effects [8].

- **Migration assays:** ECs tend to move according to gradients of angiogenic molecules such as VEGF or bFGF, a process known as chemotaxis. This phenomenon has been traditionally studied *in vitro* using assays such as the Boyden chamber (see **Fig.5-a**), in which cells are seeded on top of a membrane (usually coated with an ECM protein as collagen) which separates an upper compartment with control media and a lower one with the angiogenic factor. This assay is highly sensitive to small differences in concentration gradients, but has several drawbacks, as the gradient dissipates over a short period of time (hours), it is difficult to accurately count cells through the filter and cells are seeded on an artificial substrate that does not mimic the actual *in vivo* environment [10]. A different approach to evaluate migration is the scratch wound assay starting from a confluent EC monolayer in which a portion of it is removed using a cell scraper. The cells then migrate to re-form the monolayer (wound healing process) and migratory activity is microscopically quantified [11]. The main limitation of this assay is the difficulty of mimicking identical confluence conditions and scraped areas in different replicates, the interference of cell proliferation and difficulty of quantification [12].

- **Differentiation assays:** when EC differentiate, they tend to form capillary-like structures that can be studied in vitro. In these assays, cells are generally seeded in 2D on top of an ECM

consisting of fibrin, collagen or Matrigel (a mix of ECM and basement membrane proteins derived from a mouse Engelbreth-Holm-Swarm sarcoma [13]) and the attachment, migration and tube formation is evaluated in a short timespan (usually less than 24 h) when they are exposed to cytokines or growth factors [14] (see **Fig.5-b**). An alternative approach is to sandwich the EC between two layers of the protein matrix and culture them for longer times (1-2 weeks) in order to model a 3D environment [15]. Some of the problems with this experimental approach are related to the fact that the materials used already have angiogenic properties (Matrigel for instance includes many growth factors in its formulation) resulting in a homogenous tubule formation that can be difficult to quantify [16]. Moreover, tube formation is not specific to EC, as it has been shown that human fibroblasts or glioblastoma cells are also able to form tubes on these substrates, and lumen formation is hardly ever observed in these assays, indicating a poor differentiation [16]. One of the ways to tackle this problem has been the creation of co-cultures with stromal cells such as fibroblasts or smooth muscle cells. This assay has been shown to better mimic the actual capillary bed found *in vivo* but is highly time-consuming (12-14 days) and less characterized as the molecules secreted by the supporting cells are not well-defined [17].

- **Organ culture assays:** following the idea of the co-culture approach to better mimic the actual cell microenvironment, assays using vascular extracts from animal models have been adopted, as they include all the stromal cells and the supporting matrix [18]. On top of that, the ECs are in their actual quiescent state (non-proliferative), which is more representative of the *in vivo* situation. The most commonly used assay is the rat aortic ring assay, in which an explant from the aortic ring is seeded in an ECM matrix (such as fibrin) and the sprouting of endothelial cells is monitored for a period of 10-14 days [19] (see **Fig.5-c**). The key limitations of this strategy are that it is based on the use of non-human cells, that large vessels are not the best model for angiogenesis, as it is generally a microvascular event, and that using different animals completely changes the endothelial response, reducing a lot the reproducibility [20].

One of the general problems with in vitro assays is that the used ECs have important phenotypic differences, especially between the ones derived from large vessels, such as the human umbilical vein endothelial cells (HUVEC) or from a microvascular origin, such as the human dermal microvascular endothelial cells (HuDMEC) [21]. It has been shown that depending on their origin, the response to growth factors and other molecules is different. Moreover, when cells are extracted and cultured in vitro, the quiescent phenotype found in vivo is lost, becoming proliferative and experimenting with changes in their surface antigens [22]. Their behaviour also changes depending on the ECM used or if they are cultured in static or dynamic flow conditions. These difficulties in mimicking the complex physiological interactions make *in vivo* models a

necessary step in the preclinical evaluation of a biomaterial. The main types of ***in vivo*** **assays** to evaluate neovascularization are the following:

- **Sponge or polymer implantation assay:** in this method, the implantation of a polymeric sponge containing the angiogenic factors or cells, either directly injected or added as pellets is performed in different animal models (rats, mice, rabbits, etc.) [23]. An alternative approach is to resuspend the tested substance in Matrigel, which is in a liquid form under 4 ºC, but when injected subcutaneously at body temperature (37 ºC) quickly forms a solid plug that allows a controlled release [24]. The formation of neovasculature is assessed after a given time by performing either an immunohistological staining of the sponge with endothelial-specific markers (such as CD31), assessing the haemoglobin content or using a radioactive tracer [25]. The main limitations of this approach are related to the heterogeneity in the sponges' sizes, shape and composition and the non-specific angiogenic responses due to unexpected immune responses [23].

- **Chick chorioallantoic membrane assay:** it is the most commonly used assay to evaluate angiogenesis and consists of the implantation in a 7-8 day old chick embryo of a polymer sponge or a plastic disc in which the tested chemical is loaded, either through a window cut in the eggshell or in shell-less embryos cultured in Petri dishes [26] (see **Fig.5-d**). The number of vessels converging towards the implanted pellet is then counted using a stereomicroscope. The popularity of this assay stems from its low cost and technical simplicity, although it has many drawbacks such as the presence of an already well-developed vasculature that difficult the process of identifying new capillaries, the potential inflammatory response generated by debris like shell dust or the high sensitivity to oxygen tensions [20].

- **Corneal angiogenesis assay:** this assay is based on the use of corneal tissue, which is avascular, making the identification of new capillaries stemming from the corneal limbus easily identifiable [27]. It requires performing a small cut in the corneal tissue of the animal (generally rabbits but also rats or mice) to create a “pocket” in which a polymeric pellet loaded with the test substance is placed [28]. Microscopic imaging is then performed to analyse the number of capillaries penetrating the cornea. The main disadvantage of this assay is that it is technically demanding and not suitable for large-scale screening [8].

- **Chamber assays:** they rely on the use of transparent chambers placed in a piece of skin (rabbit ear, mouse dorsal skinfold) or bone (skull), previously placing a gel containing the test molecule on the exposed surface and then covering it with glass and closing the chamber to secure it [24]. The quantification is then performed by acquiring microscopy images. It is a highly interesting assay because it allows for the continuous monitoring of 3D vessel growth (typically for 1-3 weeks). However, these assays are invasive, technically complex, and highly expensive [23].

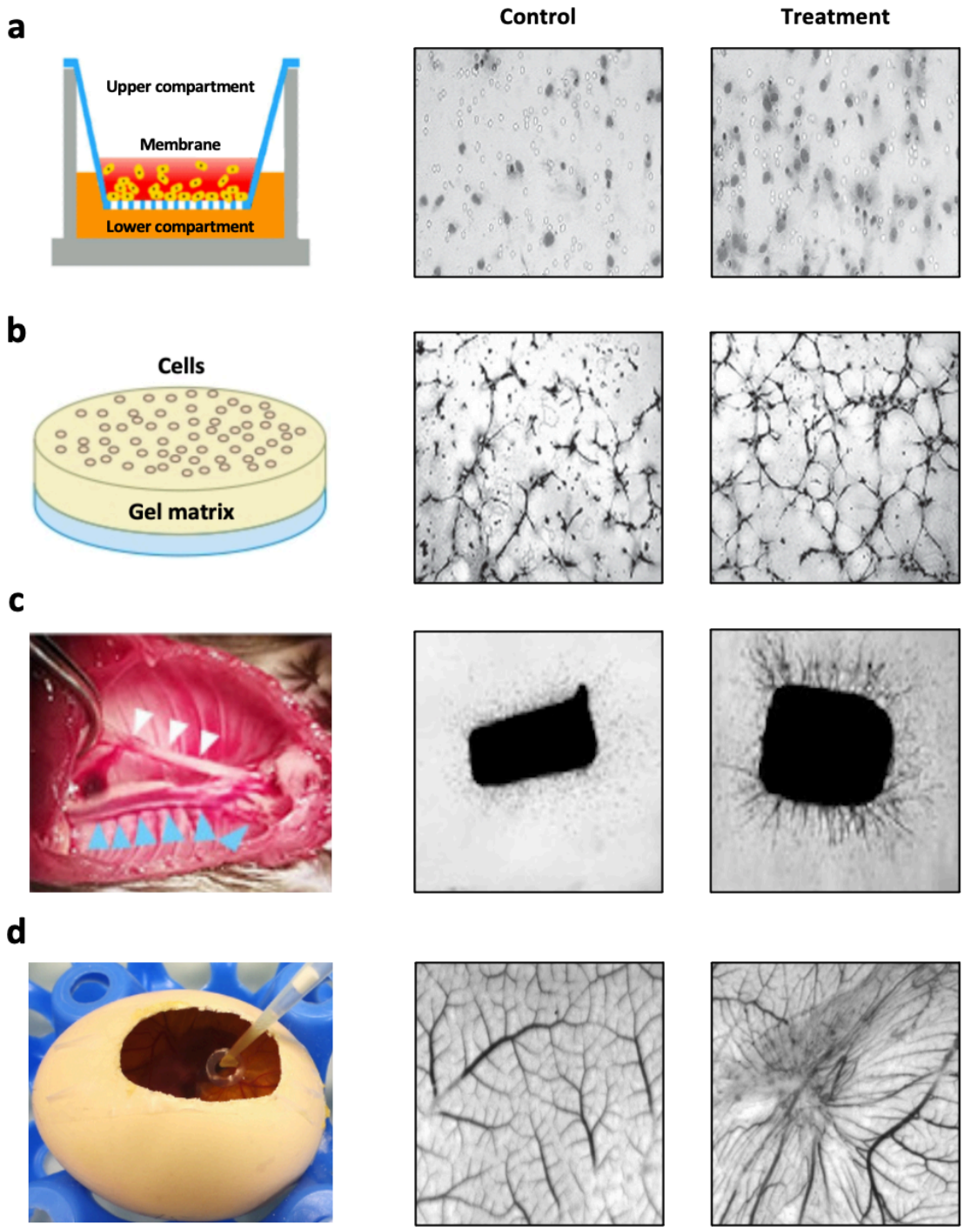

Figure 5 Representative preclinical assays to assess neovascularization. (a) Endothelial cell migration *in vitro* quantified using a Transwell assay. **(b)** Endothelial cell differentiation *in vitro* quantified using the tube formation assay on Matrigel. **(c)** Organ culture *in vitro* of a mouse aortic ring. **(d)** Angiogenesis assay performed *in vivo* on a chick chorioallantoic membrane (CAM). *Adapted from [8].*

3.1.2 Microphysiological models of vascular tissue

Microfluidic models have evidenced to be an invaluable tool for the study of microvasculature development and pathology. Proposed designs can be grouped in two distinct categories

depending on how the vessels are generated. patterned or self-assembled network formation. The first one is the **patterned formation approach**, which is based on the use of a temporal scaffold or sacrificial mould to generate the desired geometry. One of the studies pioneering this method was based on the generation of a single perfusable microvessel (75-100 μm) by seeding EC in the hollow regions left by microneedles inserted in a collagen gel and removed after polymerization. These vessels maintained a stable cylindrical shape and a functional barrier function under hydrostatic flow (1-4 Pa) for 2-3 weeks [29]. Other researchers developed similar techniques as endothelial monolayers in gold-sputtered rods [30] or silica capillary tubes [31]. First attempts to create microvessel networks have relied on the use of soft-lithography to generate PDMS moulds with a series of interconnected channels, that were then used as stamps on biodegradable hydrogels. After polymerization, the stamp is removed and hollow channels are seeded with endothelial cells [32,33]. A similar approach is subtractive scaffolding, in which a sacrificial template, generally hydrogels such as gelatin [34], alginate [35] or PEG [36], is mixed within a collagen or fibrin matrix. After the dissolution of the sacrificial layer, those hollow spaces are seeded with EC. More complex patterns can be generated by imaging actual *in vivo* capillary networks and then using that pattern to guide a laser-assisted degradation of hydrogels, which results in highly biomimetic geometries [37]. The main limitations of the patterned network formation methodology are the limited control over hydrogel distribution and the long times needed by some of the systems to generate functional vessels (up to 2 weeks), which can lead to undesired gel degradation by the cells and disruption of the angiogenic growth [3].

Regarding the **self-assembling approach**, it is generally inspired by the naturally occurring vascularization mechanisms. One of them is angiogenesis, in which endothelial cells sprout from a pre-existing vessel, which in microfluidic systems can be mimicked in several ways. One of them is the use of microcarrier beads coated with EC, which are then resuspended in a fibrin gel that shows a sprouting behaviour after around 2 days when treated with VEGF [38]. This system was used to illustrate the essential role of stromal cells in driving angiogenesis, as it was shown that transforming growth factor β (TFG- β) or angiotensin 1 (ANG-1) are only able to stimulate angiogenesis in the presence of fibroblasts [39]. A different approach is the use of PDMS microfluidic devices with chambers delimited by arrays of microposts, in which the surface tension generated by the hydrophobicity of the polymer and the precise spacing of the microstructures is used to spatially confine hydrogels during the injection. After cross-linking adjacent microchannels are filled with media and EC seeded in the gel-media interface. These systems or multi-chamber modifications have been used to study the effects of growth factors, cytokines, adhesion molecules, or paracrine signalling in co-culture conditions [40-42]. For instance, a gradient of VEGF and sphingosine-1-phosphate (S1P) was generated in the hydrogel

chamber by putting these chemoattractants on one of the side channels and control media on the cellular side to study their effect on length and direction of the endothelial sprouting [43].

This type of designs can also be used to recreate vasculogenesis by injecting the EC resuspended in a hydrogel in one of the chambers and encapsulate stromal cells in different ones, allowing paracrine signalling that results in an endothelial network formation in 24 h and lumen formation in 4 days [44]. A similar self-assembling approach has been used in a different device, in which an array of diamond-shaped chambers limited by small pores (30 μm) was used to confine the cell suspension by the phenomena of capillary burst valve. The microvascular network was able to anastomose to the EC-lined side channels through the pores, and it was then perfused by a hydrostatic pressure gradient that mimics the arterial to venous capillary flow [45]. These microvascular networks have shown a great potential for modelling physiologically relevant events. For instance, HUVECs cultured in the presence of human lung fibroblasts formed a perfusable network after 4 days that has been used to study trans-endothelial migration of tumour cells, showing that tumour necrosis factor α (TNF-α) increased vessel permeability and cancer cell extravasation [46]. The most relevant limitations of self-assembling systems are related to the PDMS mould, which has been shown to influence the morphology of the endothelial channels, prevent vasodilation/constriction phenomena and absorb small hydrophobic molecules [47].

Interestingly, these approaches have been adapted to mimic specific vascularized tissues. For example, several studies have put forward models of the blood-brain barrier, which is a specialized vasculature structure in the brain composed of ECs surrounded by pericytes and astrocytes [48]. It is characterized by an extremely restrictive permeability that allows only the transportation of small molecules and gases while preventing the entrance of drugs, bacteria, etc. [49]. A disfunction of this barrier is related to several neurological disorders such as Alzheimer's or Parkinson’s diseases [50]. A microphysiological platform based on collagen gel confinement using PDMS microposts (4-chamber design) and cellular self-assembly, demonstrated the viability of co-culture of neurons, astrocytes, and EC, resulting in tight-junction expression and permeability levels close to the *in vivo* values [51]. Other vascularized tissue barrier models have been proposed, such as the lung alveolar-capillary interface, which was modelled by co-culturing human pulmonary microvascular EC with alveolar epithelial cells on a polymeric porous membrane [52]. The skin has also been mimicked by generating a perfusable 3D microvessel within an epidermis-dermis, allowing for the screening of cosmetic and pharmaceutical molecules [53]. Examples of parenchymal tissues include vascularized liver tissue, which has been modelled in a microfluidic device by co-culturing hepatocyte spheroids with fibroblasts and EC, resulting in a higher secretion of albumin, urea and cytochrome P-450 compared to hepatocyte monocultures [54]. Models of bone tissue have also been proposed by tri-culturing MSC and

osteoblasts with EC, which self-assembled in a perfusable microvascular network that was used to study tumour cell extravasation [55].

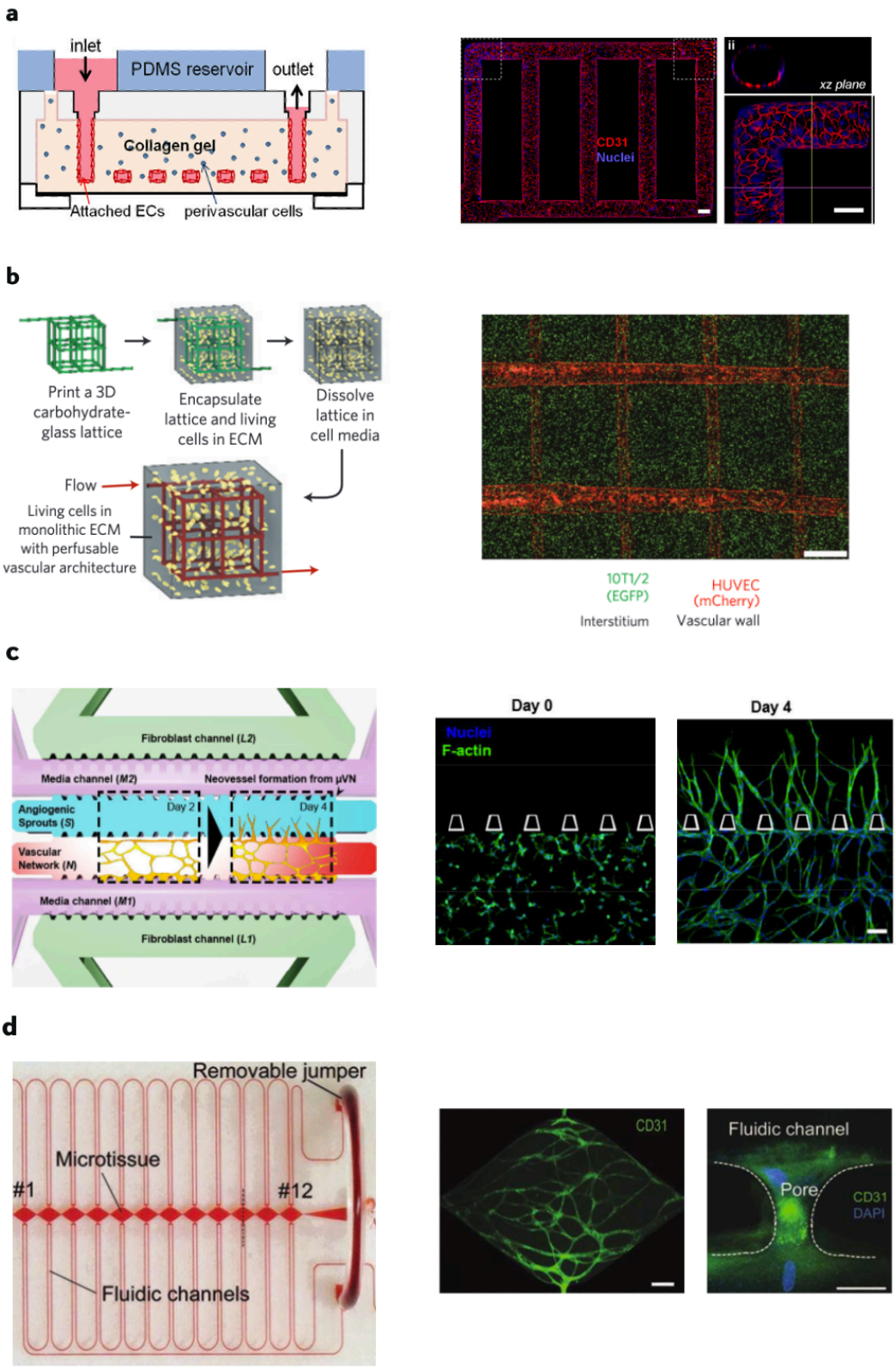

Figure 6 Microphysiological systems to model vascular tissue. (a) Vascular network generated using a hydrogel patterning method based on a PDMS stamp. (**b**) Microvessel network generated using a sacrificial scaffold made of

dissolvable carbohydrate glass. (**c**) Hydrogel confinement using PDMS microposts allowing endothelial cell self-assembling to study angiogenesis. (**d**) Self-assembled network based on the co-culture of human lung fibroblasts with endothelial cells in a hydrogel anastomosed to the lateral fluidic channels. *Adapted from [3].*

In the described vascular models, the **evaluation of vessel functionality and maturation** is generally based on microscopical analysis [56]. For instance, number and length of branches, vessel diameter and total area are indicative of the quality of the microvascular network [44,57]. Immunofluorescence staining for proteins such as CD-31, von Willebrand factor (vWF) or vascular-endothelial cadherin (VE-cadherin) are indicative of the endothelial phenotype [58]. The presence of tight junction proteins such as zonula occludens-1 (ZO-1), laminin and collagen IV (basement membrane proteins) are commonly used as markers of vessel maturity [59]. Another key parameter indicative of mature vessels is their permeability, which can be evaluated by using the Huxley method, which is based on the perfusion a fluorescent marker (such as FITC-dextran) through the lumenized vessels and evaluating the linear relationship between fluorescence intensity and fluorophore concentration in the extracellular space [60]. This method has proved to be an excellent way to estimate barrier function, although it has been recognized that in vitro values tend to be one or two orders of magnitude higher than *in vivo* [61]. This is due to the current lack of some functional elements regulating vessel permeability, such as the glycocalyx and fully developed basal lamina, as well as the neglection of convective transport in the model [62].

From all these different platforms, very few of them have been actually used to evaluate biomaterials [63,64], which motivated us to propose an novel microfluidic-based assay to actually be able to study the effect of calcium-releasing biomaterials on endothelial progenitor cell recruitment. To achieve this goal, we designed, fabricated, and validated the capacity of the proposed microfluidic platform to generate gradients of soluble factors using a finite element model (FEM) of diffusion. We evaluated the suitability of the platform to study 3D migration to inorganic ions by evaluating the response of bone marrow-derived rat mesenchymal stem cells (BM-rMSC) and rat endothelial progenitor cells (rEPC) to gradients of calcium. We then implemented an assay to study the migratory response of rEPC to calcium-releasing scaffolds in a co-culture microenvironment with BM-rMSC. We also screened the release profile of several pro-angiogenic and inflammatory cytokines and performed an in-depth study of the role of osteopontin in mediating the response of rEPC to high extracellular calcium levels. Overall, we believe that the presented microfluidic assay could be of great interest to performing preclinical studies with materials for bone tissue engineering and better understanding of the different elements involved in the complex process of vascularization.

3.2 Materials and methods

3.2.1 Cell culture

Bone marrow-derived rat endothelial progenitor cells (rEPC) and mesenchymal stem cells (BM-rMSC) were obtained from the long bones of young Lewis rats (2-4 weeks old) following previously published protocols [65,66]. Briefly, the bone marrow was obtained from the rat's long bones by flushing adhesion medium M199 (Sigma, DE) supplemented with 20 % fetal bovine serum, 1 % pyruvate, 1% penicillin/streptomycin, 1 % L-glutamine (all reagents from Thermo Fisher, US) and 22 µg/ml heparin (Sigma, DE). The whole fraction was plated in 6-well plates and incubated for 24 h. Most adherent cells attached to the dish during this time were BM-rMSC, which were subsequently plated in T75 flasks (Thermo Fisher, US) and cultured in α-minimal essential medium (α-MEM) supplemented with 10 % FBS, 1 % Pen/Strep, and 1 % L-glutamine (all reagents from Thermo Fisher, US) for no more than 5 passages. The cell lineage was confirmed by positive staining for Stro1, CD105, CD44, which are generally accepted markers for this lineage [67]. The cells in suspension were recovered and plated in new dishes for another 24 h. On the third day, the suspension fraction was highly enriched in hematopoietic cells, which were recovered and plated in T75 flasks and further cultured in Endogro media (Merck Millipore, DE) for no more than 5 passages. The endothelial progenitors showed weak positive staining for Flk-1, CD-34, CD-31, and vWF, which is generally indicative of an immature, endothelial-progenitor-like state [68]. All cells were cultured in a humidified 5 % CO2 incubator at 37 ºC.

3.2.2 Device design and fabrication

The design of the microfluidic platform (see **Fig.7-a,b**) was performed using computer-aided design software (AutoCAD 2019, Autodesk, US) and consists of 2 cell culture chambers (1300 µm x 8800 µm x 150 µm) in contact with 2 cell culture media channels (750 µm wide, 150 µm high) separated among them by a central channel (1000 µm wide, 150 µm high). Master molds were produced using photolithography with a SU8-3050 photoresist (MicroChem, DE) and 4'' Si wafers as supports. All procedures were performed in a cleanroom environment. Polydimethylsiloxane elastomer (PDMS, Sylgard 184, Dow Corning) was used at 10:1 w/w (base: curing agent). After degassing and curing overnight at 65 ºC, the PDMS was carefully removed from the silicon wafer, separated into individual chips, and perforated producing 6 mm holes for reservoirs and 1 mm holes for chamber inlets. Chips were cleaned and bonded to glass rectangular supports (0.17 mm thick coverslips) by air plasma treatment (Harrick Plasma PCD-002-CE) for 0.5 min at 10.5 W. In the case of biomaterial testing, the used coverslips were patterned with PLA nanofibers (more details in methods section 2.4), and fibers outside the stromal cell chamber area were carefully removed before the plasma treatment with a cloth wetted

in acetone (Panreac, ES). Finally, all the chips were cured at 85 ºC for 12 hours to strengthen the bonding. Devices were sterilized by placing them in the plasma chamber and repeating the previously described process.

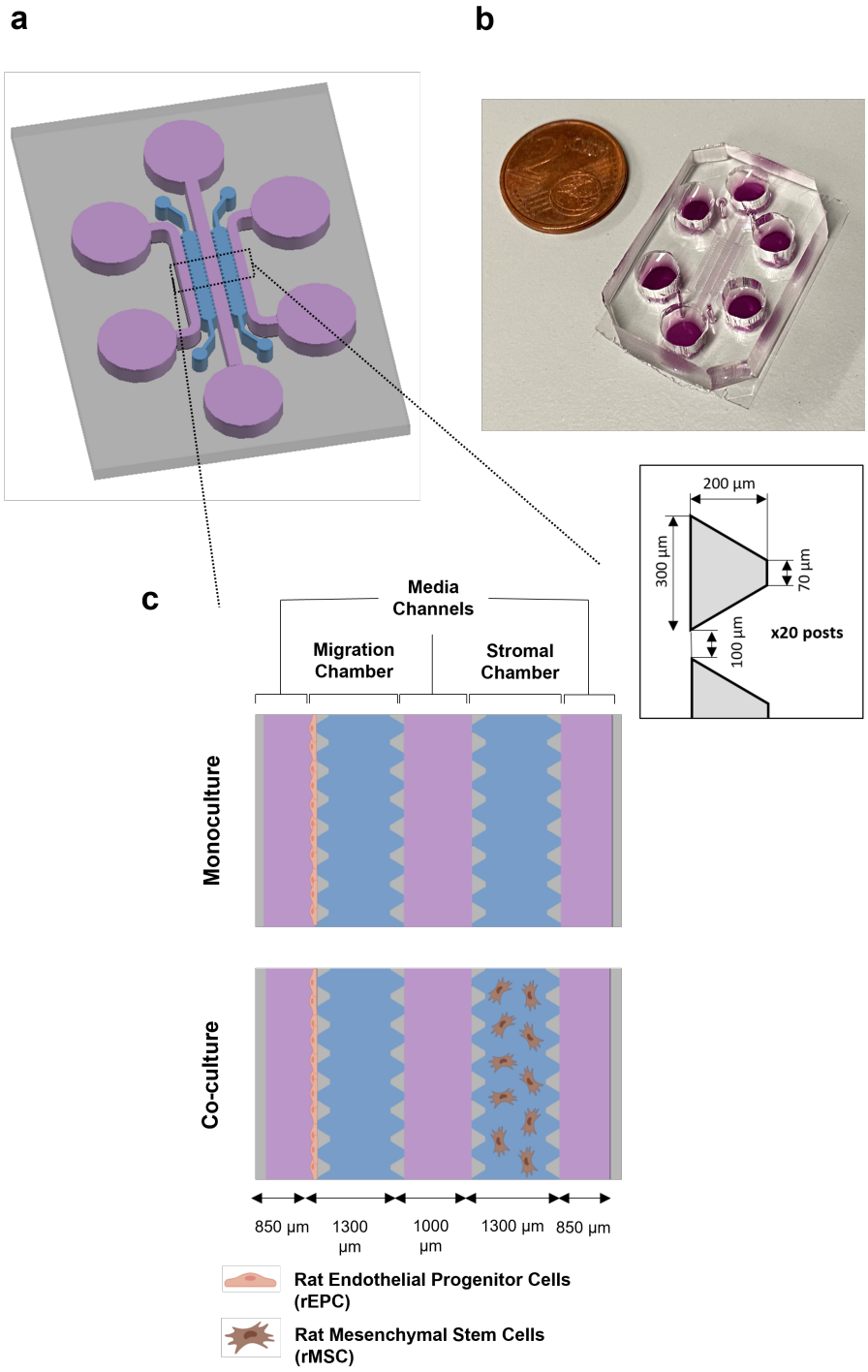

Figure 7 Microfluidic assay to study rEPC recruitment. (**a**) Scheme of the device showing the 2 cell chambers (blue) and the media channels (purple). (**b**) Picture featuring the final assembled platform. (**c**) Comprehensive view detailing how cells are cultured in the device, either in monoculture (just one cell type, migration caused by the addition of a chemoattractant to the cell media) or co-culture conditions (two cell types, migration induced by the secretions of the cells located in the stromal cell chamber).

3.2.3 Finite element model of protein transport and validation

An *in silico* model of the device was developed using the finite element method (FEM) to evaluate if a concentration gradient could be obtained in the migration chamber from the secretions produced by the BM-rMSCs. The creation of such a gradient is based on the passive diffusion of the protein of interest through the porous hydrogel (fibrin) injected in the cell chamber area (migratory chamber). To study the diffusive process, the geometry of the platform was split into two domains with different diffusive properties: (1) the fluid area associated with the cell media, including the channels and reservoirs, and (2) the cell chambers filled with fibrin hydrogel. The concentration profile was calculated with COMSOL Multiphysics 5.6 (COMSOL Inc, US) using the *Transport of Diluted Species* interface, which in our particular case solves the mass conservation equation considering that there is no convective transport involved. This yields an equation corresponding to Fick's laws of diffusion:

$$\boldsymbol{J_i} = -D\nabla c$$

$$\frac{\partial c}{\partial t} = \nabla . \boldsymbol{J_i} + R$$

Where J_i (mol m^{-2} s^{-1}), is the diffusive molar flux vector, which evaluates the amount of substance that flows through a unit of the area during a unit time interval, c (mol m^{-3}) is the concentration of the chemical species of interest, D (m^2 s^{-1}) the diffusion coefficient and R (mol m^{-3} s^{-1}) the reaction rate of the considered species. A no flux boundary condition was selected for all walls of the system. A tetrahedral mesh with approximately 215,000 elements was used and solved based on the PARDISO approach. The reliability of the results was controlled by different mesh sensitivity processes.

In our case, we were interested in studying the diffusion of the osteopontin protein, which has an approximate molecular weight of 31 kDa, that is in the range of other well-known angiogenic factors such as VEGF, bFGF, or IGF [69]. The diffusion coefficient for molecules with that hydrodynamic radius is around $6x10^{-11}$ m^2/s in cell media and $4.9x10^{-11}$ m^2 s^{-1} in hydrogels such as collagen or fibrin [42,43]. The osteopontin secretion on day 3 was derived from an ELISA assay performed on BM-rMSCs (see methods section 3.2.8) and estimated to be approximately $1.41x10^{-12}$ mol m^{-3} s^{-1} (assuming a linear release profile).

To validate the computational model, we studied the concentration profile of a 40 kDa Texas Red conjugated dextran (Thermo Fisher, US), a non-reactive polymer with a comparable hydrodynamic radius to osteopontin. To perform the experiment, both cell chambers were loaded with the fibrin gel (2.5 mg/ml fibrinogen and 1 U/ml thrombin), one of the side channels filled with regular PBS and the remaining two with a solution of fluorescent dextran in PBS at an initial concentration of 25 µg ml^{-1}. Fluorescent images were acquired in a Leica AF7000 microscope

(Leica Systems, DE) at different time points (2.5 h, 5 h, 10 h, and 15 h) and images were processed with ImageJ software (NIH, US) to obtain the evolution of the fluorescent intensity profile. The area selected is located between the rows of posts 10 and 11 and the values were normalized using the intensity measurements from the fluorescent channel (maximum) and control channel (minimum). These results were compared to the values obtained in the finite element simulations (removing the reaction rate term), which were also normalized to allow for direct comparison.

3.2.4 Calcium-releasing biomaterial fabrication

The calcium-releasing biomaterial chosen for evaluation in our platform was based on CaP ormoglass nanoparticles (NP) prepared using a sol-gel process and the $CaO:P_2O_5:Na_2O:TiO_2$ 44.5:44.5:6:5 molar ratio composition reported by Sanzana et al. [70]. After obtaining the NP, they were resuspended at 25 % w/w (PLA+NP25) by ultrasonic dispersion in 4% w/w poly-L/DL lactic acid solution (Purasorb PLDL 7038, 70/30 L-lactide/DL-lactide copolymer, inherent viscosity midpoint 3.8 dl g^{-1}, molecular mass ≈ 850,000 Da, Corbion, NL) in 2,2,2-trifluoroethanol (TFE, 99 % Alfa Aesar, US). The plain PLA 70/30 solution was used to produce the control PLA fibers. 5 ml syringes (Becton-Dickinson, US) were loaded with the polymer solutions and pumped (NE-300, New Era Inc, USA) at a flow rate of 1 ml/h through a 21-gauge blunt-tip needle (Nordson EFD, US). A high-voltage power supply (NanoNC, KR) was used and fibers were collected onto a grounded cylindric collector located at 200 mm from the tip of the syringe. Rectangular fragments of aluminum foil (20x33 cm) were used to envelop the collector. Three 0.17 mm coverslips (Deltalab, ES) were secured with adhesive tape following the middle axis of the aluminum foil rectangle. A rotary speed of 1000 rpm was used to obtain aligned fibers. The deposition time was 10 min and the applied voltage was 15 kV.

3.2.5 Biomaterial morphology and calcium release characterization

The calcium ions release profile of the PLA+NP25 was measured by preparing three electrospun coverslips and bonding them to a PDMS block (7 mm in height). A custom-made device based on a PDMS block with a 10 mm punch hole in the middle of the block, previously removing most of the fibers outside the punched area as explained in the previous section. 500 µl of culture media obtained mixing α-MEM and Endogro media at 1:1 were added to each device. Samples were kept inside 100 mm Petri dishes in a 5 % CO_2 incubator at 37º C and the medium was replaced at different time points for a total period of 48 h. The calcium concentration of each replaced medium was obtained using the O-Cresophtalein complexone assay and measuring the absorbance of the samples using an Infinite M200 Pro plate reader (Tecan, CH). The shape of the fibers, previously coated with gold was featured using scanning electron microscopy with an electron source by field emission (NOVA Nano SEM 230, Fei Co., NL) at 10 kV.

3.2.6 Migration assays

Cells were seeded in the microfluidic system either in monoculture or co-culture conditions (see **Fig.7-c**). In the first case, both cell chambers were loaded with a fibrin gel obtained by mixing a fibrinogen solution at 2.5 mg/ml with 1 U/ml of thrombin (both reagents from Sigma, DE). In the co-culture experiments, the migration chamber was loaded with acellular fibrin and the stromal one with a solution consisting of $10x10^6$ cells ml^{-1}, either resuspended in a fibrin gel (10 µl) or directly seeded on top of the electrospun fibers. The devices were either incubated at 37 ºC for 15 min to allow for hydrogel polymerization or 1 h to allow BM-rMSCs to attach to the PLA fibers. The cells (just rEPCs in the case of co-culture conditions) were centrifuged and resuspended at a concentration of $1x10^6$ cells ml^{-1} and seeded in the device by putting 50 µl in the upstream reservoir of one of the side channels and aspirating from the other end. The devices were then tilted 90º and incubated for 45 min to allow for cell attachment.

In the case of the monoculture experiments, all reservoirs were filled with the regular cell media (approximately 150 µl/reservoir) and kept for 1 day under those conditions. During the next 2 days, the devices were either kept without supplementation or mixed with VEGF (Preprotech, US) at 100 ng ml^{-1} or $CaCl_2$ (Sigma, DE) at 10 mM in the acellular channels. The media was changed every 15 h in order to reset the concentration gradient in the migration chamber. In the co-culture experiments, the media of both cell populations was mixed at a 1:1 ratio, used during day 1 without supplementation (control) and for the next 2 days either in control conditions, supplemented with $CaCl_2$ at 10 mM or supplemented with $CaCl_2$ plus osteopontin neutralizing antibody (R&D Systems, MN, US) at 10 µg/ml. No changes of media were performed to avoid disrupting the gradient generated by the BM-rMSCs secretions. For biomaterial testing, no supplementation was used. In all cases, low serum (2 % FBS) conditions were considered. Each device was kept inside 100 mm Petri dishes in a 5 % CO_2 incubator at 37 º C. Three replicates were performed per experimental condition.

3.2.7 Immunostaining and cell migration quantification

The cells seeded in our microfluidic platform were fixed after 72 hours in culture with 4 % paraformaldehyde (Electron Microscopy Sciences, US) for 15 minutes after removing unreacted paraformaldehyde with sterile 1x PBS. After another 1x PBS washing, they were permeabilized with a Triton X-100 (Sigma, DE) solution at 0.1 % v/v in 1x PBS with glycine (Sigma, DE) at 0.15 % w/v (PBS-gly) for 15 min. Then, cells were stained by incubating them at room temperature for 2 h with a rhodamine-phalloidin (Thermo Fisher, US) solution at 1:200 in PBS-gly. A counterstaining for cell nuclei were also implemented by incubating 4′,6-diamidino-2-phenylindole (DAPI, Thermo Fisher, US) at 1:1000 in PBS-gly for 10 min at room temperature.

Samples were then washed three times in PBS-gly and maintained at 4 ºC in the same solution until acquisition.

Imaging was performed on a TCS SP-5 confocal microscope (Leica Microsystems, DE). Cell migration was quantified with a custom-made procedure using the software Image J-Fiji [71]. Briefly, the acquired images were projected as a *z*-stack (maximum intensity) and a reference line was drawn at half the microposts width (using the bright field channel) in order not to take into account any basal cell invasion of the gel. Then, the cartesian coordinates and the total number of migrated cells were automatically calculated from the DAPI channel using the *3D Objects Counter* plugin [72]. The migrated distance of each cell was calculated as the difference between the *x*-coordinates (or *y*-coordinates depending on how the chip was placed) and corresponding coordinates of the reference line at half the microposts width. One representative image in the middle of the cell chamber (between rows 10 and 11) was taken per chip from a total of 3 replicates in any experimental condition. Cell number was quantified only from the selected area.

3.2.8 Proliferation and protein expression assays

To perform the proliferation assay, $10x10^6$ cells ml^{-1} were seeded in the stromal chamber and resuspended in fibrin gel (10 µl) as previously explained. The rest of the device was filled either with control media or media supplemented with $CaCl_2$ at 10 mM (150 µl/reservoir). Cells were kept in culture for 3 days with a change of media after day 1. Proliferation was quantified by measuring the ratio of dsDNA in cell lysates using the PicoGreen kit at two-time points: 3 h after the initial seeding (to get an estimate of the initial amount of dsDNA) and after 3 days in culture. To obtain the lysates, cells were recovered from the devices after dissolving the fibrin gel by incubating with TrypLE (Thermo Fisher, US) for 45 min at 37 ºC in agitation. The cells were then centrifuged and resuspended in 300 µl of Tris-EDTA (Sigma, DE) and lysed by subjecting them to three freeze-thaw cycles. The PicoGreen assay was then performed following the manufacturer's instructions. Fluorescence measurements were performed in an Infinite M200 Pro plate reader (Tecan, CH). Three replicates were performed per condition and time point.

The conditioned media collected on day 3 from the devices seeded with BM-rMSC was used to measure the amount of OPN released by the cells. We also analyzed the conditioned media obtained on day 3 from the co-culture experiments using the biomaterials for several pro-angiogenic and inflammatory proteins (IL-1β, IL-6, OPN, IGF-2). In both cases, protein expression was analyzed using an ELISA kit (R&D Systems, US) following the manufacturer's instructions Absorbance measurements were performed in an Infinite M200 Pro plate reader (Tecan, CH). These values were normalized by the amount of dsDNA obtained for each of the samples. Three replicates were performed per experimental condition.

3.2.9 Statistical analysis

Prism 8.3 software (GraphPad Software, US) was used to statistically treat all generated data., which was tested for normality and presented and analyzed with the mean and the standard deviation or the median and the quartile. For 2 samples comparison, Student's t-test (unpaired, two-tailed distribution) was used, while for the multiple samples (unless otherwise specified) comparison with a one-way ANOVA was followed by a post-hoc Tukey's test. Statistical significance was considered from p-value < 0.05 (*).

3.3 Results and discussion

3.3.1 Microfluidic platform allows the generation of 3D protein gradients

To demonstrate the possibility of generating a protein gradient inside the proposed microfluidic platform, we created and validated a finite element model of the device for the transport of diluted species using a 40 kDa dextran. We chose this molecular weight because its diffusion coefficient is really close to that of several pro-angiogenic proteins such as VEGF, representing a diffusivity analog of those molecules [69,73,74]. We compared the simulation results with the experimental values for different time points in a total interval of 15 h (see **Fig.8-a**). It can be observed that the gradient becomes linear after approximately 2.5 h, with a progressive increase of the dextran concentration in the control channel from 0 to 0.125 µM (approximately 25 % of the maximum concentration), which can be reset by changing the media as previously explained in section 2.6. The average slope obtained in the finite element model when the gradient becomes linear (2.77×10^{-4} µM µm^{-1}) and the experimental one (2.88×10^{-4} µM µm^{-1}) are not significantly different ($p > 0.005$), which indicates that the computational model is able to adequately predict the behavior of our system. It is important to highlight that protein binding to the gel, as well as blocking and consuming mechanisms related to the rEPC monolayer, were neglected in order to perform the comparisons. This means that the dextran profile does not exactly mimic the real protein gradient, although it gives us important insight into the diffusion mechanisms in our system.

For the monoculture conditions, results obtained for the dextran experiments suggest that applying the VEGF at a concentration of 100 ng ml^{-1} would yield a linear gradient after about 2.5 h with an average slope of approximately 55 ng ml^{-1} that can be maintained for at least 12 hours. In the case of Ca^{2+}, it has been demonstrated that simple ions can freely diffuse in the high water content of the hydrogel [75], which implies that the gradient dissipates much faster. In fact, our simulations (see **Fig.9**) show that the calcium gradient dissipates over 1 h. However, the results presented in section 3.2 evidenced that this time interval is enough to activate cell migration

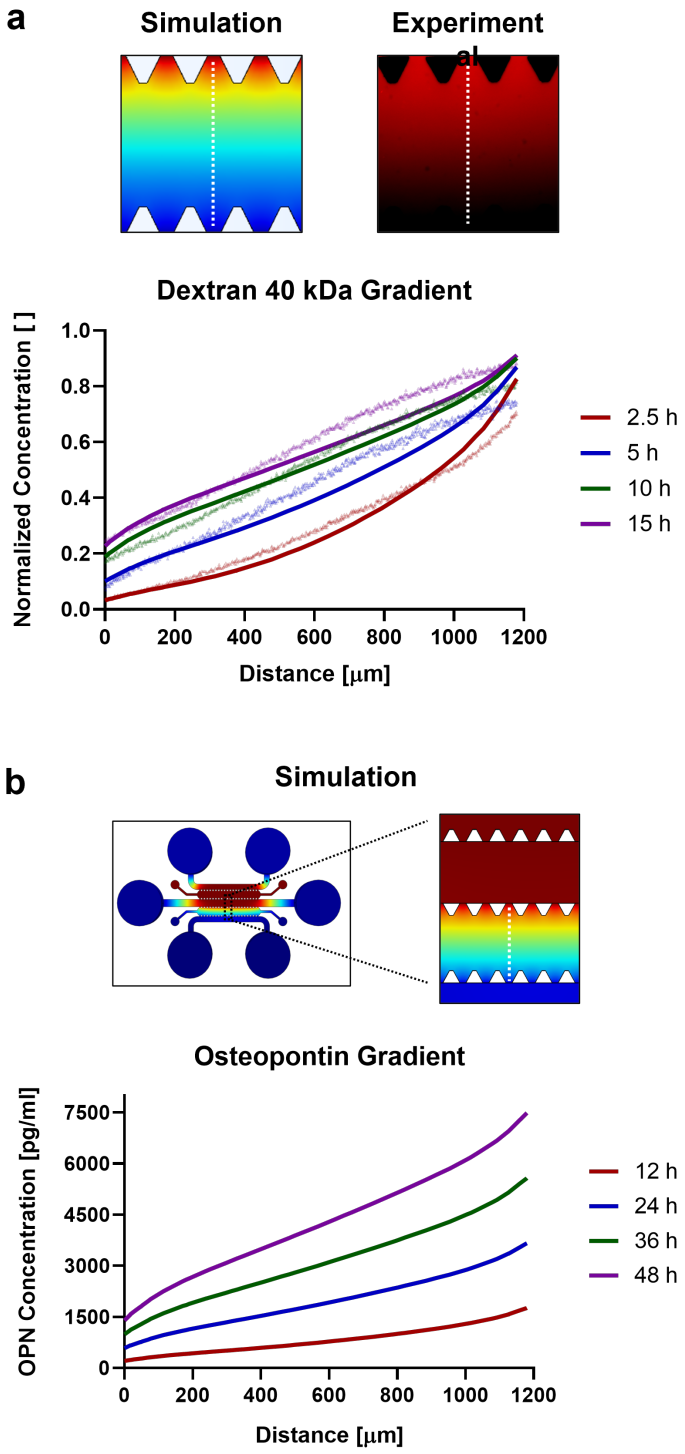

Figure 8 Finite element model of protein diffusion in microfluidic platform. (**a**) Comparison of the normalized concentration gradients obtained in the FEM simulations (solid lines) with the experimental fluorescence measurements (dotted lines) for different timepoints. (**b**) Computational model of the gradients generated by the BM-rMSC osteopontin secretions in the migration chamber for different timepoints. In both cases, the gradient profile corresponds to a transversal section of the cell chamber between rows of posts 10 and 11.

In the case of co-culture conditions, we utilized the finite element simulation to address how OPN gradient could be generated from the stromal chamber into the migration chamber. The

results show (see **Fig.7-b**) that linear gradients are generated with increasingly steeper slopes with the time in culture. For instance, after 24 h the gradient is 2.36 ng ml^{-1} mm^{-1}, increasing to 4.70 ng ml^{-1} mm^{-1} after 48 h. These results are in the range of previously reported studies with encapsulated human lung fibroblasts (hLF) [76], suggesting that the dimensions of the device allow paracrine communication between rEPCs and BM-rMSCs.

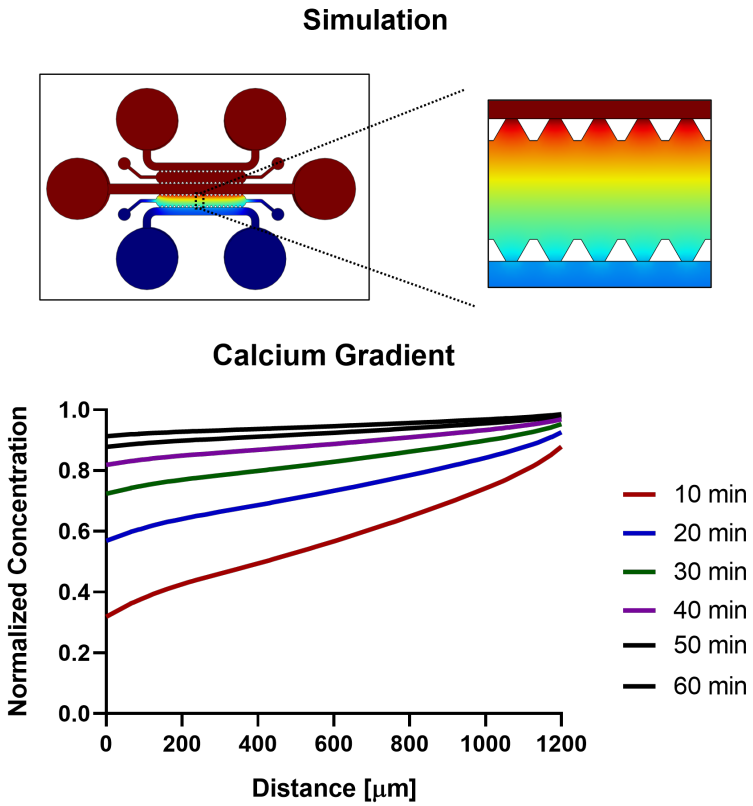

Figure 9 Finite element model of calcium chloride diffusion. Normalized concentration gradients obtained in the FEM simulations (solid lines) for different timepoints. In all cases, the gradient profile corresponds to a transversal section of the cell chamber between rows of posts 10 and 11.

3.3.2 Validation of the microfluidic platform to study chemotaxis and proliferation of BM-rMSC and rEPC

After evaluating the diffusive transport of bioactive molecules in our device, we performed several assays to demonstrate that the platform can be used to study the migration and proliferation of the cells of interest and evaluate the effects of calcium in their recruitment. Our results (see **Fig.10-a,b**) show that the creation of a calcium gradient in the migratory chamber is able to elicit a strong chemotactic response in BM-rMSCs in 3D, with a mean migrated distance of 124.7 ± 14.7 μm with respect to half of the microposts width (dashed line in **Fig.10-a**). This response is comparable to the one obtained using VEGF at 100 ng ml^{-1} (129.3 ± 6.7 μm), a growth factor that has been demonstrated to induce MSC mobilization via ERK- and FAK-depending

pathways [77]. In both cases, the migratory response is significantly higher than the control, in which the cells remain adhered to the wall without invading the gel. This data suggests that the transient calcium gradient, despite dissipating quickly, is enough to activate cell migration. The mean number of migrated cells is 28 ± 7 for $CaCl_2$ and 32 ± 5 for VEGF, which reinforces the idea of their chemotactic potential. The dsDNA quantification shows an almost two-fold increase in cell proliferation (see **Fig.10-c**), which probably shows that after the induction of BM-rMSC migration starts the proliferation, as a process involved in physiological or pathological conditions such as the development of vasculogenesis/angiogenesis [78]. The obtained results seem to be in good agreement with previous experiments performed in 2D using Transwells, in which extracellular calcium also elicited a strong chemotactic response on these cells [66,79].

Regarding rEPCs, our results (see **Fig.11-a,b**) show that the mean migrated distance when cells are subjected to the transient calcium gradient (60.3 ± 13.6 µm) is not significantly higher than that obtained for the control conditions (49.0 ± 10.0 µm). However, when the gradient is generated using VEGF at 100 ng/ml (which is widely known to potently stimulate endothelial cells mobilization), the migrated distance (107.7 ± 3.6 µm) is significantly higher than in the aforementioned conditions. The mean number of migrated cells is 12 ± 5 for the control condition, 10 ± 2 for the $CaCl_2$, and 37 ± 10 for the VEGF. These results agree with the proliferation data obtained by dsDNA quantification (see **Fig.11-c**), as no significant differences were observed in calcium-treated media concerning the control condition. In this case, the obtained results are in contrast with previous 2D assays, in which a significant increase in chemotaxis was reported [65,80]. We believe that the observed differences can be due to the limitations related to 2D assays, such as the lack of 3D architecture or the use of thin artificial 2D polycarbonate membranes that poorly resemble the native extracellular matrix (ECM) [81]. It is important to highlight that we did not quantify the dsDNA for cell proliferation in the case of the VEGF because it is a well-known inducer of mitosis and proliferation of these cell types [82,83]. Previously presented microfluidic systems with similar architectures have demonstrated their superior performance to Transwells to study processes like cell migration or angiogenesis [84,85,86], as they allow to better control of the biophysical and biochemical microenvironment as well as offer the possibility to incorporate perfusion and monitor cell migration in real-time cell instead of relying only on end-point measurements [87].

Notice that migration assays on 2D culture plates or glass are usually not longer than 24 h. Our previous experiments showed low viability when they were conducted for up to 3 days. A concentration of 2 % of serum was used in order to maintain cell viability for several days. We considered that some proteins and growth factors might be present in very low concentrations, but the same amount of serum was used in all conditions. We assumed that optimal conditions

are serum-free, but in our case, after optimization, a reduced serum of 2 % was needed for conducting the experiments.

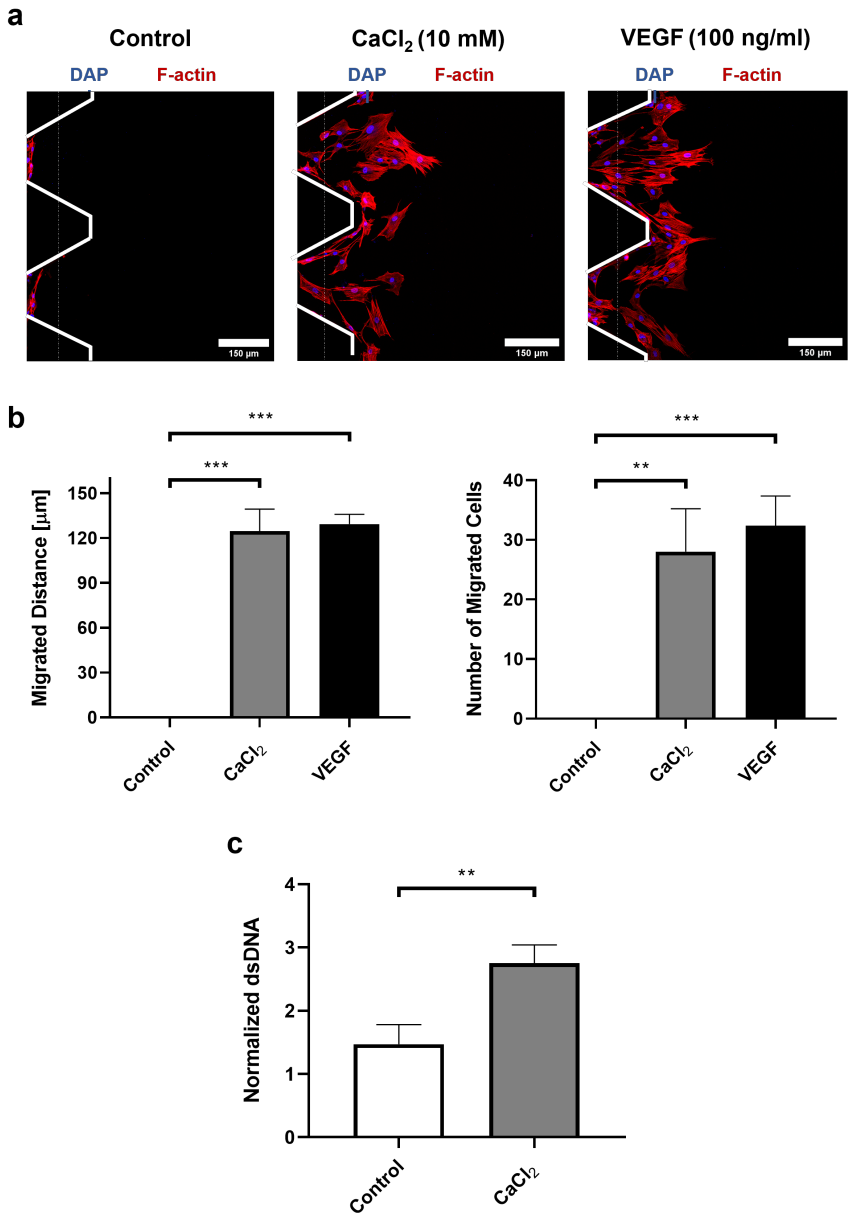

Figure 10 Evaluation of migration and proliferation of BM-rMSC in 3D microfluidic assay. (**a**) Confocal images of BM-rMSC migration in three conditions: media with no supplementation (control), media supplemented with $CaCl_2$ at 10 mM and media supplemented with VEGF at 100 ng/ml. Cells were stained for F-actin (red), and cell nuclei (blue) after a total of 3 days in culture. (**b**) Analysis of the mean migrated distance and mean number of migrated cells with respect to the half of the microposts width (dotted white line in the microscopy images). (**c**) Proliferation index from the whole BM-rMSC 3D culture in the microfluidic devices. This index was obtained as the ratio of the dsDNA content of all the cells after 3 days in culture with respect to the initial amount. Results are expressed as mean ± standard deviation ($n = 3$) with *$p < 0.05$, **$p < 0.01$ and *$p < 0.001$ (evaluated with Student's t-test).

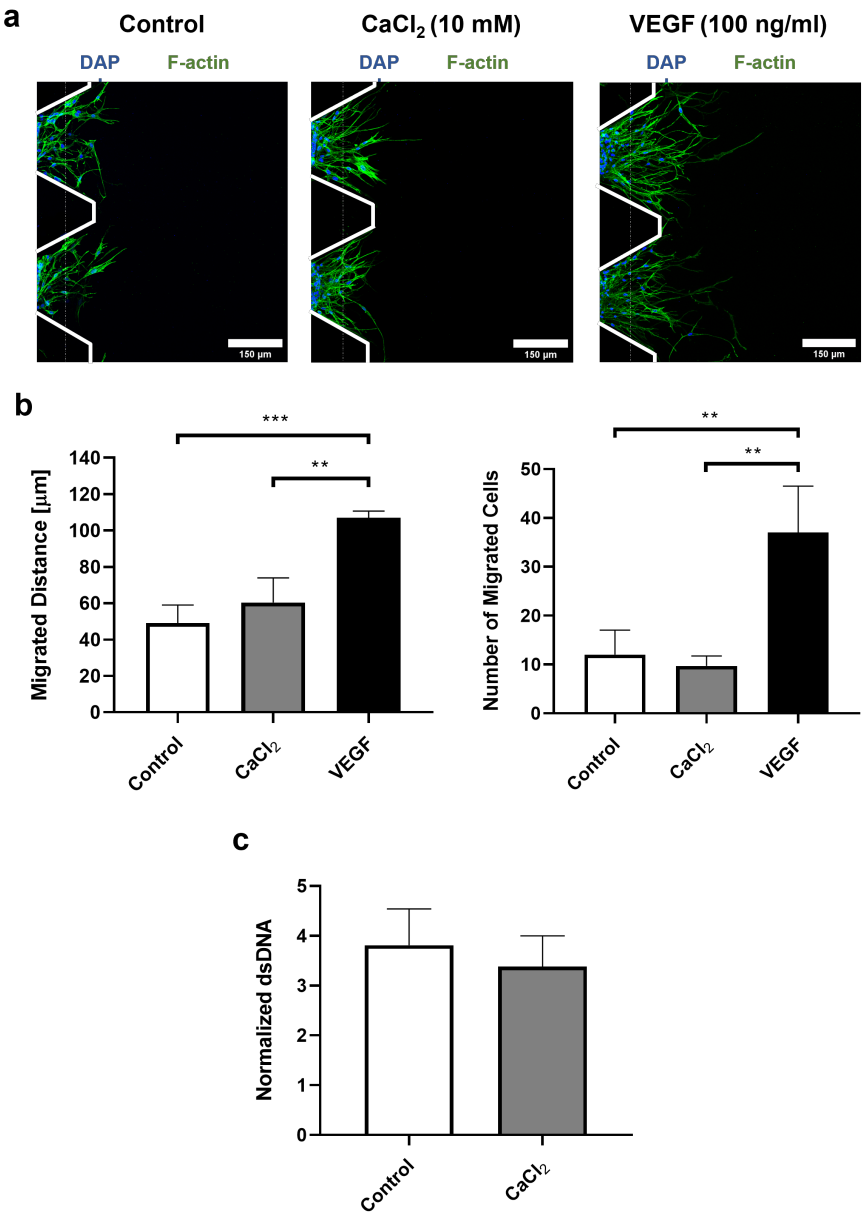

Figure 11 Evaluation of migration and proliferation of rEPC in 3D microfluidic assay. (**a**) Confocal images of rEPC migration in three conditions: media with no supplementation (control), media supplemented with $CaCl_2$ at 10 mM and media supplemented with VEGF at 100 ng/ml. Cells were stained for F-actin (green), and cell nuclei (blue) after a total of 3 days in culture. (**b**) Analysis of the mean migrated distance and mean number of migrated cells with respect to the half of the microposts width (dotted white line in the microscopy images). (**c**) Proliferation index from the whole rEPC 3D culture in the microfluidic devices. This index was obtained as the ratio of the dsDNA content of all the cells after 3 days in culture with respect to the initial amount. Results are expressed as mean ± standard deviation ($n = 3$) with $*p < 0.05$, $**p < 0.01$ and $*p < 0.001$ (evaluated with Student's t-test).

3.3.3 Calcium-releasing PLA scaffolds significantly increase rEPC recruitment compared to PLA controls in 3D microfluidic assay

Based on these previous results, we decided to assess the capacity of our platform to predict the recruitment of rEPCs using calcium-releasing biomaterials. To do so, we compared an

electrospun composite scaffold made of PLA with calcium phosphate nanoparticles with PLA controls (no calcium release). The chosen composite has been shown to induce a significant increase in vascularization compared to regular PLA in a subcutaneous mice model [88]. In those experiments, the optimal range of nanoparticle loading was established between 20-30 % (w/w), so we chose a ratio of 25 % (PLA+NP25) for our experiments.

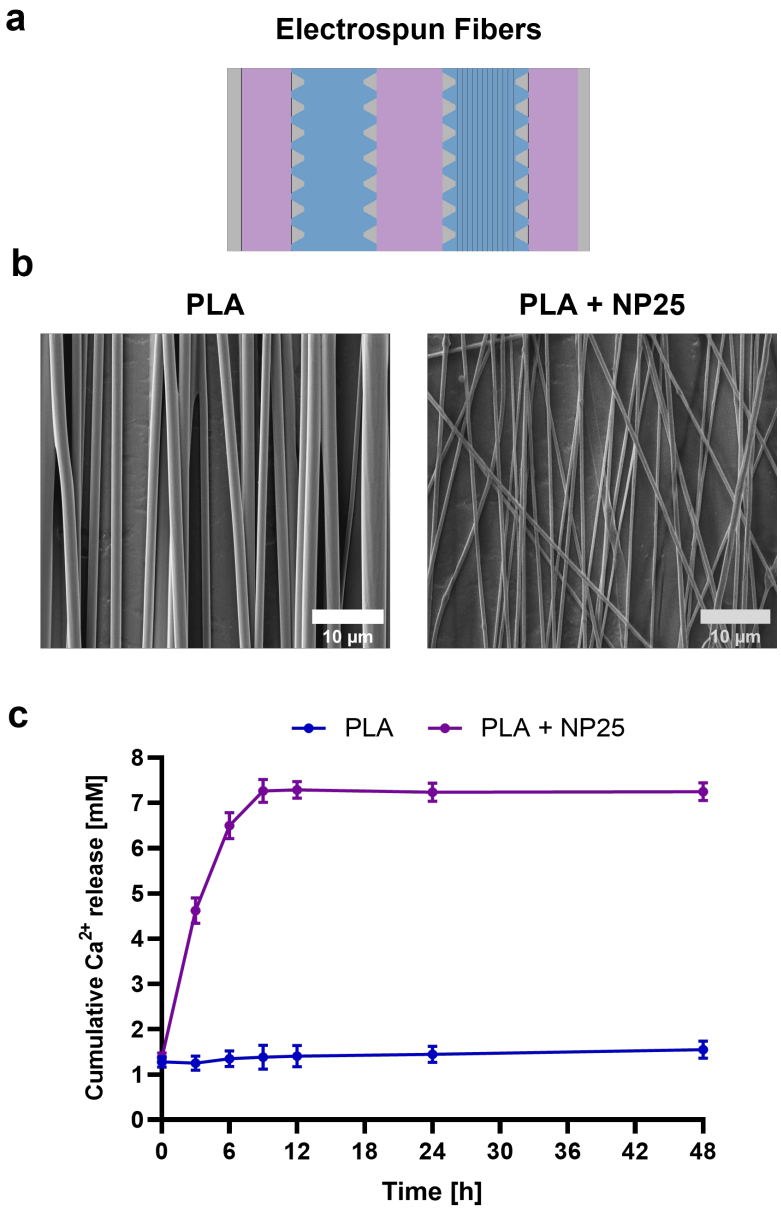

Figure 12 Biomaterial characterization. (**a**) Schematic representation of the electrospun fibers deposition in the stromal chamber of our device. (**b**) FESEM pictures showing the electrospun fibers morphology respectively. (**c**) Cumulative calcium release for the PLA fibers with CaP nanoparticles vs a regular PLA control for different timepoints (0 h, 3 h, 6 h, 9 h, 12 h, 24 h and 48 h). Results are expressed as mean ± standard deviation (n = 3).

To perform the assay, we electrospun the biomaterials in the stromal chamber (see **Fig.12-a**) and then seeded BM-rMSCs on top of the fibers to better recapitulate the bone microenvironment

(see **Fig.13-a**). In our study, we focused on paracrine signaling. Indeed, it has been shown that, in co-culture conditions where the different cell types are in direct contact, MSCs tend to wrap around the endothelial cells and differentiate into mural cells (mainly pericytes) [89,90]. We characterized the morphology of the fibers using SEM imaging (see **Fig.12-b**), which showed some differences in their arrangement, probably due to the formation of nanoparticle aggregates, which tend to induce a higher degree of disorder in the PLA+NP25 fibers. The cumulative calcium release profile in cell media (see **Fig.12-c**) was also evaluated, yielding a basal level of around 1.5 mM in the PLA controls, which corresponds to the amount of $CaCl_2$ already present in most cells culture media formulations. In the case of the PLA+NP25, the peak in the instantaneous release occurs between 3 and 4 h after immersion, while the cumulative amount of calcium reaches a maximum value of 7.25 ± 0.19 mM in around 10 h.

Notice that the calcium release of the scaffolds was measured using a custom-made device based on a PDMS block with a 10 mm punch hole in the middle in which the nanofibers were deposited. The total volume of culture media used in these experiments was 500 µl. We considered that the dimensions of the microfluidic devices couldn't have a huge influence on the release profile of the nanofibers, as the amount of total media volume used in the chips is in the same order (≈500-600 µl) and the calcium diffuses really fast in the cell culture media (order of magnitude of 10^{-9} m^2/s).

Regarding rEPCs' migration (see **Fig.13-c,d**), we observed a significantly higher migration in the case of PLA+NP25 with respect to the pure PLA controls, both in terms of the mean migrated distance (92.3 ± 5.0 µm vs 69.3 ± 11.2 µm) and the mean number of migrated cells (46 ± 13 vs 12 ± 3). As previously shown, calcium *per se* does not affect rEPCs' recruitment, so we checked for the release profile of a range of relevant pro-angiogenic and inflammatory proteins in BM-rMSC monocultures seeded on top of the two different materials. We could observe a significant increase in the release of IL-1β ($p \leq 0.01$), IL-6 ($p \leq 0.001$), IGF-2 ($p \leq 0.05$), and OPN ($p \leq 0.01$) in the case of the PLA+NP25 in our 3D microfluidic assay (see **Fig.13-b**). We chose these proteins because some studies have reported that the use of elevated extracellular calcium caused an upregulation of some angiogenic genes such as those encoding insulin-like growth factors (IGF) [91]. Pro-inflammatory cytokines such as IL-1β or IL-6 have also been associated with scaffold vascularization processes. They cause the activation of the M1 macrophages phenotype, which secrete high levels of angiogenic growth factors (such as VEGF) and metalloproteases involved in vascular remodeling [92,93]. Osteopontin, a phosphorylated acidic RGD containing glycoprotein, was also considered in our analysis, as it is a prominent constituent of the bone matrix that has been associated with angiogenesis in tumor microenvironments [94].

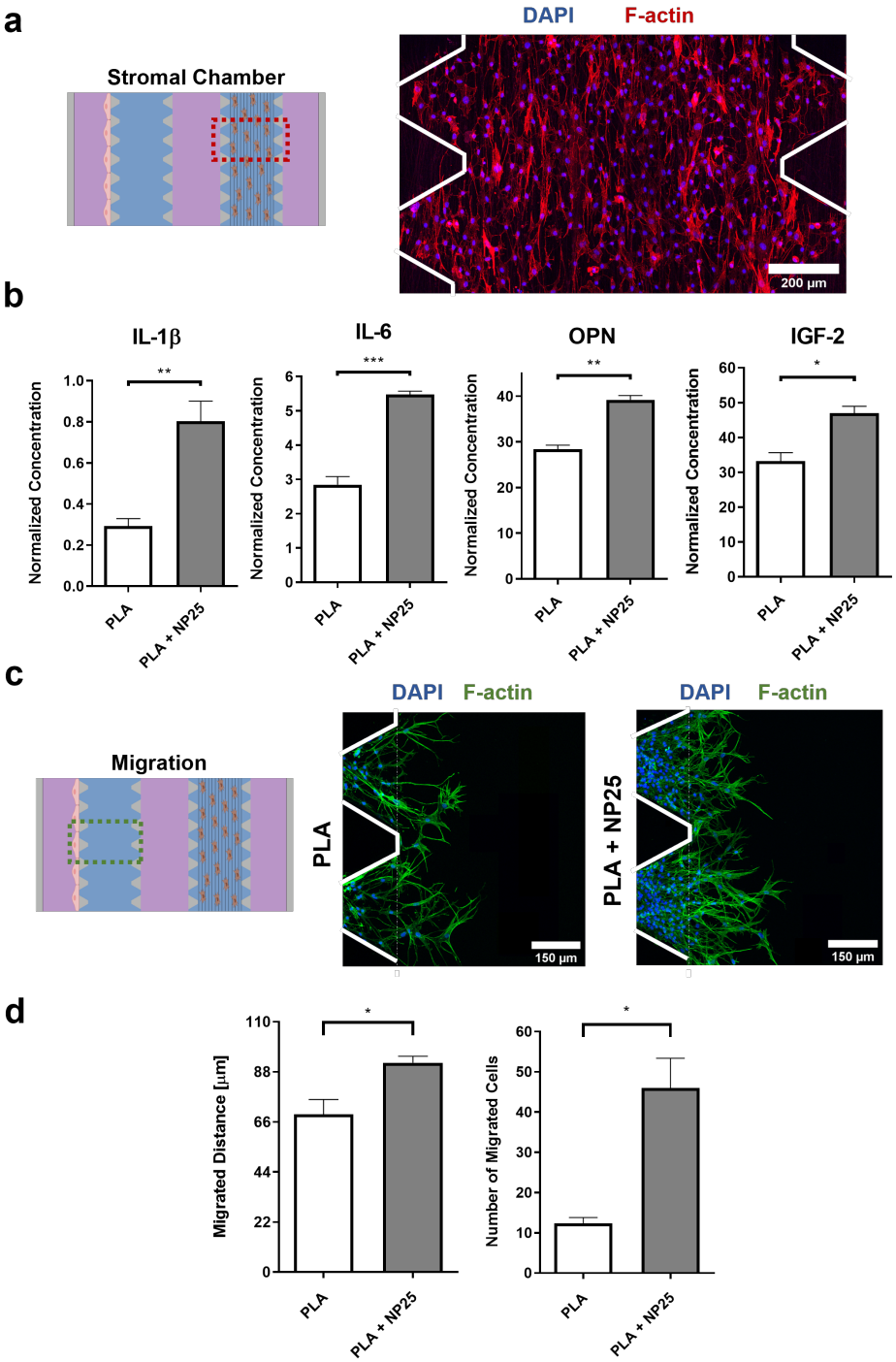

Figure 13 Evaluation of the biomaterial effects on rEPC and BM-rMSC in 3D microfluidic assay. (**a**) Schematic of the seeding conditions for the BM-rMSC in the stromal chamber on top of the electrospun fibers and confocal image of the actual seeded cells stained for F-actin (red), and cell nuclei (blue) after a total of 3 days in culture. (**b**) Total release of different pro-angiogenic and inflammatory cytokines (IL-1β, IL-6, OPN, IGF-2) in cell media by BM-rMSC for 3 days. (**c**) Schematic of the migration experiment with rEPC in co-culture conditions with the biomaterial and confocal microscopy images for PLA fiber with the CaP nanoparticles at 25 % w/w vs the regular control. Cells were stained for F-actin (green) and cell nuclei (blue) after a total of 3 days in culture. (d) Analysis of the mean migrated distance and mean number of migrated cells with respect to the half of the microposts width (dotted white line in the microscopy images). Results are presented as mean ± standard deviation (n = 3) with *p < 0.05 (Student's t-test).

To the best of our knowledge, few studies have addressed the study of biomaterials using microfluidic platforms so far. One of these works is focused on evaluating hyaluronic acid-based hydrogels by studying the resulting networks formed by the self-assembling of human-induced pluripotent stem cell-derived endothelial cells (hiPSC-ECs) [95]. The main drawback of this platform is that its applicability is limited to the evaluation of vasculogenesis in hydrogel-based materials, as performing migration studies or incorporating rigid scaffolds is not possible in the proposed device. Another recent study has also put forward a microfluidic platform to evaluate expanded polytetrafluoroethylene (ePTFE) membranes by assessing the capacity of a preformed vascular network composed of human umbilical vein endothelial cells (HUVEC) and human lung fibroblasts (hLF) to colonize it [96]. However, although being an excellent proof of concept showing how microfluidics can be used to test biomaterials, we consider that there are some drawbacks that limit its applicability, especially for bone tissue engineering applications. For instance, it relies on a complex fabrication process requiring specialized laser cutting equipment and the creation of U-shaped pieces to fit the membrane in the device, which can lead to problems of gap formation between the substrate and the membrane. Moreover, the direct growth of the cells in the material makes it difficult to discern the different variables at play (bioactive ion release, porosity, etc.). We believe that our platform offers a low-cost and more robust solution for the study of the experimental variables independently, something that is not achievable with the aforementioned microfluidic assays or other commonly used *ex vivo* or *in vivo* assays (such as the CAM assay), as it allows for the direct incorporation of the biomaterial scaffold (such as electrospun ones) without direct cell contact to study the process of cell migration towards the material.

3.3.4 Calcium-mediated osteopontin secretion by BM-rMSC is one of the main signaling cues determining rEPC recruitment in microfluidic 3D assay

Based on the previously presented results, we decided to further study the role of OPN in the recruitment of rEPCs, as its role in this process is widely unknown. To test the hypothesis of OPN-mediated EPCs recruitment, we performed a migration assay in co-culture conditions treating the calcium-conditioned media with an OPN inhibitor (anti-OPN antibody at 10 µg/ml). We validated the use of this strategy by checking that osteopontin levels in cell culture media were significantly increased when the cells were stimulated with high levels of extracellular calcium salt for two days but drastically reduced when treated with the inhibitor (see **Fig.14-c**). Regarding rEPCs migratory activity (see **Fig.14-a-b**), the travelled migrated distance in calcium-treated media (104.3 ± 12.7 µm) was significantly higher than in the control condition (47.3 ± 5.0 µm) but drastically reduced when the anti-OPN antibody was added to the media (72.3 ± 12.1 µm). A decrease in the number of migrated cells was also observed when using the OPN inhibitor,

from 58 ± 5 to 35 ± 4, being this value still higher than the one obtained in the control condition (23 ± 4 cells).

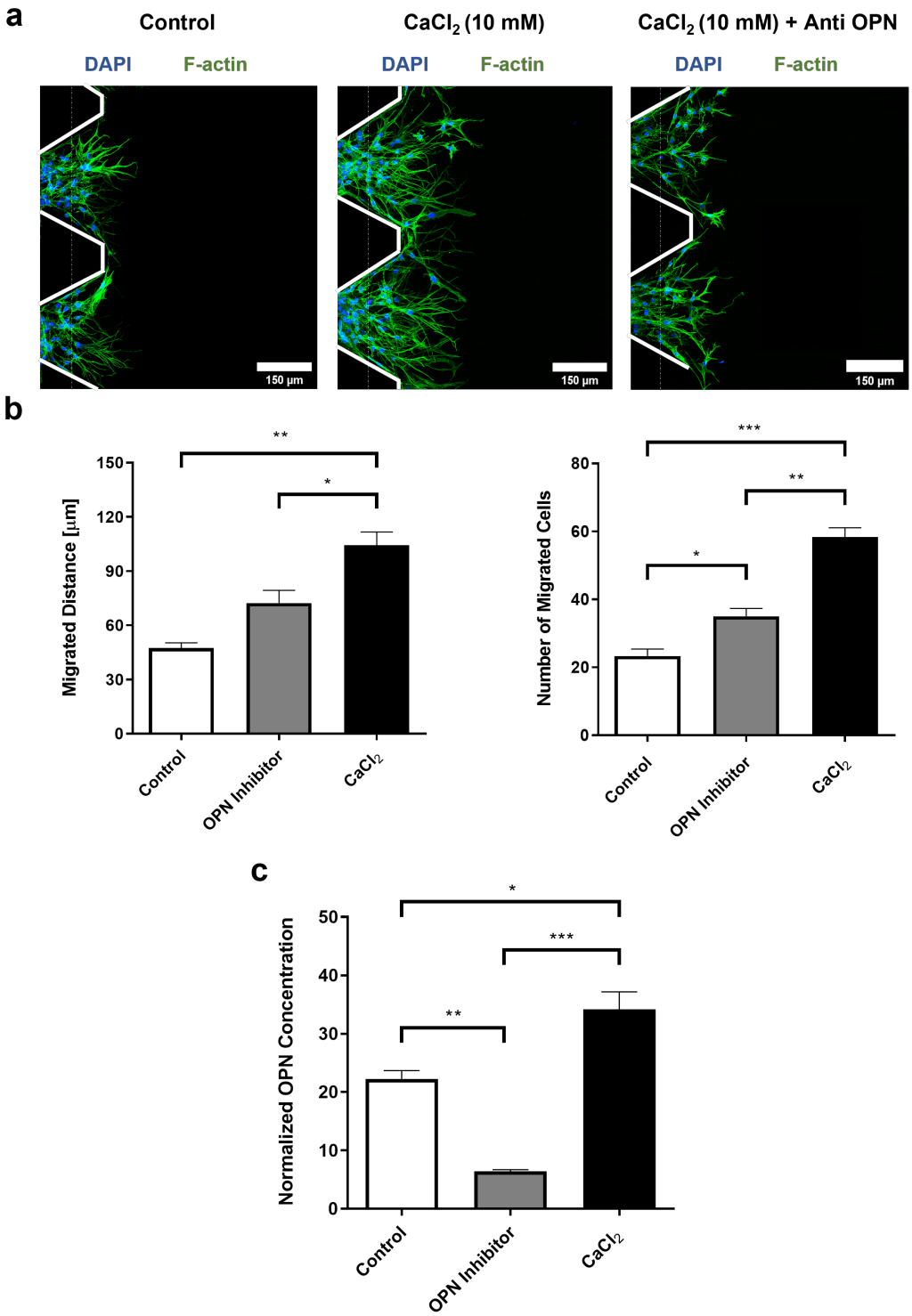

Figure 14 Evaluation of the osteopontin effect on rEPC migration in 3D microfluidic assay. (**a**) Confocal images of rEPC migration in three conditions: media with no supplementation (control), media supplemented with $CaCl_2$ at 10 mM and media supplemented with $CaCl_2$ at 10 mM with an osteopontin inhibitor. Cells were stained for F-actin (green), and cell nuclei (blue) after a total of 3 days in culture. (**b**) Analysis of the mean migrated distance and mean number of

migrated cells with respect to the half of the microposts width (dotted white line in the microscopy images). (**c**) Total amount of osteopontin released by BM-rMSC 3D-cultured in the microfluidic devices for 3 days. Results are expressed as mean ± standard deviation ($n = 3$) with $*p < 0.05$, $**p < 0.01$ and $*p < 0.001$ (evaluated with Student's t-test).

These results are in line with several studies showing that the use of an anti-OPN antibody resulted in significant inhibition of angiogenesis in two different *in vivo* models (chick chorioallantoic membrane and corneal pocket assays), slowing down tumor progression [94,97]. Overall, our results suggest that calcium is not acting as a primary signal in rEPCs recruitment, but rather as a mediator in the secretion of chemotactic proteins by rBM-rMSCs. Among the secreted chemotactic proteins, we found that osteopontin may play an important role in the migration events of rEPCs. This supports the idea that the crosstalk between rEPCs and BM-rMSCs is essential for the modulation of vascularization in bone healing [98,99] and that vasculogenesis and osteogenesis are closely linked [100]. Further studies should be performed to shed light on whether other key signals are also involved in the behavior of endothelial cells in angiogenic processes through cell crosstalking.

3.4 Conclusions

In this work, a novel 3D microfluidic assay to study the effects of calcium release on the recruitment of rEPCs is presented. We validated the functionality of the platform by evaluating the migration and proliferation in 3D of the two main cell types involved in this process (BM-rMSCs and rEPCs, both derived from rat bone marrow), and the possibility to generate gradients of bioactive molecules using an experimentally-validated finite element model. We also confirmed the possibility to incorporate and study calcium-releasing scaffolds in the platform, showing a significant increase in rEPCs' recruitment when using a pro-angiogenic electrospun scaffold made of PLA with calcium phosphate nanoparticles with respect to regular PLA controls. We also evidenced the utility of the assay to evaluate signaling cues involved in rEPCs' recruitment by studying the role of osteopontin in this process. The obtained results point to the central role of this protein in the calcium-mediated recruitment of rEPCs. Overall, we believe that the presented platform is an effective tool to evaluate and better understand the capacity of implant material candidates to recruit endogenous endothelial progenitors, a key step in the scaffold vascularization process.

3.5 References

[1] Novosel E C, Kleinhans C and Kluger P J 2011 Vascularization is the key challenge in tissue engineering *Adv. Drug Deliv. Rev.* **63** 300–11.

[2] Folkman J 2006 Angiogenesis *Annu. Rev. Med.* **57** 1–18.

[3] Haase K and Kamm R D 2017 Advances in on-chip vascularization *Regen. Med.* **12** 285–

302.

[4] Herbert S P and Stainier D Y R 2011 Molecular control of endothelial cell behaviour during blood vessel morphogenesis *Nat. Rev. Mol. Cell Biol.* **12** 551–64.

[5] Tonini T, Rossi F and Claudio P P 2003 Molecular basis of angiogenesis and cancer *Oncogene* **22** 6549–56.

[6] Ferrara N, Gerber H P and LeCouter J 2003 The biology of VEGF and its receptors *Nat. Med.* **9** 669–76.

[7] Krock B L, Skuli N and Simon M C 2011 Hypoxia-induced angiogenesis: good and evil *Genes and Cancer* **2** 1117–33.

[8] Staton C A, Stribbling S M, Tazzyman S, Hughes R, Brown N J and Lewis C E 2004 Current methods for assaying angiogenesis in vitro and in vivo *Int. J. Exp. Pathol.* **85** 233–48.

[9] Eccles S A, Court W, Patterson L and Sanderson S 2009 In vitro assays for endothelial cell functions related to angiogenesis: proliferation, motility, tubular differentiation, and proteolysis. *Methods Mol. Biol.* **467** 159–81.

[10] Lamalice L, Le Boeuf F and Huot J 2007 Endothelial cell migration during angiogenesis *Circ. Res.* **100** 782–94.

[11] Rodriguez L G, Wu X and Guan J L 2005 Wound-healing assay *Methods Mol. Biol.* **294** 23–9.

[12] Jonkman J E, Cathcart J A, Xu F, Bartolini M E, Amon J E, Stevens K M and Colarusso P 2014 An introduction to the wound healing assay using live-cell microscopy *Cell Adhes. Migr.* **8** 440–51.

[13] Lawley T J and Kubota Y 1989 Induction of morphologic differentiation of endothelial cells in culture *J. Invest. Dermatol.* **93** 59–61.

[14] Kanzawa S, Endo H and Shioya N 1993 Improved in vitro angiogenesis model by collagen density reduction and the use of type III collagen *Ann. Plast. Surg.* **30** 244–51.

[15] Gagnon E, Cattaruzzi P, Griffith M, Muzakare L, LeFlaol K, Faure R, Beliveau R, Hussain S N, Koutsilieris M and Doillon C J 2002 Human vascular endothelial cells with extended life spans: in vitro cell response, protein expression, and angiogenesis *Angiogenesis* **5** 21–33.

[16] Bishop E T, Bell G T, Bloor S, Broom I J, Hendry N F K and Wheatley D N 1999 An in vitro model of angiogenesis: basic features *Angiogenesis* **3** 335–44.

[17] Donovan D, Brown N J, Bishop E T and Lewis C E 2001 Comparison of three in vitro human “angiogenesis” assays with capillaries formed in vivo *Angiogenesis* **4** 113–21.

[18] Auerbach R, Auerbach W and Polakowski I 1991 Assays for angiogenesis: a review *Pharmacol. Ther.* **51** 1–11.

[19] Nicosia R F, Lin Y J, Hazelton D and Qian X H 1997 Endogenous regulation of angiogenesis in the rat aorta model: role of vascular endothelial growth factor *Am. J. Pathol.* **151** 1379–86.

[20] Auerbach R, Akhtar N, Lewis R L and Shinners B L 2000 Angiogenesis assays: problems and pitfalls *Cancer Metastasis Rev.* **19** 167–72.

[21] Jackson C J and Nguyen M 1997 Human microvascular endothelial cells differ from macrovascular endothelial cells in their expression of matrix metalloproteinases *Int. J. Biochem. Cell Biol.* **29** 1167–77.

[22] Auerbach R, Lewis R, Shinners B, Kubai L and Akhtar N 2003 Angiogenesis assays: a critical overview *Clin. Chem.* **49** 32–40.

[23] Dellian M, Witwer B P, Salehi H A, Yuan F and Jain R K 1996 Quantitation and physiological characterization of angiogenic vessels in mice: effect of basic fibroblast growth factor, vascular endothelial growth factor/vascular permeability factor, and host microenvironment *Am. J. Pathol.* **149** 59–71.

[24] Jain R K, Schlenger K, Hockel M and Yuan F 1997 Quantitative angiogenesis assays: Progress and problems *Nat. Med.* **3** 1203–8.

[25] Downs E C, Robertson N E, Riss T L and Plunkett M L 1992 Calcium alginate beads as a slow-release system for delivering angiogenic molecules in vivo and in vitro *J. Cell. Physiol.* **152** 422–9.

[26] Nguyen M, Shing Y and Folkman J 1994 Quantitation of angiogenesis and antiangiogenesis in the chick embryo chorioallantoic membrane *Microvasc. Res.* **47** 31–40.

[27] Gimbrone M A, Cotran R S, Leapman S B and Folkman J 1974 Tumor growth and neovascularization: an experimental model using the rabbit cornea *J. Natl. Cancer Inst.* **52** 413–27.

[28] Muthukkaruppan V and Auerbach R 1979 Angiogenesis in the mouse cornea *Science* **205** 1416–8.

[29] Chrobak K M, Potter D R and Tien J 2006 Formation of perfused, functional microvascular

tubes in vitro *Microvasc. Res.* **71** 185–96.

[30] Sadr N, Zhu M, Osaki T, Kakegawa T, Yang Y, Moretti M, Fukuda J and Khademhosseini A 2011 SAM-based cell transfer to photopatterned hydrogels for microengineering vascular-like structures *Biomaterials* **32** 7479–90.

[31] Yoshida H, Matsusaki M and Akashi M 2013 Multilayered blood capillary analogs in biodegradable hydrogels for in vitro drug permeability assays *Adv. Funct. Mater.* **23** 1736–42.

[32] Miller J S, Stevens K R, Yang M T, Baker B M, Nguyen D H T, Cohen D M, Toro E, Chen A A, Galie P A, Yu X, Chaturvedi R, Bhatia S N and Chen C S 2012 Rapid casting of patterned vascular networks for perfusable engineered three-dimensional tissues *Nat. Mater.* **11** 768–74.

[33] Heintz K A, Bregenzer M E, Mantle J L, Lee K H, West J L and Slater J H 2016 Fabrication of 3D biomimetic microfluidic networks in hydrogels *Adv. Healthc. Mater.* **5** 2153–60.

[34] Golden A P and Tien J 2007 Fabrication of microfluidic hydrogels using molded gelatin as a sacrificial element *Lab Chip* **7** 720–725.

[35] Wang X Y, Jin Z H, Gan B W, Xie M and Huang W H 2014 Engineering interconnected 3D vascular networks in hydrogels using molded sodium alginate lattice as the sacrificial template *Lab Chip* **14** 2709–16.

[36] Tsang V L, Chen A A, Cho L M, Jadin K D, Sah R L, DeLong S, West J L and Bhatia S N 2007 Fabrication of 3D hepatic tissues by additive photopatterning of cellular hydrogels *FASEB J.* **21** 790–801.

[37] Brandenberg N and Lutolf M P 2016 In situ patterning of microfluidic networks in 3D cell-laden hydrogels *Adv. Mater.* **28** 7450–56.

[38] Nakatsu M N, Sainson R C A, Aoto J N, Taylor K L, Aitkenhead M, Perez-del-Pulgar S, Carpenter P M and Hughes C C W 2003 Angiogenic sprouting and capillary lumen formation modeled by human umbilical vein endothelial cells (HUVEC) in fibrin gels: the role of fibroblasts and angiopoietin-1 *Microvasc. Res.* **66** 102–12.

[39] Newman A C, Nakatsu M N, Chou W, Gershon P D and Hughes C C W 2011 The requirement for fibroblasts in angiogenesis: Fibroblast-derived matrix proteins are essential for endothelial cell lumen formation *Mol. Biol. Cell* **22** 3791–800.

[40] Vickerman V, Blundo J, Chung S and Kamm R 2008 Design, fabrication and implementation of a novel multi-parameter control microfluidic platform for three-dimensional cell culture and real-time imaging *Lab Chip* **8** 1468–77.

[41] Chung S, Sudo R, MacK P J, Wan C R, Vickerman V and Kamm R D 2009 Cell migration into scaffolds under co-culture conditions in a microfluidic platform *Lab Chip* **9** 269–75.

[42] Song J W and Munn L L 2011 Fluid forces control endothelial sprouting *Proc. Natl. Acad. Sci. U. S. A.* **108** 15342–47.

[43] Farahat W A, Wood L B, Zervantonakis I K, Schor A, Ong S, Neal D, Kamm R D and Asada H H 2012 Ensemble analysis of angiogenic growth in three-dimensional microfluidic cell cultures *PLoS One* **7** 333-347.

[44] Whisler J A, Chen M B and Kamm R D 2014 Control of perfusable microvascular network morphology using a multiculture microfluidic system *Tissue Eng. - Part C Methods* **20** 543–52.

[45] Moya M L, Hsu Y H, Lee A P, Christopher C W H and George S C 2013 In vitro perfused human capillary networks *Tissue Eng. - Part C Methods* **19** 730–737.

[46] Chen M B, Whisler J A, Jeon J S and Kamm R D 2013 Mechanisms of tumor cell extravasation in an in vitro microvascular network platform *Integr. Biol.* **5** 1262–71.

[47] Bischel L L, Young E W K, Mader B R and Beebe D J 2013 Tubeless microfluidic angiogenesis assay with three-dimensional endothelial-lined microvessels *Biomaterials* **34** 1471–77.

[48] Abbott N J, Ronnback L and Hansson E 2006 Astrocyte-endothelial interactions at the blood-brain barrier *Nat. Rev. Neurosci.* **7** 41–53.

[49] Abbott N J 2005 Dynamics of CNS barriers: evolution, differentiation, and modulation *Cell. Mol. Neurobiol.* **25** 5–23.

[50] Zlokovic B V. 2008 The blood-brain barrier in health and chronic neurodegenerative disorders *Neuron* **57** 178–201.

[51] Adriani G, Ma D, Pavesi A, Kamm R D and Goh E L K 2017 A 3D neurovascular microfluidic model consisting of neurons, astrocytes and cerebral endothelial cells as a blood-brain barrier *Lab Chip* **17** 448–59.

[52] Adriani G, Ma D, Pavesi A, Kamm R D and Goh E L K 2017 A 3D neurovascular microfluidic model consisting of neurons, astrocytes and cerebral endothelial cells as a blood-brain barrier *Lab Chip* **17** 448–59.

[53] Mori N, Morimoto Y and Takeuchi S 2017 Skin integrated with perfusable vascular channels on a chip *Biomaterials* **116** 48–56.

[54] Liu Y, Li H, Yan S, Wei J and Li X 2014 Hepatocyte cocultures with endothelial cells and

fibroblasts on micropatterned fibrous mats to promote liver-specific functions and capillary formation capabilities *Biomacromolecules* **15** 1044–54.

[55] Jusoh N, Oh S, Kim S, Kim J and Jeon N L 2015 Microfluidic vascularized bone tissue model with hydroxyapatite-incorporated extracellular matrix *Lab Chip* **15** 3984–8.

[56] Lee S, Ko J, Park D, Lee S R, Chung M, Lee Y and Jeon N L 2018 Microfluidic-based vascularized microphysiological systems *Lab Chip* **18** 2686–709.

[57] Hsu Y H, Moya M L, Hughes C C W, George S C and Lee A P 2013 A microfluidic platform for generating large-scale nearly identical human microphysiological vascularized tissue arrays *Lab Chip* **13** 2990–8.

[58] Rosenfeld D, Landau S, Shandalov Y, Raindel N, Freiman A, Shor E, Blinder Y, Vandenburgh H H, Mooney D J and Levenberg S 2016 Morphogenesis of 3D vascular networks is regulated by tensile forces *Proc. Natl. Acad. Sci. U. S. A.* **113** 3215–20.

[59] Kim S, Lee H, Chung M and Jeon N L 2013 Engineering of functional, perfusable 3D microvascular networks on a chip *Lab Chip* **13** 1489–500.

[60] Huxley V H, Curry F E and Adamson R H 1987 Quantitative fluorescence microscopy on single capillaries: α-lactalbumin transport *Am. J. Physiol. - Hear. Circ. Physiol.* **252** 188-197.

[61] Tarbell J M 2010 Shear stress and the endothelial transport barrier *Cardiovasc. Res.* **87** 320–30.

[62] Curry F R E and Adamson R H 2010 Vascular permeability modulation at the cell, microvessel, or whole organ level: towards closing gaps in our knowledge *Cardiovasc. Res.* **87** 218–29.

[63] Natividad-Diaz S L, Browne S, Jha A K, Ma Z, Hossainy S, Kurokawa Y K, George S C and Healy K E 2019 A combined hiPSC-derived endothelial cell and in vitro microfluidic platform for assessing biomaterial-based angiogenesis *Biomaterials* **194** 73–83

[64] Bai J, Haase K, Roberts J, Hoffmann J, Nguyen H T, Wan Z, Zhang S, Sarker B, Friedman N, Ristic-Lehmann C and Kamm R D 2021 A novel 3D vascular assay for evaluating angiogenesis across porous membranes *Biomaterials* **268** 120–35

[65] Aguirre A, González A, Planell J A, Engel E 2010 Extracellular calcium modulates in vitro bone marrow-derived Flk-1^{+} CD34^{+} progenitor cell chemotaxis and differentiation through a calcium-sensing receptor *Biochem. Biophys. Res. Commun.* **393** 156-61.

[66] González A, Planell J A, Engel E 2014 Extracellular calcium and CaSR drive osteoinduction

in mesenchymal stromal cells *Acta Biomater.* **10** 2824–33.

[67] Khakoo A Y, Finkel T 2005 Endothelial progenitor cells *Annu. Rev. Med.* **56** 79–101.

[68] Favoni R E, De Cupis A 2000 The role of polypeptide growth factors in human carcinomas: New targets for a novel pharmacological approach *Pharmacol. Rev.* **52** 179–206.

[69] Braga J, Desterro J M, Carmo-Fonseca M 2004 Intracellular macromolecular mobility measured by fluorescence recovery after photobleaching with confocal laser scanning microscopes *Mol. Biol. Cell.* **15** 4749–60.

[70] Sanzana ES, Navarro M, Macule F, Suso S, Planell J A, Ginebra M P 2008 Of the in vivo behavior of calcium phosphate cements and glasses as bone substitutes *Acta Biomater.* **4** 1924–33.

[71] Schindelin J, Arganda-Carreras I, Frise E, Kaynig V, Longair M, Pietzsch T, Preibisch S, Rueden C, Saalfeld S, Schmid B, Tinevez J Y, White D J, Hartenstein V, Eliceiri K, Tomancak P, Cardona A 2012 Fiji: An open-source platform for biological-image analysis *Nat. Methods.* **9** 676–682.

[72] Bolte S, Cordelieres F P 2006 A guided tour into subcellular colocalization analysis in light microscopy *J. Microsc.* **224** 213–232.

[73] Shin Y, Jeon J S, Han S, Jung G S, Shin S, Lee S H, Sudo R, Kamm R D, Chung S 2011 In vitro 3D collective sprouting angiogenesis under orchestrated ANG-1 and VEGF gradients *Lab Chip* **11** 2175–81.

[74] Helm C L, Fleury M E, Zisch A H, Boschetti F, Swartz M A 2005 Synergy between interstitial flow and VEGF directs capillary morphogenesis in vitro through a gradient amplification mechanism *Proc. Natl. Acad. Sci.* **102** 15779–84.

[75] Schuszter G, Geher-Herczegh T, Szucs A, Toth A, Horvath D 2017 Determination of the diffusion coefficient of hydrogen ion in hydrogels *Phys. Chem. Chem. Phys.* **19** 12136–43.

[76] Lim S H, Kim C, Aref A R, Kamm R D, Raghunath M 2013 Complementary effects of ciclopirox olamine, a prolyl hydroxylase inhibitor and sphingosine 1-phosphate on fibroblasts and endothelial cells in driving capillary sprouting *Integr. Biol.* **5** 1474–84.

[77] Ishii M, Takahashi M, Murakami J, Yanagisawa T, Nishimura M 2019 Vascular endothelial growth factor-C promotes human mesenchymal stem cell migration via an ERK-and FAK-dependent mechanism *Mol. Cell. Biochem.* **455** 185–193.

[78] De Donatis A, Ranaldi F, Cirri P 2010 Reciprocal control of cell proliferation and migration *Cell Commun. Signal.* **8** 1–4.

[79] Lee M N, Hwang H S, Oh S H, Roshanzadeh A, Kim J W, Song J H, Kim E S, Koh J T 2018 Elevated extracellular calcium ions promote proliferation and migration of mesenchymal stem cells via increasing osteopontin expression *Exp. Mol. Med.* **50** 1-16.

[80] Aguirre A, González A, Navarro M, Castaño O, Planell J A, Engel E 2012 Control of microenvironmental cues with a smart biomaterial composite promotes endothelial progenitor cell angiogenesis *Eur. Cells Mater.* **24** 90–106.

[81] Esch E W, Bahinski A, Huh D 2015 Organs-on-chips at the frontiers of drug discovery *Nat. Rev. Drug Discov.* **14** 248–260.

[82] Olsson A K, Dimberg A, Kreuger J, Claesson-Welsh L 2006 VEGF receptor signalling - in control of vascular function *Nat. Rev. Mol. Cell Biol.* **7** 359–371.

[83] Yun S P, Lee M Y, Ryu J M, Song C H, Han H J 2009 Role of HIF-1alpha and VEGF in human mesenchymal stem cell proliferation by 17beta-estradiol: involvement of PKC, PI3K/Akt, and MAPKs *Am. J. Physiol. Cell Physiol.* **296** 317-326.

[84] Kim S, Lee H, Chung M, Jeon N L 2013 Engineering of functional, perfusable 3D microvascular networks on a chip *Lab Chip* **13** 1489–1500.

[85] Shin Y, Han S, Jeon J S, Yamamoto K, Zervantonakis I K, Sudo R, Kamm R D, Chung S 2012 Microfluidic assay for simultaneous culture of multiple cell types on surfaces or within hydrogels *Nat. Protoc.* **7** 1247–1259.

[86] Tan S Y, Leung Z, Wu A R 2020 Recreating physiological environments in vitro: Design rules for microfluidic-based vascularized tissue constructs *Small* **16** 55-72.

[87] Zhang B, Korolj A, Lai B F, Radisic M 2018 Advances in organ-on-a-chip engineering *Nat. Rev. Mater.* **3** 257–278.

[88] Oliveira H, Catros S, Boiziau C, Siadous R, Marti-Munoz J, Bareille R, Rey S, Castano O, Planell J, Amedee J, Engel E 2016 The proangiogenic potential of a novel calcium releasing biomaterial: Impact on cell recruitment. *Acta Biomater.* **29** 435–45.

[89] Joensuu K, Uusitalo-Kylmala L, Hentunen T A, Heino T J 2018 Angiogenic potential of human mesenchymal stromal cell and circulating mononuclear cell cocultures is reflected in the expression profiles of proangiogenic factors leading to endothelial cell and pericyte differentiation *J. Tissue Eng. Regen. Med.* **12** 775–783.

[90] Lozito T P, Kuo C K, Taboas J M, Tuan R S 2009 Human mesenchymal stem cells express vascular cell phenotypes upon interaction with endothelial cell matrix *J. Cell. Biochem.* **107** 714–722.

[91] Maeng Y S, Choi H J, Kwon J Y, Park Y W, Choi K S, Min J K, Kim Y H, Suh P G, Kang K S, Won M H, Kim Y M, Kwon Y G 2009 Endothelial progenitor cell homing: Prominent role of the IGF2-IGF2R-PLC 22 axis *Blood* **113** 233–243.

[92] Martinez F O, Gordon S, Locati M and Mantovani A 2006 Transcriptional profiling of the human monocyte-to-macrophage differentiation and polarization: New molecules and patterns of gene expression *J Immunol* **177** 7303-11.

[93] Spiller K L, Anfang R R, Spiller K J, Ng J, Nakazawa K R, Daulton J W and Vunjak-Novakovic G 2014 The role of macrophage phenotype in vascularization of tissue engineering scaffolds *Biomaterials* **35** 4477–88.

[94] Zhao H, Chen Q, Alam A, Cui J, Suen K C, Soo A P, Eguchi S, Gu J, Ma D 2018 The role of osteopontin in the progression of solid organ tumour *Cell Death Dis.* **9** 356-371.

[95] Natividad-Diaz S L, Browne S, Jha A K, Ma Z, Hossainy S, Kurokawa Y K, George S C, Healy K E 2019 A combined hiPSC-derived endothelial cell and in vitro microfluidic platform for assessing biomaterial-based angiogenesis *Biomaterials* **194** 73–83.

[96] Bai J, Haase K, Roberts J J, Hoffmann J, Nguyen H T, Wan Z, Zhang S, Sarker B, Friedman N, Ristic-Lehmann C, Kamm R D 2021 A novel 3D vascular assay for evaluating angiogenesis across porous membranes *Biomaterials* **268** 592-607.

[97] Dai J, Peng L, Fan K, Wang H, Wei R, Ji G, Cai J, Lu B, Li B, Zhang D, Kang Y, Tan M, Qian W, Guo Y 2009 Osteopontin induces angiogenesis through activation of PI3K/AKT and ERK1/2 in endothelial cells *Oncogene* **28** 3412–3422.

[98] Aguirre A, Planell J A, Engel E 2010 Dynamics of bone marrow-derived endothelial progenitor cell/mesenchymal stem cell interaction in co-culture and its implications in angiogenesis *Biochem. Biophys. Res. Commun.* **400** 284–291.

[99] Rouwkema J, Westerweel P E, De Boer J, Verhaar M C, Van Blitterswijk C A 2009 The use of endothelial progenitor cells for prevascularized bone tissue engineering *Tissue Eng. - Part A* **15** 2015–2027.

[100] Hankenson K D, Dishowitz M, Gray C, Schenker M 2011 Angiogenesis in bone regeneration *Injury* **42** 556–561.

4

A Microphysiological System Combining Electrospun Fibers and Electrical Stimulation for the Maturation of Highly Anisotropic Cardiac Tissue

The creation of cardiac tissue models for preclinical testing is still a non-solved problem in drug discovery, due to the limitations related to the *in vitro* replication of cardiac tissue complexity. Among these limitations, the difficulty of mimicking the functional properties of the myocardium due to the immaturity of the used cells hampers the obtention of reliable results that could be translated into human patients. In this chapter, start by introducing the current state of the art in microphysiological models of cardiac tissue to then describe our contribution to the field, based on a microfluidic platform that aims to provide a range of signaling cues to immature cardiac cells to drive them towards an adult phenotype. The device combines topographical electrospun nanofibers with electrical stimulation in a microfabricated system. We validated our platform using a co-culture of neonatal mouse cardiomyocytes and cardiac fibroblasts, showing that it allows us to control the degree of anisotropy of the cardiac tissue inside the microdevice in a cost-effective way. Moreover, a 3D computational model of the electrical field was created and validated to demonstrate that our platform can closely match the distribution obtained with the gold standard (planar electrode technology) using inexpensive rod-shaped biocompatible stainless-steel electrodes. The functionality of the electrical stimulation was shown to induce a higher expression of the tight junction protein Cx-43, as well as the upregulation of several key genes involved in conductive and structural cardiac properties. These results validate our platform as a powerful tool for the tissue engineering community due to its low cost, high imaging compatibility, versatility, and high-throughput configuration capabilities.

4.1 Introduction to microphysiological models of cardiac tissue

The development of microphysiological models has led to unprecedented advancements in the understanding of cardiac physiology [1]. Traditional *in vitro* models are unable to replicate the complex architecture of the heart muscle, in which tissue orientation and electromechanical stimuli play a critical role [2]. Animal models remain the golden standard for drug discovery and disease modelling, although it is widely recognized that they cannot accurately represent human physiology due to the differences in genetics and etiology (ion channel expression, particular mutations leading to cardiovascular disease, etc) [3]. The development of MPS and stem cell technology is opening new possibilities to create biomimetic human cardiac tissues, in which the different cues involved in tissue organization and maturation can be readily modelled [4].

First developments in the field focused on improving the physiological relevance of **2D cardiac models.** Traditional cell culturing in flasks or Petri dishes results in disorganized sarcomeric structure, low electrical action potentials and fetal-like phenotype in terms of metabolism and mitochondrial density, which leads to poorly-predictive drug responses [5]. Early MPS tried to address these by incorporating aligned topological features to mimic the high anisotropy of cardiac tissue. Some of the proposed techniques include microcontact printing [6,7] hydrogel patterning with microfluidic channels [8,9], microabrasion [10] or hot embossing [11]. Patterning was sometimes combined with electrical stimulation to drive CM maturation [10,11]. Most early studies have relied on the use of murine neonatal CMs, but the discovery of hiPSC has opened up the possibility to model actual human tissues [2]. Recent studies have shown improved sarcomeric organization, differentiation efficiency and physiological responses to well-characterized drugs such as isoproterenol in two-dimensional MPS [12,13]. The main advantages of the 2D approach are related to its high-throughput capabilities for drug screening purposes [4]. However, these constructs display a lower degree of cell organization compared to 3D tissues, which results in a less mature phenotype [14].

Platforms based on **3D cardiac models** are generally preferred, as they display more in vivo-like cell-cell and cell-ECM communications, which is especially relevant for the cardiac constructs, as the contraction depends on an adequate electro-mechanical coupling [15]. Most of the current platforms should be seen as ventricle-on-a-chip, as the used CMs come from the ventricular chamber, due to the critical importance of ventricular dysfunction in heart failure [16]. The first example of a microphysiological system to model cardiac tissue was based on a cell culture platform with two Velcro-covered glass tubes that functioned as anchor points for a neonatal rat CMs suspension in collagen. These structures allowed cell attachment and compaction, resulting in a self-assembled tissue in which the static tension led to a high degree of alignment in the direction of the posts [17]. Further developments of this system resulted in a

change of the glass pillars for flexible PDMS microposts, whose bending could be related to the contraction dynamics of the tissue [18].

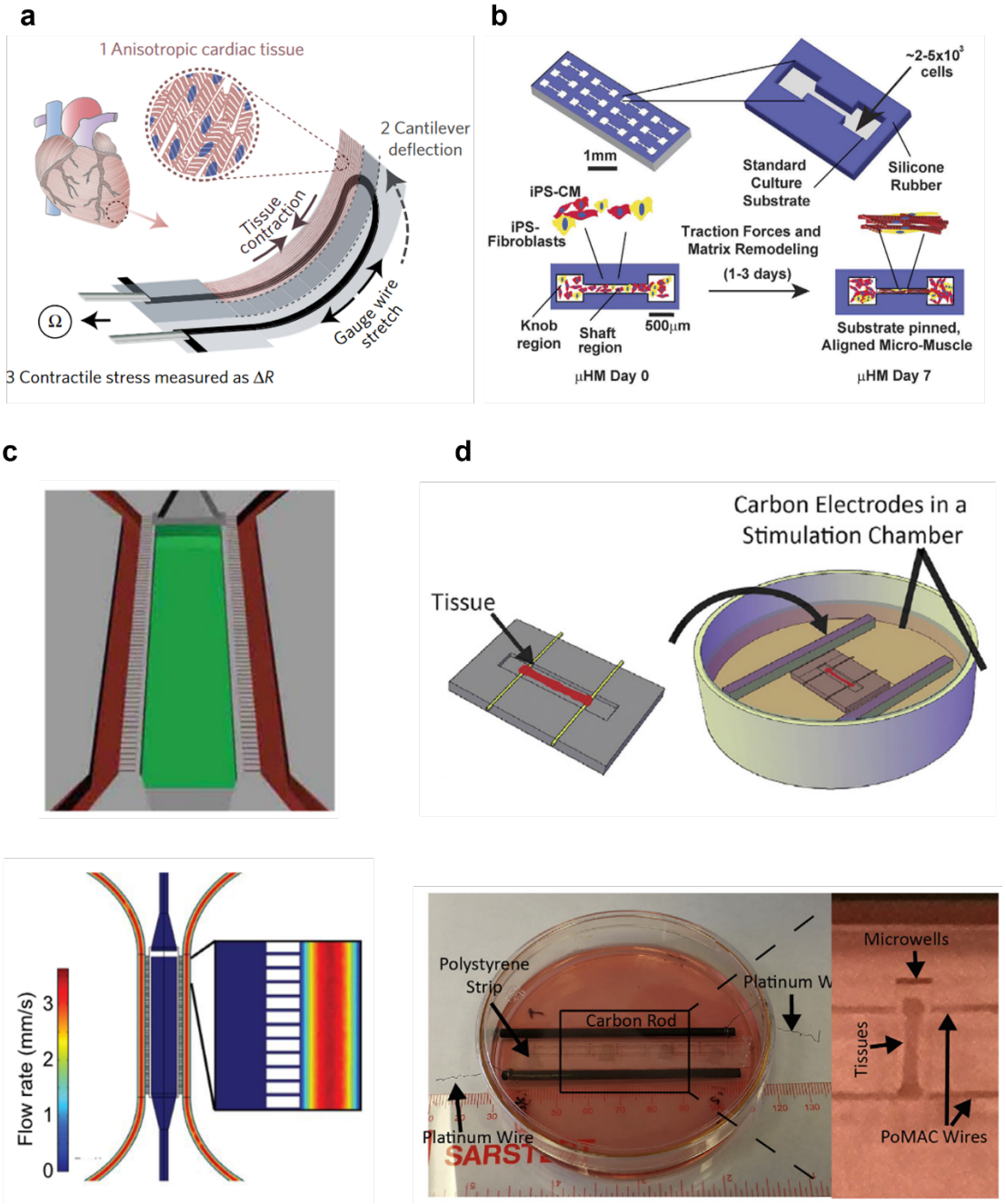

Figure 15 Microphysiological systems to model cardiac tissue. (a) Muscle thin film created on top of a 3D printed strain sensor. **(b)** Elongated tissues formed by compaction within microgroove structures or **(c)** by spatial confinement in a chamber with perfusable microchannels. **(d)** Elongated tissues formed by self-assembling around double elastic force sensors. *Adapted from [2].*

Most of the subsequent studies have adopted this approach using pillars or wires to anchor the tissue and induce a high degree of anisotropy in 3D. For instance, a MPS used soft-lithography to generate a miniaturized I-shaped tissue with two rigid anchoring wires and a force sensor

located in the centre of the construct allowed to measure the contraction force [19]. Other geometries have also been proposed using soft-lithography techniques such as perfusable tubes [20]. Recently, a platform known as Biowire, which is made of polystyrene and two elastic wires as anchor points for the tissue, has been put forward as an innovative platform to move away from PDMS, which has problems related to hydrophobic compounds absorption [21]. Some different approaches to the anchoring structures have also been proposed, such as cardiac muscle thin films using multimaterial 3D printing, in which a highly conductive piezo-electric composite was embedded in a biocompatible surface for CM culturing, allowing for continuous contraction sensing [22]. As previously commented, the most important issue to be addressed in MPS is tissue maturation. Cells derived from hiPSC have many features of immature or fetal CM, such as a low percentage of binucleated cells, non-anisotropic distribution of tight junction proteins such as connexin-43 (Cx-43) which results in low conduction velocities, underdeveloped sarcomeres, or lack of a positive-force-frequency response [23-26] On top of that, mitochondria are less mature and numerous in hiPSC-CM, which is correlated to a metabolism mostly based on glycolysis, instead of β-oxidation of fatty acids as in adult CM [27]. However, it is possible to drive cell maturation using a variety of approaches.

One of them is long-term culture (up to 6 months) has been shown to improve alignment, Z-disc and action potential profiles [28]. The use of perfusion or dynamic cultures is another strategy that resulted in contraction forces and conduction velocities close to adult CM, as cells are exposed to higher nutrient availability and shear stress [29]. Biochemical conditioning such as β-adrenergic stimulation has been shown to improve the force of contraction and cellular hypertrophy by upregulating structural proteins [30]. Co-culture of CM with stromal cells (such as cardiac fibroblasts) is essential to enhance properties such as cell morphology or conduction velocity [31]. Finally, important microenvironment cues such as static electromechanical stimulation highly improve different aspects of tissue development such as contractility or cell alignment [32-34]. Interestingly, recent studies have shown that subjecting the cardiac tissues to a ramping electrical pacing at a rate of 0.33 Hz/day to a maximum value of 6 Hz can lead to an adult-like phenotype in terms of calcium handling and action potential properties, positive force-frequency response, T-tubule formation, sarcomere structures length and even the presence of M-lines [35].

Although most of the MPS work with ventricular tissues, there are a few recent studies focused on developing adult-like atrial models. These cells have different properties in terms of genetic, electrophysiology and structural proteins [36,37] For instance, atrial cells express the myosin light chain 2a (MLC2a), while ventricular ones express the MLC2v [36]. There are limited studies reporting atrial differentiation protocols [38], although some successful studies have been

performed using the Biowire platform, in which the atrial phenotype has been validated using drugs that specifically affect this cell type such as carbachol [21]. That study went even further to develop a heteropolar tissue, in which differential drug responses were observed on the atrial and ventricular sides [21]. Although the implantation of an atrioventricular conduction system (Purkinje fibers) is still needed, this approach opens unprecedented possibilities to evaluate chamber-specific drugs and avoid off-target effects [39]. Therefore, cardiac microphysiological platforms combined with stem cell technology are proving to be a highly promising way to test new drugs. Human iPSC-CM extracted from patients contain the disease-specific genotypes that lead to disease progression [31,40]. Genetic disorders can also be generated in healthy cells using genetic editing such as CRISPR [41]. Both monogenetic diseases, such as long QT syndrome caused by a mutation in the KCNQ1 gene leading to ventricular arrhythmias [42].

In this chapter, we report the development of an innovative MPS combining topographical signaling cues created with electrospun nanofibers with electrical stimulation in a microfabricated system. The significance of this work relies on the possibility to incorporate both cues in a robust, reproducible, and cost-effective system. The final device is conceived as an easy-to-use platform that can be of great value to the cardiac research community, due to its low cost, high imaging compatibility, versatility, and high-throughput configuration capabilities. To achieve this goal, we propose a method to deposit electrospun fibers on thin commercial coverslips and bond them to a microfluidic device made in polydimethylsiloxane (PDMS). We also characterized this substrate and developed an experimentally validated computational model of the device to optimize the best electrical stimulation configuration, in terms of magnitude and uniformity, in the cell chamber region. As proof of the functionality of the system, we co-cultured cardiac fibroblasts and cardiomyocytes from neonatal CD1 mice and quantified cell orientation and elongation by immunostaining for specific cardiac markers (such as troponin T). In addition, the maturation of the developed construct was analyzed using specific genes involved in the conductive and contractile properties of cardiac tissues by real-time polymerase chain reactions (qRT-PCR).

4.2 Materials and methods

4.2.1 Electrospinning and characterization of the nanofibers

Poly-L/DL lactic acid 70/30 (PLA 70/30) (Purasorb PLDL 7038, viscosity 3.8 dl/g at 25 ºC, Purac Biomaterials, NL) was dissolved at 8 % w/w in 2,2,2-trifluoroethanol (99.8 %, Panreac, ES). To acquire fluorescent nanofibers, rhodamine B (Sigma, DE) was also added at a final non-cytotoxic concentration of 0.01 % w/v. The solution was loaded into a 5 ml syringe (Becton-Dickinson, US) and delivered through a 21-gauge blunt-tip needle (Nordson EFD, US) at a flow

rate of 0.5 ml/h using a syringe pump (NE-300, New Era Inc, USA). Fibers were electrospun using a high-voltage power supply (NanoNC, KR) onto a grounded stationary collector placed at a distance of 20 cm from the tip of the syringe. The collector was round in shape, with a diameter of 9 cm and around which we wrapped pieces of aluminum foil of 20x33 cm with three 0.17 mm coverslips (Deltalab, ES) secured with tape following the middle axis of the rectangle. To obtain randomly distributed fibers, the collector was kept static for 2 min and the power supply configured at 9 kV, while for the aligned fibers the collector was set at a rotating speed of 1000 rpm for 6 min with a potential of 12 kV. A focusing ring-shaped electrode was also used in the latter case to restrict the deposition area of the electrospinning jet.

The morphology of the fibers was assessed using a field emission scanning electron microscope (NOVA Nano SEM 230, Fei Co., NL) operating at 10 kV and covered with an ultra-thin gold layer (10 nm) deposited by thermal evaporation (Univex 450B, Oerlikon Leybold Vacuum, DE). SEM images were processed in Image J (NIH, US) to obtain different parameters of interest. To obtain fiber alignment information, the Oval Profile ImageJ [43,44] plugin was used. Briefly, it performs an oval projection of the Fast Fourier Transform (FFT) of the images followed by a radial summation of the pixel intensities for each angle between 0 and 180º (as de FFT data are symmetric). The degree of alignment is reflected by the height and shape of the peak, which indicates the principal angle of orientation. The mean fiber diameter and the standard deviation were also assessed by performing 18 measurements on both random and aligned samples. Finally, the stiffness of the fibers was assessed by calculating the approached elastic modulus in a tensile strain assay using a Zwick-Roell Zwicki-line Z0.5TN universal testing machine (Zwick-Roell, DE) and a 10 N force cell. The number of replicates was 5 and the speed of assay was set to 10 mm/min.

4.2.2 Device design and fabrication

The microfluidic platform design (see **Fig.16-a-c**) consists of a main cell culture chamber (1300 µm wide, 8800 µm long, 150 µm high) flanked by two media channels (750 µm wide, 150 µm high). There are also four 1.2 mm holes tangent to the media channels to place the rod-shaped electrodes needed to electrically stimulate the cardiac cells. Master molds, PDMS replicas, cleaning and bonding were performed following the same procedures as previously described in section 3.2.2. The diameter used for the holes in this device was 6 mm for the media reservoirs and 1.2 mm for the cell chamber inlets and electrode holes. As previously explained, the coverslips were patterned with electrospun nanofibers in either a random or aligned fashion. Due to the high hydrophobicity of the PLA 70/30 [45], we removed most of the unused deposited fibers before the plasma treatment with a stray wet in acetone, leaving just an area slightly bigger than the cell culture chamber. That way, the PDMS frame acted as a holder for the fibers, so they

remained in a fixed position. Finally, all the chips were thermally treated for 2 h at 85 ºC to stabilize the bonding. We were aware that the glass transition temperature (T_g) of PLA electrospun fibers ranges 57-58 ºC [46]. However, we did not observe any effect on the topography of the fibers. Then, all chips were sterilized by putting them under UV light for at least 30 min.

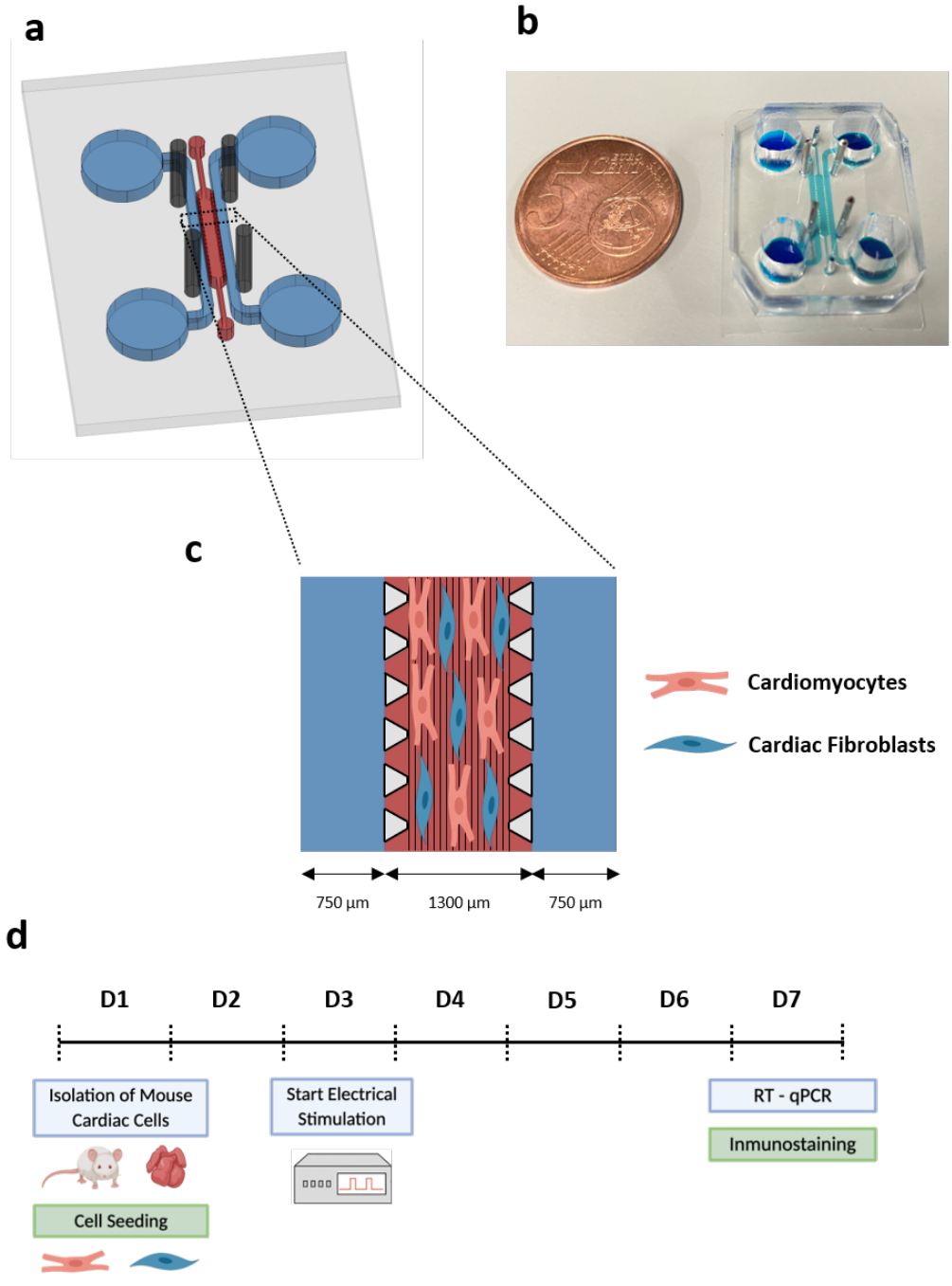

Figure 16 Design and cell culture model of the microfluidic platform aimed at the generation and maturation of highly anisotropic cardiac tissue. (**a**) Schematic representation of the microfluidic device including the cell chamber (red), the media channels (blue), and the stimulation electrodes (dark gray). (**b**) Photo of the assembled microfluidic platform. (**c**) Detailed schematic view showing the patterned substrate created with electrospun fibers in the cell chamber and how the cardiac cells follow its orientation. (**d**) Timeline of the experiments.

4.2.3 Finite element modelling of the electrical field

A computational model of our microfluidic platform was developed using the finite element method (FEM) to obtain the distribution and magnitude of the electric field. The area of interest considered corresponds to the cell chamber located between the two pairs of rod-like electrodes and in which the cells are seeded and grown as a monolayer (area ≈ 11.4 mm^2). The 3D geometry of the device was divided into three different homogenous domains: (1) the fluid domain representing the culture medium, (2) the stainless-steel electrodes, and (3) the PDMS frame and posts, each with their respective electrical properties [47] (see **table 1**).

Materials	Conductivity (σ) [S/m]	Permittivity (ε)
Culture media	1.5	80.1
PDMS	$1*10^{-22}$	2.63
Stainless steel	$1.32*10^{6}$	1.005

Table 1 Electrical properties of the three domains within the MPS.

The electric field distribution was computed with the software COMSOL Multiphysics 5.5 (Comsol Inc., US). Numerical simulations were performed using the Electric Current interface, assuming direct-current (DC), steady-state conditions to solve Maxwell's equations, for which the governing equation is:

$$-\nabla.(\sigma\nabla C - J_e) = Q_i$$

Where V is the electric potential, σ is the electric conductivity, J_e is the generated current density and Q_i is the local current source. The electric field can be derived from the potential V obtained in the aforementioned equation as $E = -\nabla V$ assuming electroquasistatic conditions. Regarding the boundary conditions, one pair of the stainless-steel electrodes were grounded, while the other pair was set to the different electric potentials. The electrospun-coated glass surface was considered an electrically insulating boundary condition. The geometry was discretized with a tetrahedral mesh with approximately 40.000 elements and calculated using a direct solver based on the PARDISO method. Mesh sensitivity studies were conducted to ensure consistency of the results.

4.2.4 Validation of the electrical model

In order to validate the computational model of the electrical stimulation, electrical signal recordings were performed in different places inside the microfluidic system. We used a variation of the design with the electrodes placed at 1 mm from the cell chamber inlets to avoid

measurement problems, such as the accidental contact of the voltage probe with the electrodes. To perform the measurements, holes were made during the fabrication of PDMS devices used for this test in three different positions of the cell chamber: (1) between the 2nd and 4th rows of posts starting from one of the inlets of the cell chamber, (2) between the 9th and 11th rows of posts from the chosen inlet and, (3) between the 2nd and 4th rows of posts starting from the opposing inlet. The chip was filled with PBS (100 µl/reservoir) and the stimulation electrodes were placed in their corresponding holes and connected to a function generator (Agilent 33250A, US) using a coaxial-alligator cable. One pair of electrodes on one side of the chamber was grounded, while in the other pair a biphasic wave was applied to range from -2.5 V during 1 ms to +2.5 V during another 1 ms (so V_{pp} = 5 V and the total duration of 2 ms). The frequency of the signal was set at 1 Hz. To perform the measurements, a stainless-steel needle was connected to a digital oscilloscope (Keysight DSOX 3024T, US) and used as a voltage probe in each of the holes made in the device. The measurements were performed on a total of three independent devices.

4.2.5 Isolation and seeding of mouse cardiac cells

Cardiac primary cells were obtained from CD1 neonatal mice as previously described [48]. Hearts from 1-3-day-old mice were extracted and transferred on ice into a solution of PBS with 20 mM 2,3-butanedione monoxime (BDM, Sigma, DE), where they were cleaned and minced into small pieces using curved scissors (approximately 0.5-1 mm3 or smaller). Then, tissue fragments underwent a predigestion step by incubating in a trypsin-EDTA solution at 0.25 % (Sigma, DE) with 4 µg/mL of DNase I and 20 mM BDM and subjected to 20-25 cycles of enzymatic digestion using collagenase II (Thermo Fisher, US) and dispase II (Sigma, DE) in L-15 medium (Sigma, DE) with 20 mM BDM. Pooled supernatants were collected through a 70 µm nylon cell strainer (Corning, US) and centrifuged at 200 G for 10 min. The pellet was resuspended in DMEM containing 1 g/L glucose (Thermo Fisher, US) supplemented with a 19 % of M-199 medium (Sigma, DE), 10 % horse serum (Sigma, DE), 5 % fetal bovine serum (Sigma, DE) and 1% penicillin and streptomycin (Thermo Fisher, US). The cell suspension was plated into a cell culture dish in order to separate most of the non-myocytic cell fraction of the heart and avoid excessive proliferation in subsequent experiments. After 1 h of incubation, the supernatant containing a purified population of cardiomyocytes was collected in a 0.5 ml Eppendorf.

4.2.6 Cell culture and electrical stimulation

Isolated cardiac cells were centrifuged and resuspended at a density of $20*10^6$ cells/ml in culture media, which is composed of DMEM containing 4.5 g/L glucose (Thermo Fisher, US) supplemented with 17% of M-199 medium (Sigma, DE), 4 % horse serum (Sigma, DE) and 1% penicillin and streptomycin (Thermo Fisher, US). Before cell seeding, all devices were coated with porcine gelatin (Sigma, DE) at 0.5 % w/v in distilled water for 1 h at 37 ºC. Approximately

10 µl of the cell suspension (~200.000 cells/device) were injected into the microfluidic system and incubated at 37 ºC for approximately 4 h to allow cell attachment. Then, the chip channels were hydrated by adding 60 µl of cell culture media in each of the reservoirs on one side of the chamber and gently aspirating from the other end with a 1 ml pipette with the tip cut to fit the size of the reservoirs. Finally, each reservoir was filled with medium (approximately 120 µl), and each chip was kept inside a 100 mm Petri dish in a 37º C, 5 % CO_2 incubator with daily changes of media for the duration of the experiment (7 days).

Electrical stimulation was started on day 3 to provide cells with enough time to recover from the isolation procedure. To apply the stimulation, AISI 304 stainless steel electrodes were made by machining 20G microlance needles (Becton Dickinson, US), yielding cylinders of 0.86-0.92 mm in diameter and 2 cm in length, which fitted into the 1 mm dedicated holes of the device. An alligator clip was clamped to each pair of electrodes and then connected to a coaxial-alligator cable coming from a function generator (Agilent 33250A, US). A small groove was machined in the Petri dishes to easily take the cables out. A biphasic wave of V_{pp} = 5 V, 2 ms in width, and a frequency of 1 Hz was applied, which are the recommended parameters according to the most established protocols [49,50]. The electrical stimulation was maintained for 5 days before the final readouts (see the experimental timeline in **Fig.18-d**).

4.2.7 Immunostaining and quantification of cell alignment and Cx-43 expression

Cardiac cells were fixed after 7 days in culture with 4 % paraformaldehyde (Electron Microscopy Sciences, US) for 15 minutes after washing cells twice with sterile 1x PBS. Then, they were washed again with 1x PBS and permeabilized with a solution of Triton X-100 (Sigma, DE) at 0.1 % v/v in 1x PBS with glycine (Sigma, DE) at 0.15 % w/v (PBS-gly) for 15 min. After that, cells were treated for 2 h with a blocking solution of bovine serum albumin (Sigma, DE) at 5 % w/v in PBS-gly to prevent non-specific antibody bindings. Samples were then incubated overnight at 4 ºC with rabbit polyclonal antibody against connexin-43 (Abcam ab11370, UK) (1:400) in blocking solution and mouse monoclonal antibody against cardiac troponin T (Abcam ab8295, UK) (1:200). The next day, samples were incubated for 2 h at room temperature with Alexa 488 against mouse antibody (Abcam ab150117, UK) and Alexa 635 against a rabbit antibody (Thermo Fisher, US), both at 1:200 in blocking solution. A counterstaining for cell nuclei were also performed by incubating DAPI (Thermo Fisher, US) (1:1000) in PBS-gly for 10 min at room temperature. Samples were then rinsed three times in PBS-gly and maintained at 4 ºC in the same solution until image acquisition.

Imaging was performed on a Leica Thunder fluorescence microscope (Leica Microsystems, DE) with the same acquisition parameters for all the samples (exposure time, LED power, etc.)

and the obtained images were processed using Image J software [45] (NIH, US). To quantify cell alignment, we used the plugin Orientation J to obtain the orientation and isotropy properties of the images based on the evaluation of the gradient structure tensor [51]. The expression of the protein connexin-43 was also estimated from the acquired images. Briefly, the procedure consists of removing the background illumination of the DAPI and Cx-43 images, converting them to grayscale, and then binarizing them by applying automated thresholding based on the Otsu method. Finally, the number of objects for each image is labeled and counted using the Analyze Particles plugin of Image J. The amount of Cx-43 dots is divided by the number of cell nuclei, which results in a normalized core for the quantity of gap junction proteins per cell. Two images per device from a total of three replicates were considered for each of the two experimental conditions (random fibers without electrical stimulation and aligned fibers with electrical stimulation).

4.2.8 Real-time quantitative PCR

qRT-PCR analyses were performed for a range of cardiac markers using the StepOnePlus RT-PCR System (AB Applied Biosystems Life Technologies, US). To isolate RNA from our microfluidic system, cells were thoroughly washed with sterile 1x PBS (five washing steps with 4 min intervals of incubation) to remove all traits of phenol red present in the cell culture media and avoid further interference in downstream reactions. Then, a buffer provided in the RNeasy Plus Micro kit (Qiagen, NL) was used to lyse the cells (60 µl per upstream reservoir followed by a 5 min incubation). The lysate was then collected from one of the cell chamber inlets into a 0.5 Eppendorf vial and homogenized vortexing it for 1 min. The remaining isolation steps were performed following the manufacturer's protocols, including the removal of gDNA. The quality and concentration of the extracted RNA samples were assessed using a Nanodrop 1000 spectrophotometer (Thermo Fisher, US). After this step, the RNA was transcribed into cDNA using the RT2 First Strand Kit (Qiagen, NL) and real-time PCR was performed with the RT2 SYBR Green Mastermix (Qiagen, NL) following the manufacturer's protocols. Specific primers for amplifying TNNI3, GJA1, and MYH6, MYH7, and housekeeping gene R18S were used (Qiagen, NL). Data obtained by qRT-PCR were analyzed using the ΔΔCt method. Two replicates were considered for each of the experimental conditions (aligned fibers with and without electrical stimulation), each one using the RNA harvested from just a single microfluidic device.

4.2.9 Statistical analysis

All data were statistically analyzed following the same procedure as presented in section 3.2.9.

4.3 Results and discussion

4.3.1 Fabrication of microfluidic devices with nanopatterned substrates

Our results show that the electrospinning of nanofibers is an effective way to generate either random or aligned nanotopographies for microfluidic devices, as observed in SEM micrographs (**Fig.17-a,b**). The differences in fiber orientation were quantified by performing an FFT analysis and radial summation of the oval profile of SEM images. A clear peak at 90º can be observed for the aligned fibers (**Fig.17-c**) while a random distribution at different angles is seen for the randomly distributed ones (**Fig.17-d**). A series of different electrospinning parameters were tested till the optimal configuration was found, which yielded continuous and homogenous fiber thicknesses of 1702.3 ± 128.9 nm for the random fibers and 697.3 ± 30.9 nm for the aligned ones (**Fig.17-e**) with no bead content. The approached elastic modulus was isotropic for the random nanofibers, with a mean value of 21.1 ± 3.9 MPa, while for the aligned ones the value in the direction of the fibers was 516.5 ± 80.3 MPa (**Fig.17-f**).

A robust method to incorporate the electrospun substrates into our microfluidic system was also developed. As the high hydrophobicity of the PLA fibers (~130º) [47] hampers the bonding process of the coverslips to the PDMS devices, we carefully removed most of them from the substrate with a stray bathed in acetone, leaving only a small rectangle slightly bigger than the cell chamber (around 2 cm wide and 10 cm long). This allowed the PDMS frame to hang on and fix the fibers preventing their detachment from the coverslip when immersed in cell media. The bonding process could be successfully performed for all the experiments, and we did not observe any leakage of media during cell culturing within the devices. Another advantage of using PDMS as a frame is its transparency, which together with the fact that we use thin coverslips as substrates (0.17 mm) and low thickness electrospun layers (~12 μm), makes our device compatible with high-resolution imaging platforms such as confocal microscopes.

Overall, we consider electrospinning to be a much more robust, reproducible, cost-effective, and scalable approach to generate nanopatterned substrates for microfluidic chips than previously presented methods such as microcontact printing [7,52,53], hydrogel patterning with microfluidic channels [8,9], or hot embossing [11]. It is a single-step procedure performed with commonly used equipment (such as pumps, or a high voltage source) while previously used techniques are multistep and require expensive microfabricated molds generally obtained through photolithography. It also offers high versatility, as it is possible to easily customize many different fabrication parameters such as fiber orientation, thickness, length, positioning density or type of polymer material (natural, synthetic, or blended) [54-56]. In our case, we chose PLA 70/30 due

to its excellent biocompatibility and cell adhesion properties observed in previous works from our group [45,57].

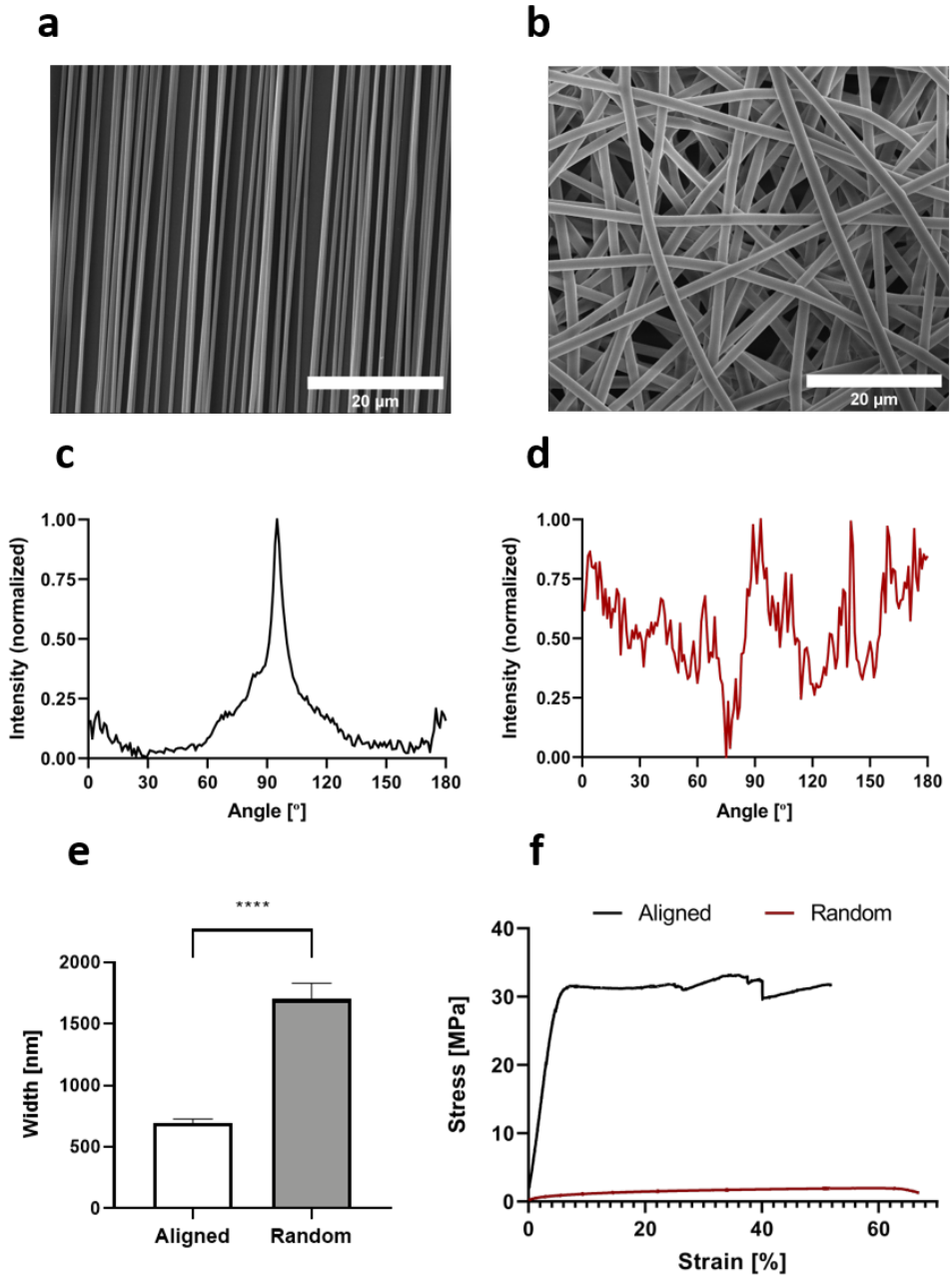

Figure 17 Electrospun fibers characterization. (**a,b**) Field emission scanning electron microscopy (SEM) images showing the morphology of the aligned and random fibers respectively. (**c,d**) FFT analysis of the nanofiber orientation based on the SEM images. (**e**) Mean nanofiber diameter for each of the conformations. (**f**) Characteristic stress-strain curves were obtained for the tensile mechanical assay of each sample type. Scale bar in (a,b) = 20 µm. Data in (e) expressed as mean ± standard deviation (n = 18) with ****p < 0.0001 (evaluated with Student's t-test).

The mechanical strength and chemical stability of this material make it compatible with procedures such as plasma bonding or UV light sterilization, which is an important limitation of the techniques that rely on natural polymers such as collagen, which tend to collapse due to their

low ultimate strength and undergo degradation when exposed to UV light [58]. Finally, our device can also be easily customized to incorporate perfusion by changing the size of the reservoirs and connecting it to a pumping system by using the appropriate tubing. This is something that cannot be easily addressed in most of the previously presented methods, which generally rely on systems placed inside well-plates or Petri dishes [10,11,59,60], in which incorporating perfusion is not even an option.

4.3.2 Electrical stimulation model of the microfluidic system

The development of a reliable electrical model for our platform is essential in order to demonstrate that our approach can generate the required conditions to optimally stimulate cardiac cells. It is generally considered that a uniform electrical field of 5 V/cm, 2 ms in duration, and 1 Hz in frequency can mimic the characteristics of the electrical impulses in murine native myocardium [59]. After performing some preliminary testing, we found that placing the electrodes tangent to the media channels and aligned with cell chamber inlets yields the best trade-off between design simplicity and maximizing the electrical field strength in the cell chamber. Then, we evaluated the possibility of performing the stimulation using just two rod-shaped electrodes at each end of the chamber. Unfortunately, we found that this was not a suitable approach, as the generated field was not homogeneous because the x-components (corresponding to cell chamber width direction) did not cancel each other (see **Fig.18-a**).

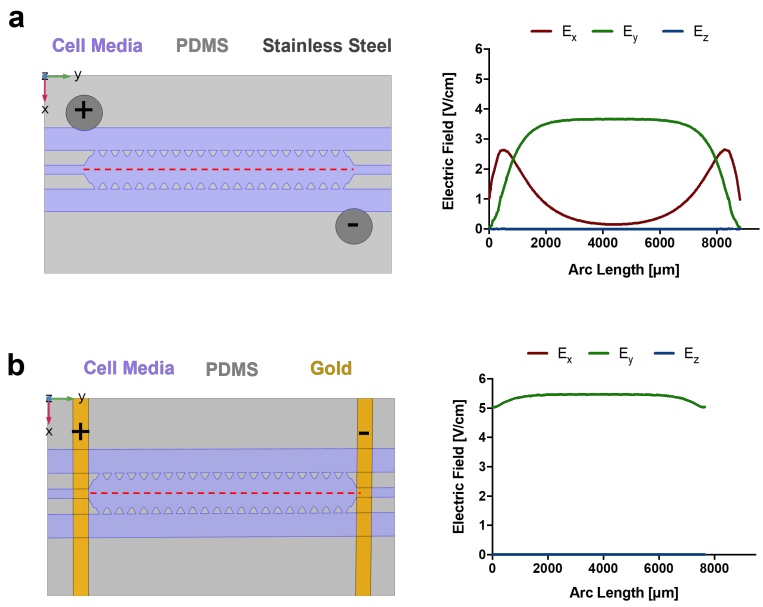

Figure 18 Electrical finite element model results for preliminary evaluation of stimulation approaches. (**a**) Layout and materials composing the different parts of the system and electrical field intensity corresponding to the longitudinal section decomposed in its different components (x,y,z) for the two stainless steel electrodes configuration. (**b**) Layout, materials and electrical field intensity for the planar gold electrodes configuration. The red line indicates the section across which the electrical field was computed (z = 75 µm). All results were calculated for an input voltage of 5 V_{pp}.

To solve this problem, we introduced two extra electrodes placed symmetrically at each end of the chamber (see **Fig.19-a**), which proved to completely remove the x-component (see **Fig.19-b**). This makes the field to be completely homogenous in the length direction (y-component) for most of the cell chamber, with the logical perturbations around the PDMS posts structures due to the insulator properties of this polymer. This is further confirmed by observing the field lines (**Fig.19-c**), which show that the current flow goes completely in the electrode-electrode direction (matching also with the alignment of the electrospun fibers). This is an important point, as it has been shown that cardiomyocytes are more excitable when their long axis is parallel to the electrical field lines [59,61], so the electrical field should ideally go in the same direction as the contact cues. Another interesting point is that the required input voltage to generate a field of around 5 V/cm is significantly lower in the case of the four-electrode configuration (around 5 V) than in the two-electrode one (around 8 V). In both cases, we observed that the z-component is zero, which means that the homogeneity is maintained for all the height of the chamber.

Regarding the validity of the simulations, we have to consider that they are performed under steady-state conditions. Any bioreactor using solid electrodes to apply electrical stimulation has a dynamic electrical behavior that derives from the way the charge is transduced into the electrolyte (generally cell media). This process occurs via reversible and non-reversible faradaic reactions and the non-faradaic charging/discharging of the double layer formed in the electrode/electrolyte interface [50]. In our case, we consider the steady-state conditions as an electroquasistatic approximation of the dynamic electrical behavior of the system, which gives us detailed spatial information rather than a description of the time evolution of the system. This is a valid assumption when considering homogenous, isotropic media, and wavelengths under 10 kHz [49,60], all of which are fulfilled in our experiment.

To make sure that the developed electrical model is able to predict the actual electrical field distribution in our device, we compared the theoretical voltage curve obtained in the simulations with experimental measurements performed in three different positions inside the cell chamber (see **Fig.20-a,c**). The pulse characteristics were the same as in the cell stimulation protocol: biphasic wave with an amplitude of 5 V_{pp}, 2 ms in duration, and 1 Hz in frequency. We evidenced that the experimental measurements perfectly matched the theoretical curves with minimal differences between devices (see **Fig.20-b**). For the first position (approximately 1408 µm from the start of the cell chamber) we measured a value of 3.31 ± 0.03 V, which is close to the 3.28 V estimated in the finite element simulation. For the second and third positions (4208 µm and 7008 µm respectively from the chamber inlet) we obtained values of 2.55 ± 0.03 V and 1.77 ± 0.02 V which also matched the estimated simulation values of 2.52 V and 1.72 V.

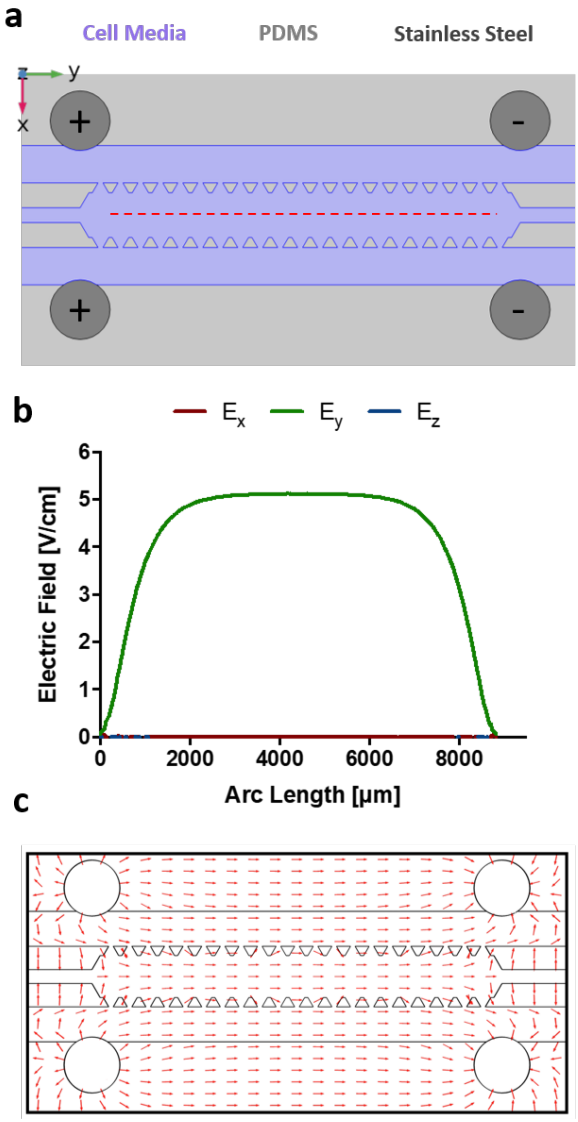

Figure 19 Electrical finite element model results. (**a**) Layout and materials composing the different parts of the system: the cell chamber filled with culture media, PDMS frame and posts, and four stainless-steel electrodes. The red line indicates the section across which the electrical field was computed (z = 75 µm). (**b**) Electrical field intensity corresponding to the longitudinal section previously indicated decomposed in its different components (x,y,z) for an input voltage of 5 V_{pp}. (**c**) Electrical field vectors in a cross-section of the cell chamber (z = 75 µm), indicative of the direction of current flow.

4.3.3 Comparison of the developed system to "gold standard" planar electrodes

The use of rod-shaped carbon electrodes is the most common approach to stimulate cardiac cells in macroscale platforms, due to their excellent properties in terms of biocompatibility and injected charge (95 % of charge is transduced into the bioreactor during the stimulus pulse) [49]. However, they cannot be easily integrated into microfluidic platforms because of their poor mechanical properties. The most common approach to stimulate this type of cell in microsize devices is the deposition of planar microelectrodes on fixed positions of the substrate [11,60].

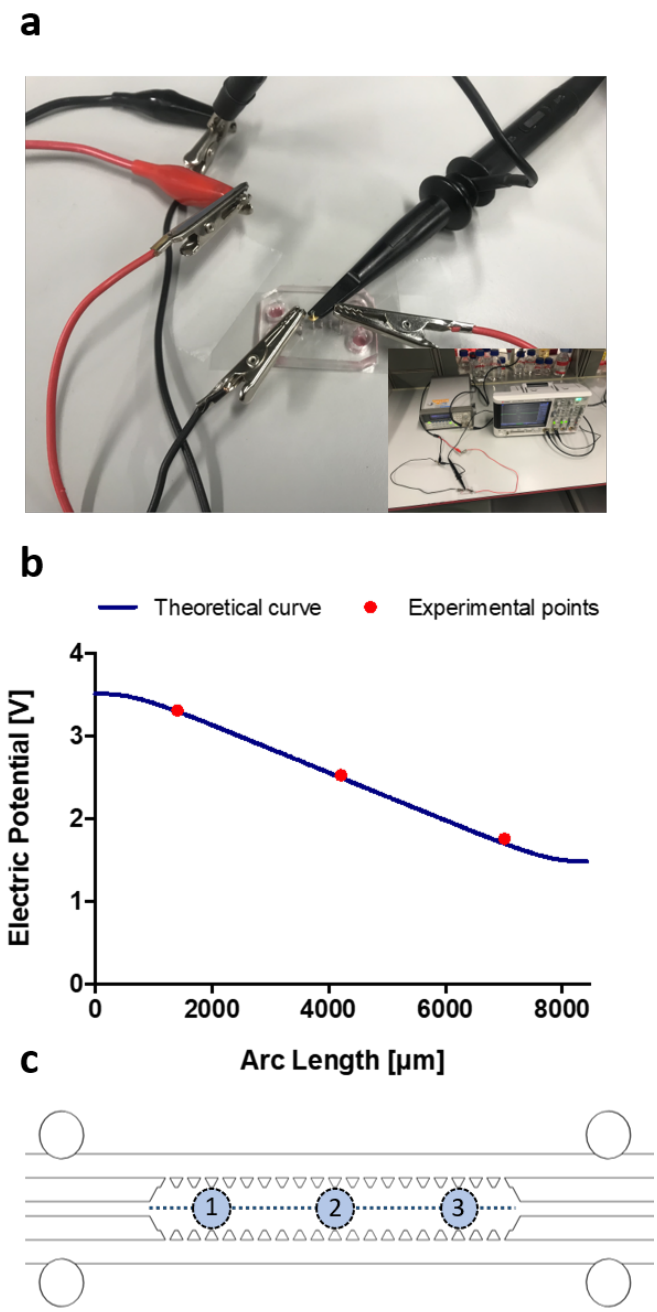

Figure 20 Electrical characterization of the device. (**a**) The experimental setup used to perform the voltage measurements. (**b**) Comparison of the theoretical curve obtained in the FEM simulations for the electrical potential concerning the experimental voltage measurements (red dots). (**c**) Schematic of the device showing the section for which the electric potential was calculated in the simulations ($z = 75$) and the three holes performed in the cell chamber of the device to obtain the experimental measurements. Experimental data in (b) expressed as mean ± standard deviation ($n = 3$). Note that the error bars cannot be seen because of the really small deviations: ± 0.03 V for points number 1,2 and ± 0.02 for point number 3.

Since this approach is considered the gold standard, we compared our system to an equivalent version in which planar electrodes were used. To that end, we performed a simulation considering the patterning of two rectangular gold electrodes (120 µm in width and 800 nm in height based

on the parameters from a previously proposed system [11]) in the same position as the rod-shaped stainless-steel ones (aligned with the cell chamber inlets).

The results of the simulation (**Fig.18-b**) show that the planar electrodes require just a slightly lower input voltage (around 4.6 V) to generate the 5 V/cm field compared to the four-electrode configuration (~5 V). Another difference is that the field is completely homogenous for all the length of the chamber, while in the 4-electrode configuration there is a slope to reach and drop from the 5 V/cm value for approximately the first and last millimeter of the chamber. However, the use of planar electrodes has many limitations: its microfabrication is generally a complex procedure requiring expensive equipment (such as photolithography mask aligners or evaporators) and materials (gold, platinum, etc.) with the resulting devices being generally not reusable due to the irreversible nature of the bonding process. Moreover, their planar nature may not ensure the uniformity of the electrical field throughout the different heights [62], which is critical in case a 3D culture is performed.

4.3.4 Generation of highly anisotropic cardiac tissue with improved maturation

Cardiac cells were seeded on our MPS to evaluate tissue alignment and maturation after 7 days in culture (5 of which were under electrical stimulation). In the case of the randomly deposited fibers, the distribution of the cardiomyocyte contractile proteins was completely isotropic, showing no preferential angle of orientation (**Fig.21-a,c**), while in the case of the aligned ones, the cells are polarized in the direction of the nanofibers (0º) with a small deviation of ± 5º (**Fig.21-b,c**). Cells were also clearly more elongated in the aligned fibers, acquiring a fusiform shape that closely mimics the morphology of cardiomyocytes found in native myocardium [20]. From the electrospinning variables, the used fiber density is probably the main regulator of the resulting tissue architecture, as it drives two processes: the first step during cell seeding and attachment, in which the fibers provide contact guidance, and the second step of intercellular guidance caused by the growth and close interaction of neighboring cells [54]. High fiber densities are recommended to obtain optimal ordering, co-alignment, and elongation of cardiac cells, so we made sure to completely fulfill this requirement by depositing around 1160 fibers/mm. This is also beneficial in terms of generating a nanoscale topography with a high specific surface area, which is essential for optimal cell attachment and growth [55].

Cardiomyocytes formed confluent cell monolayers capable of spontaneously contracting on top of the nanofibers. This is in line with previous studies that show that thin meshes provide contact guidance and oriented growth to the cells while still allowing some degree of cellular contraction [54].

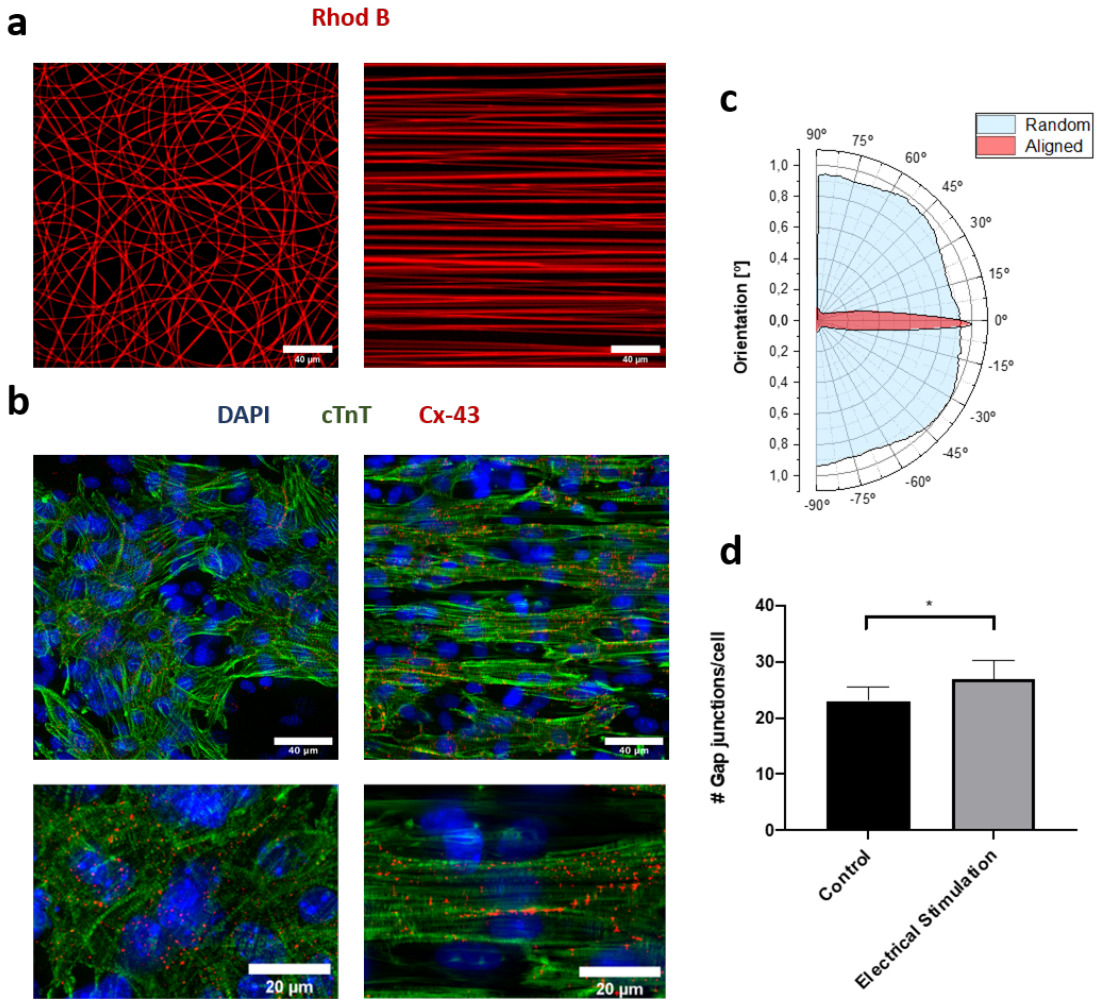

Figure 21 Immunofluorescence staining of the cardiac tissue and quantification of orientation and gap junctional proteins expression. (**a**) Fluorescent microscope images of the random electrospun fibers containing rhodamine B (red) and the cardiomyocytes seeded on top stained for the contractile protein troponin T (green), gap junctional protein connexin-43 (red), and cell nuclei (blue) after 7 days in regular culture. (**b**) Fluorescent microscope images of the aligned electrospun fibers containing rhodamine B (red) and the cardiomyocytes seeded on top stained for the contractile protein troponin T (green), gap junctional protein connexin-43 (red), and cell nuclei (blue) after 7 days in culture (5 of them with electrical stimulation). Scale bar in (a,b) = 40 µm (20 µm in magnification view). (**c**) Polar plot of the differences in the orientation between the cardiomyocytes seeded on top of the aligned vs random electrospun substrates. Results represent the normalized mean values distribution (n = 6) for different angles between -90º to 90º. (**d**) Analysis of the number of measured Cx-43 gap junctional protein (Cx-43) dots per cell. Results are expressed as mean ± standard deviation (n = 6) with *p < 0.05 (evaluated with Student's t-test).

Compared with previously presented microsystems, which are generally based on the microfabrication of geometries not naturally occurring in vivo, such as rectangular lanes made of different materials [7-11], nanofibrous scaffolds have the advantage of providing a much more physiologically relevant environment for cardiac cells as they closely resemble the native fibrous network of the extracellular matrix of the heart [63]. One important consideration is that the stiffness of the PLA fibers is several orders of magnitude higher than the physiological range for

neonatal mice [64] (around 4-11.4 kPa) or human [21] (10-500 kPa) myocardium, which has been shown to increase cardiac fibroblasts proliferation [64]. An overgrowth of fibroblasts may compromise the generation of a confluent contractile monolayer due to the limited proliferative capacity of the cardiomyocytes. Therefore, during the isolation procedure, we made sure that the cardiac cell population was highly enriched in cardiomyocytes, and cells were seeded at high densities ($20*10^6$ cells/ml). The complete removal of fibroblasts, however, is not recommended, as their presence has been demonstrated to significantly improve the morphological and functional properties of the resulting cardiac constructs [65,66].

As previously described, we also incorporated electrical stimulation into our system. We selected AISI 304 stainless steel electrodes due to their excellent biocompatibility, mechanical properties, and charge transfer characteristics from the electrode to the cell media (75 % of injected charge) [49]. One common concern about the use of these electrodes is that they are more susceptible to faradaic reactions than carbon electrodes because they leave a higher amount of unrecovered electrical charge, which makes them more likely to undergo corrosion and generate harmful byproducts [67]. However, this can be easily minimized using an adequate stimulation protocol. First, short pulses (2 ms in duration) are enough to excite cardiac cells while sufficiently short to dissipate double layer effects on the electrodes between subsequent pulses [50]. Additionally, the use of biphasic waves is an effective way to balance the charge and counteract the irreversible reactions happening at the interface of the electrodes and culture medium, which leads to an accumulation of charge with undesirable side effects (electrolysis, pH gradients, etc.) [68]. We successfully implemented this approach in our platform, as we did not observe any bubble formation at the electrode sites or changes in the color of the phenol red present in the medium during the time of culture. Moreover, with the daily change of media, we made sure that we eliminated any potential accumulation of byproducts that may have formed during the stimulation. As previously commented, cardiomyocytes tend to align parallel to the direction of the electrical field lines [59,61], while the fibroblasts strongly orient perpendicularly to the field lines, especially when DC is used [18,59]. However, previous studies have shown that the use of topographical cues saturates the cellular signaling pathways leading to cellular orientation [10,11]. As a result, the use of electrical stimulation would fail to promote further cellular elongation. Therefore, the main goal of incorporating electrical cues in our platform is to enhance the development of conductive and contractile properties of the cardiac constructs. This is an important feature, as it has been shown that electrospun fibers alone have a limited effect on cardiomyocyte maturation [69]. One of the most important points in this regard is the development of cardiac gap junctions, which are transmembrane intercellular channels that enable the propagation of electrical signals across the cardiac tissue and, subsequently, the activation and development of the contractile apparatus [70]. Immunofluorescence analyses show a moderate

but significant increase for connexin-43 (Cx-43, the major cardiac gap junctional protein in heart tissue) in the stimulated tissues compared to the controls (**Fig.21-d**). Interestingly, their distribution also shows a clear trend from being randomly dispersed in the cytosol in the case of the unstimulated controls (**Fig.21-a**) to a progressive localization in the membrane border of the elongated cells in the stimulated ones (**Fig.21-b**), which is widely considered to be their functional location in adult cardiomyocytes [71].

Several factors were taken into account to achieve an enhanced expression and localization of this protein. First, it has been evidenced that the optimal time to start the electrical stimulation is between 1-3 days after cell seeding [50]. If applied too early, cells will not have time to recover from the isolation process, and the production and reassembling of conductive proteins will be inhibited, leading to poor contractile behavior. On the other hand, if applied too late the effects of the stimulation will be minimal due to the reduced amount of contractile properties available in the cells [59]. Additionally, the use of biphasic pulses has been shown to yield better functional and structural properties in cardiac constructs compared to monophasic pulses [72]. This is attributed to the synergistic effect of the two phases of the pulses, with the first one acting as conditioning subthreshold prepulse and the second phase as an excitatory pulse [73].

We further studied the effects of our electrical stimulation setup in driving cell maturation by analyzing the transcriptional expression of several key cardiac markers. On the one hand, we focused on the development of functional gap junctions and cell-to-cell coupling by analyzing the GJA1 gene, which encodes the connexin-43 protein. We observed a 2.5-fold increase in the expression of this gene in the electrically stimulated samples compared to the unstimulated controls (**Fig.22-a**), which closely agrees with the Cx-43 expressed at the protein level and supports the idea that electrical stimulation is the main factor enhancing cell maturation. We also evaluated the development of the contractile apparatus by quantifying the TNNI3 gene, which encodes cardiac troponin I, a key component of the actin-based thin filaments. Interestingly, we found a 7-fold increase in the expression of this gene compared to the unstimulated samples (**Fig.22-b**). This result suggests a higher degree of maturation, as this isoform of the troponin is often associated with an adult phenotype [70]. The values obtained for both the TNNI3 and GJA1 are in the range reported for macroscale bioreactors [74], showing the capabilities of our miniaturized system in achieving similar degrees of maturation to much more complex and costly setups.

We also evaluated MYH6 and MYH7 genes, which respectively encode the α-(fast) and β-(slow) heavy chain subunits of the cardiac myosin. The β-subunit is associated with a more adult-like phenotype, while the α-subunit tends to be higher in a fetal stage [75]. Therefore, it is important to quantify the β-MHC/α-MHC ratio, as it increases with the developmental stage [70].

We found lower levels in the expression of MYH7 concerning MYH6 in electrically stimulated samples compared to controls (**Fig.22-c**). We believe that this fact is derived from the limitations of the 2D configuration, as these proteins are more dependent on mechanotransduction pathways than troponin for their development [76,77]. In 2D setups, the use of high stiffness substrates prevents the same level of contraction and remodeling as in highly compliant 3D scaffolds, which leads to some degree of degradation and decrease in the synthesis of sarcomeric proteins [78].

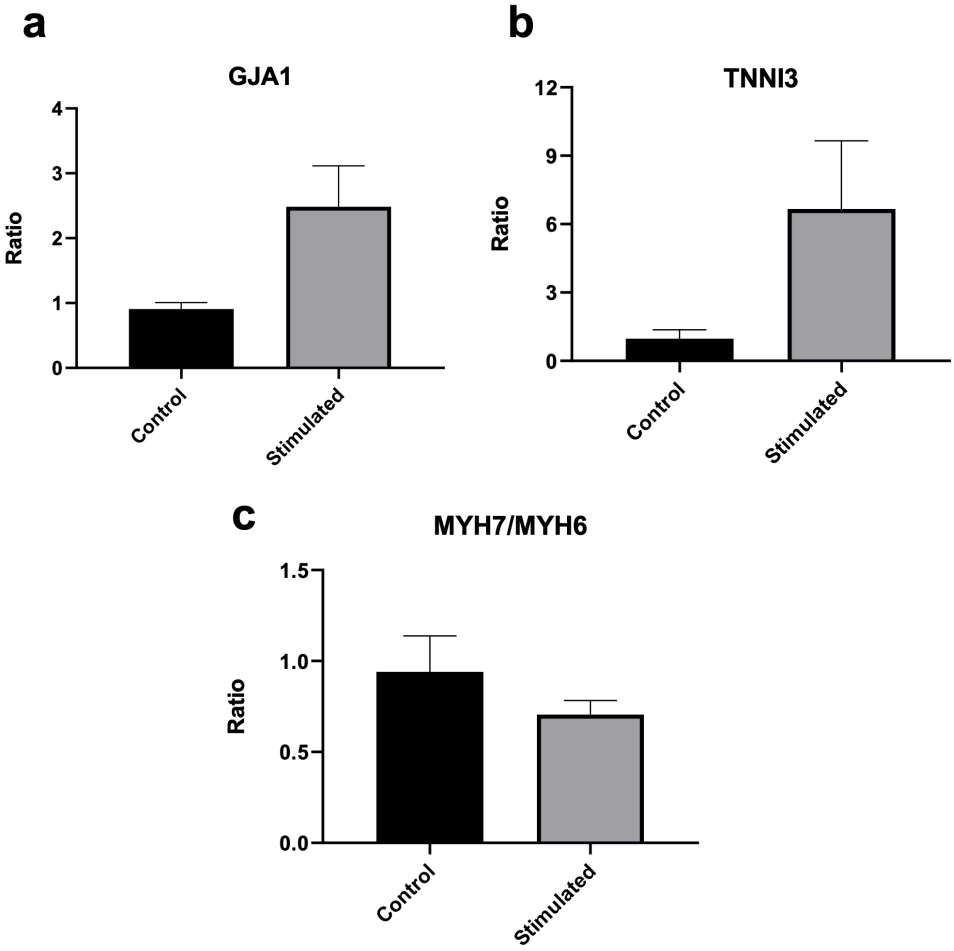

Figure 22 RT-qPCR analysis of the transcriptional expression of different cardiac markers. (**a**) Connexin-43 (encoded by GJA1 gene), **(b)** Troponin I (encoded by TNNI3 gene) and **(c)** ratio between myosin heavy chain alfa and beta isoforms (encoded by the MYH7 and MYH6 genes respectively). Gene expression values are computed as fold changes using the ΔCt method and expressed as a ratio concerning the control condition.

4.4 Conclusions

In this study, we present a microfluidic cell culture system able to generate a highly biomimetic 2D cardiac tissue by incorporating topographical and electrical cues more simply and efficiently than previously reported platforms, representing a useful tool for tissue engineering community. We describe a method to generate electrospun-coated substrates in closed microdevices and validate its potential to consistently yield highly anisotropic cardiac microtissues. Moreover, we

describe a simple and cost-effective strategy to place electrodes in a microfluidic system. An experimentally validated finite element model of our device shows that this approach is able to generate electrical fields with a magnitude comparable to the golden standard based on planar electrodes with similar input voltages. The functionality of the electrical setup for the maturation of the cardiac constructs is also evidenced by the upregulation of key cardiac genes related to the contractile apparatus (troponin I) and conductive properties (upregulation of tight junctional protein Cx-43 at both gene and protein level). Nevertheless, some limitations related to the high stiffness of the 2D substrate are also observed, which leads to a slight decrease in the ratio of β-MHC/α-MHC ratio, often related to a more immature phenotype. Further work is therefore required to address this issue by implementing more compliant substrates that allow a higher degree of remodeling.

4.5 References

[1] Paloschi V, Sabater-Lleal M, Middelkamp H, Vivas A, Johansson S, van der Meer A, Tenje M and Maegdefessel L 2021 Organ-on-a-chip technology: a novel approach to investigate cardiovascular diseases *Cardiovasc. Res.* **117** 2742-54.

[2] Zhao Y, Rafatian N, Wang E Y, Wu Q, Lai B F L, Lu R X, Savoji H and Radisic M 2020 Towards chamber specific heart-on-a-chip for drug testing applications *Adv. Drug Deliv. Rev.* **165–166** 60–76.

[3] Eder A, Vollert I, Hansen A and Eschenhagen T 2016 Human engineered heart tissue as a model system for drug testing *Adv. Drug Deliv. Rev.* **96** 214–24.

[4] Stein J M, Mummery C L and Bellin M 2020 Engineered models of the human heart: directions and challenges *Stem Cell Reports* **16** 2049-57.

[5] Yang X, Pabon L and Murry C E 2014 Engineering adolescence: Maturation of human pluripotent stem cell-derived cardiomyocytes *Circ. Res.* **114** 511–23.

[6] Wilbur J L, Kumar A, Kim E and Whitesides G M 1994 Microfabrication by microcontact printing of self-assembled monolayers *Adv. Mater.* **6** 600–4.

[7] Bursac N, Parker K K, Iravanian S and Tung L 2002 Cardiomyocyte cultures with controlled macroscopic anisotropy: a model for functional electrophysiological studies of cardiac muscle. *Circ. Res.* **91** 45–54.

[8] Karp J M, Yeo Y, Geng W, Cannizarro C, Yan K, Kohane D S, Vunjak-Novakovic G, Langer R S and Radisic M 2006 A photolithographic method to create cellular micropatterns *Biomaterials* **27** 4755–64.

[9] Khademhosseini A, Eng G, Yeh J, Kucharczyk P A, Langer R, Vunjak-Novakovic G and

Radisic M 2007 Microfluidic patterning for fabrication of contractile cardiac organoids *Biomed. Microdevices* **9** 149–57.

[10] Au H T H, Cheng I, Chowdhury M F and Radisic M 2007 Interactive effects of surface topography and pulsatile electrical field stimulation on orientation and elongation of fibroblasts and cardiomyocytes *Biomaterials* **28** 4277–93.

[11] Heidi Au H T, Cui B, Chu Z E, Veres T and Radisic M 2009 Cell culture chips for simultaneous application of topographical and electrical cues enhance phenotype of cardiomyocytes *Lab Chip* **9** 564–75.

[12] Jung G, Fajardo G, Ribeiro A J S, Kooiker K B, Coronado M, Zhao M, Hu D Q, Reddy S, Kodo K, Sriram K, Insel P A, Wu J C, Pruitt B L and Bernstein D 2016 Time-dependent evolution of functional vs. remodeling signaling in induced pluripotent stem cell-derived cardiomyocytes and induced maturation with biomechanical stimulation *FASEB J.* **30** 1464–79.

[13] Salick M R, Napiwocki B N, Sha J, Knight G T, Chindhy S A, Kamp T J, Ashton R S and Crone W C 2014 Micropattern width dependent sarcomere development in human ESC-derived cardiomyocytes *Biomaterials* **35** 4454–64.

[14] Mittal R, Woo F W, Castro C S, Cohen M A, Karanxha J, Mittal J, Chhibber T and Jhaveri V M 2019 Organ-on-chip models: implications in drug discovery and clinical applications *J. Cell. Physiol.* **234** 8352–80.

[15] Parker K and Ingber D 2007 Extracellular matrix, mechanotransduction and structural hierarchies in heart tissue engineering *Philos. Trans. R. Soc. Lond. B. Biol. Sci.* **362** 1267–79.

[16] Mosterd A and Hoes A W 2007 Clinical epidemiology of heart failure *Heart* **93** 1137–46.

[17] Eschenhagen T, Fink C, Remmers U, Scholz H, Wattchow J, Weil J, Zimmermann W, Dohmen H H, Schafer H, Bishopric N, Wakatsuki T and Elson E L 1997 Three-dimensional reconstitution of embryonic cardiomyocytes in a collagen matrix: a new heart muscle model system *FASEB J.* **11** 683–94.

[18] Zimmermann W H, Schneiderbanger K, Schubert P, Didie M, Munzel F, Heubach J F, Kostin S, Neuhuber W L and Enschenhagen T 2002 Tissue engineering of a differentiated cardiac muscle construct *Circ. Res.* **90** 223–30.

[19] Schroer A K, Shotwell M S, Sidorov V Y, Wikswo J P and Merryman W D 2017 I-Wire heart-on-a-chip II: biomechanical analysis of contractile, three-dimensional cardiomyocyte tissue constructs *Acta Biomater.* **48** 79–87.

[20] Xiao Y, Zhang B, Liu H, Miklas J W, Gagliardi M, Pahnke A, Thavandiran N, Sun Y, Simmons C, Keller G and Radisic M 2014 Microfabricated perfusable cardiac biowire: a platform that mimics native cardiac bundle *Lab Chip* **14** 869–82.

[21] Zhao Y, Rafatian N, Feric N T, Cox B J, Aschar-Sobbi R, Wang E Y, Aggarwal P, Zhang B, Conant G, Ronaldson-Bouchard K, Pahnke A, Protze S, Lee J H, Davenport Huyer L, Jekic D, Wickeler A, Naguib H E, Keller G M, Vunjak-Novakovic G, Broeckel U, Backx P H, Radisic M 2019 A platform for generation of chamber-specific cardiac tissues and disease modeling *Cell* **176** 913–27.

[22] Lind J U, Busbee T A, Valentine A D, Pasqualini F S, Yuan H, Yadid M, Park S J, Kotikian A, Nesmith A P, Campbell P H, Vlassak J J, Lewis J A, Parker 2017 Instrumented cardiac microphysiological devices via multimaterial three-dimensional printing *Nat. Mater.* **16** 303–8.

[23] Hu D, Linders A, Yamak A, Correia C, Kijlstra J D, Garakani A, Xiao L, Milan D J, Meer P van der, Serra M, Alves P M and Domian I J 2018 Metabolic maturation of human pluripotent stem cell-derived cardiomyocytes by inhibition of HIF-1α and LDHA *Circ. Res.* **123** 1066–79.

[24] Angst B D, Khan L U, Severs N J, Whitely K, Rothery S, Thompson R P, Magee A I and Gourdie R G 1997 Dissociated spatial patterning of gap junctions and cell adhesion junctions during postnatal differentiation of ventricular myocardium *Circ. Res.* **80** 88–94.

[25] Ribeiro M C, Tertoolen L G, Guadix J A, Bellin M, Kosmidis G, D'Aniello C, Monshouwer-Kloots J, Goumans M J, Wang Y L, Feinberg A W, Mummery C L and Passier R 2015 Functional maturation of human pluripotent stem cell derived cardiomyocytes in vitro-correlation between contraction force and electrophysiology *Biomaterials* **51** 138–50.

[26] Mulieri L A, Hasenfuss G, Leavitt B, Allen P D and Alpert N R 1992 Altered myocardial force-frequency relation in human heart failure *Circulation* **85** 1743–50.

[27] Navaratnam V 1988 Heart muscle: ultrastructural studies *J. Anat.* **158** 77-90.

[28] Lundy S D, Zhu W-Z, Regnier M and Laflamme M A 2013 Structural and functional maturation of cardiomyocytes derived from human pluripotent stem cells *Stem Cells Dev.* **22** 1991-2002.

[29] Jackman C P, Carlson A L and Bursac N 2016 Dynamic culture yields engineered myocardium with near-adult functional output Biomaterials 111 66–79.

[30] Kensah G, Gruh I, Viering J, Schumann H, Dahlmann J, Meyer H, Skvorc D, Bar A,

Akhyari P, Heisterkamp A, Haverich A and Martin U 2011 A novel miniaturized multimodal bioreactor for continuous in situ assessment of bioartificial cardiac tissue during stimulation and maturation *Tissue Eng. - Part C Methods* **17** 463–73.

[31] Thavandiran N, Dubois N, Mikryukov A, Masse S, Beca B, Simmons C A, Deshpande V S, McGarry J P, Chen C S, Nanthakumar K, Keller G M, Radisic M and Zandstra P W 2013 Design and formulation of functional pluripotent stem cell-derived cardiac microtissues *Proc. Natl. Acad. Sci. U. S. A.* **110** 4698-707.

[32] Tulloch N L, Muskheli V, Razumova M V., Korte F S, Regnier M, Hauch K D, Pabon L, Reinecke H and Murry C E 2011 Growth of engineered human myocardium with mechanical loading and vascular coculture *Circ. Res.* **109** 47–59.

[33] Miklas J W, Nunes S S, Sofla A, Reis L A, Pahnke A, Xiao Y, Laschinger C and Radisic M 2014 Bioreactor for modulation of cardiac microtissue phenotype by combined static stretch and electrical stimulation *Biofabrication* **6** 113-140.

[34] Ruan J L, Tulloch N L, Razumova M V, Saiget M, Muskheli V, Pabon L, Reinecke H, Regnier M and Murry C E 2016 Mechanical stress conditioning and electrical stimulation promote contractility and force maturation of induced pluripotent stem cell-derived human cardiac tissue *Circulation* **134** 1557–67.

[35] Ronaldson-Bouchard K, Ma S P, Yeager K, Chen T, Song L, Sirabella D, Morikawa K, Teles D, Yazawa M and Vunjak-Novakovic G 2018 Advanced maturation of human cardiac tissue grown from pluripotent stem cells *Nature Protocols* **556** 239–43.

[36] Asp J, Synnergren J, Jonsson M, Dellgren G and Jeppsson A 2012 Comparison of human cardiac gene expression profiles in paired samples of right atrium and left ventricle collected in vivo *Physiol. Genomics* **44** 89–98.

[37] Dobrev D and Wehrens X H 2010 Calmodulin kinase II, sarcoplasmic reticulum Ca2+ leak, and atrial fibrillation *Trends Cardiovasc. Med.* **20** 30–4.

[38] Gintant G, Sager P T and Stockbridge N 2016 Evolution of strategies to improve preclinical cardiac safety testing *Nat. Rev. Drug Discov.* **15** 457–71.

[39] van der Hooft C S, Heeringa J, van Herpen G, Kors J, Kingma J H and Stricker B H 2004 Drug-induced atrial fibrillation *J. Am. Coll. Cardiol.* **44** 2117–24.

[40] Sun N, Yazawa M, Liu J, Han L, Sanchez-Freire V, Abilez O J, Navarrete E G, Hu S, Wang L, Lee A, Pavlovic A, Lin S, Chen R, Hajjar R J, Snyder M P, Dolmetsch R E, Butte M J, Ashley E A, Longaker M T, Robbins R C and Wu J C 2012 Patient-specific induced pluripotent stem cells as a model for familial dilated cardiomyopathy *Sci. Transl. Med.* **4**

130-150.

[41] Chadwick A C and Musunuru K 2017 Genome Editing for the Study of Cardiovascular Diseases *Curr. Cardiol. Rep.* **19** 107-133.

[42] Friedrichs S, Malan D and Sasse P 2013 Modeling long QT syndromes using induced pluripotent stem cells: Current progress and future challenges *Trends Cardiovasc. Med.* **23** 91–8.

[43] Schneider C A, Rasband W S, Eliceiri K W 2012 NIH Image to ImageJ: 25 years of image analysis *Nat. Methods* **9** 671–675.

[44] Sachot N, Castaño O, Oliveira H, Marti-Muñoz J, Roguska A, Amedee J, Lewandowska M, Planell J A, Engel E 2016 A novel hybrid nanofibrous strategy to target progenitor cells for cost-effective: in situ angiogenesis *J. Mater. Chem. B* **4** 6967-78.

[45] Alvarez Z, Mateos-Timoneda M A, Hyrossova P, Castano O, Planell J A, Perales J C, Engel E, Alcantara S 2013 The effect of the composition of PLA films and lactate release on glial and neuronal maturation and the maintenance of the neuronal progenitor niche *Biomaterials* **34** 2221–33.

[46] Sachot N, Mateos-Timoneda M A, Planell J A, Velders A H, Lewandowska M, Engel E, Castaño O 2015 Towards 4th generation biomaterials: a covalent hybrid polymer–ormoglass architecture *Nanoscale* **7** 15349–61.

[47] Maidhof R, Tandon N, Lee E J, Luo J, Duan Y, Yeager K, Konofagou E, Vunjak-Novakovic G 2012 Biomimetic perfusion and electrical stimulation applied in concert improved the assembly of engineered cardiac tissue *J. Tissue Eng. Regen. Med.* **6**.

[48] Ordoño J, Perez-Amodio S, Ball K, Aguirre A, Engel E 2020 Lactate promotes cardiomyocyte dedifferentiation through metabolic reprogramming *BioRxiv*.

[49] Tandon N, Marsano A, Maidhof R, Wan L, Park H, Vunjak-Novakovic G 2011 Optimization of electrical stimulation parameters for cardiac tissue engineering *J. Tissue Eng. Regen. Med.* **5** 115-25.

[50] Tandon N, Cannizzaro C, Chao P H G, Maidhof R, Marsano A, Au H T H, Radisic M, Vunjak-Novakovic G 2009 Electrical stimulation systems for cardiac tissue engineering *Nat. Protoc.* **4** 155–173.

[51] Puspoki Z, Storath M, Sage D, Unser M 2016 Transforms and operators for directional bioimage analysis: A survey *Adv. Anat. Embryol. Cell Biol.* **219** 69–93.

[52] Feinberg A W, Alford P W, Jin H, Ripplinger C M, Werdich A A, Sheehy S P, Grosberg

A, Parker K K 2012 Controlling the contractile strength of engineered cardiac muscle by hierarchal tissue architecture *Biomaterials* **33** 5732–41.

[53] Badie N, Satterwhite L, Bursac N 2009 A method to replicate the microstructure of heart tissue in vitro using DTMRI-based cell micropatterning *Ann. Biomed. Eng.* **37** 2510–21.

[54] Orlova Y, Magome N, Liu L, Chen Y, Agladze K 2011 Electrospun nanofibers as a tool for architecture control in engineered cardiac tissue *Biomaterials* **32** 5615–24.

[55] Zong X, Bien H, Chung C Y, Yin L, Fang D, Hsiao B S, Chu B, Entcheva E 2005 Electrospun fine-textured scaffolds for heart tissue constructs *Biomaterials* **26** 5330–38.

[56] Sachot N, Castano O, Planell J A, Engel E 2015 Optimization of blend parameters for the fabrication of polycaprolactone-silicon based ormoglass nanofibers by electrospinning *J. Biomed. Mater. Res.- Part B Appl. Biomater.* **103** 1287-93.

[57] Oliveira H, Catros S, Boiziau C, Siadous R, Marti-Munoz J, Bareille R, Rey S, Castano O, Planell J A, Amedee J, Engel E 2016 The proangiogenic potential of a novel calcium releasing biomaterial: impact on cell recruitment *Acta Biomater.* **29** 435–445.

[58] Jariashvili K, Madhan B, Brodsky B, Kuchava A, Namicheishvili L, Metreveli N 2012 UV damage of collagen: insights from model collagen peptides *Biopolymers* **97** 189–198.

[59] Radisic M, Park H, Shing H, Consi T, Schoen F J, Langer R, Freed L E, Vunjak-Novakovic G 2004 Functional assembly of engineered myocardium by electrical stimulation of cardiac myocytes cultured on scaffolds *Proc. Natl. Acad. Sci.* **101** 18129–34.

[60] Tandon N, Marsano A, Maidhof R, Numata K, Montouri-Sorrentino C, Cannizzaro C, Voldman J, Vunjak-Novakovic G 2010 Surface-patterned electrode bioreactor for electrical stimulation *Lab Chip.* **10** 692–700.

[61] Tung L, Sliz N, Mulligan M R 1991 Influence of electrical axis of stimulation on excitation of cardiac muscle cells *Circ. Res.* **69** 722–730.

[62] Visone R, Talo G, Occhetta P, Cruz-Moreira D, Lopa S, Pappalardo O A, Redaelli, Moretti A, Rasponi M 2018 A microscale biomimetic platform for generation and electro-mechanical stimulation of 3D cardiac microtissues *APL Bioeng.* **2** 46-102.

[63] Hsiao C W, Bai M Y, Chang Y, Chung M F, Lee T Y, Wu C T, Maiti B, Liao Z X, Li R K, Sung H W 2013 Electrical coupling of isolated cardiomyocyte clusters grown on aligned conductive nanofibrous meshes for their synchronized beating *Biomaterials* **34** 1063–72.

[64] Bhana B, Iyer R K, Chen W L K, Zhao R, Sider K L, Likhitpanichkul M, Simmons C A, Radisic M 2010 Influence of substrate stiffness on the phenotype of heart cells *Biotechnol.*

Bioeng. **105** 1148–60.

[65] Radisic M, Park H, Martens T P, Salazar-Lazaro J E, Geng W, Wang Y, Langer R, Freed L E, Vunjak-Novakovic G 2008 Pre-treatment of synthetic elastomeric scaffolds by cardiac fibroblasts improves engineered heart tissue *J. Biomed. Mater. Res. - Part A.* **86** 713–724.

[66] Naito H, Melnychenko I, Didie M, Schneiderbanger K, Schubert P, Rosenkranz S, Eschenhagen T, Zimmermann W H 2006 Optimizing engineered heart tissue for therapeutic applications as surrogate heart muscle *Circulation* **114** 72-78.

[67] Tandon N, Cannizzaro C, Figallo E, Voldman J, Vunjak-Novakovic G 2006 Characterization of electrical stimulation electrodes for cardiac tissue engineering *Annu. Int. Conf. IEEE Eng. Med. Biol. Proc.* 845–848.

[68] Rubinstein J T, Miller C A, Mino H, Abbas P J 2001 Analysis of monophasic and biphasic electrical stimulation of nerve *IEEE Trans. Biomed. Eng.* **48** 1065–70.

[69] Han J, Wu Q, Xia Y, Wagner M B, Xu C 2016 Cell alignment induced by anisotropic electrospun fibrous scaffolds alone has limited effect on cardiomyocyte maturation *Stem Cell Res.* **16** 740–750.

[70] Feric N T, Radisic M 2016 Towards adult-like human engineered cardiac tissue: maturing human pluripotent stem cell-derived cardiomyocytes in human engineered cardiac tissues *Adv Drug Deliv Rev.* **96** 110–134.

[71] Smyth J W, Hong T T, Gao D, Vogan J M, Jensen B C, Fong T S, Simpson P C, Stainier D Y R, Chi N C, Shaw R M 2010 Limited forward trafficking of connexin 43 reduces cell-cell coupling in stressed human and mouse myocardium *J. Clin. Invest.* **120** 266–279.

[72] Chiu L L Y, Iyer R K, King J P, Radisic M 2011 Biphasic electrical field stimulation aids in tissue engineering of multicell-type cardiac organoids *Tissue Eng. - Part A.* **17** 1465–1475.

[73] Jones J L, Jones R E, Balasky G Improved cardiac cell excitation with symmetrical biphasic defibrillator waveforms 1987 *Am. J. Physiol.* **253** 1418-24.

[74] Visone R, Talo G, Lopa S, Rasponi M, Moretti M 2018 Enhancing all-in-one bioreactors by combining interstitial perfusion, electrical stimulation, on-line monitoring and testing within a single chamber for cardiac constructs *Sci. Rep.* **8** 1–13.

[75] Xiu Q X, Set Y S, Sun W, Zweigerdt R 2009 Global expression profile of highly enriched cardiomyocytes derived from human embryonic stem cells *Stem Cells* **27** 2163–2174.

[76] McDermott P, Daood M, Klein I 1985 Contraction regulates myosin synthesis and myosin

content of cultured heart cells *Am. J. Physiol. - Hear. Circ. Physiol.* **18** 63-69.

[77] Ivester C T, Tuxworth W J, Cooper G, McDermott P J 1995 Contraction accelerates myosin heavy chain synthesis rates in adult cardiocytes by an increase in the rate of translational initiation *J. Biol. Chem.* **270** 21950–57.

[78] Sharp W W, Terracio L, Borg T K, Samarel A M 1993 Contractile activity modulates actin synthesis and turnover in cultured neonatal rat heart cells *Circ. Res.* **73** 172–183.

5

Development of a 3D Human-derived Model of Cardiac Ischemia-Reperfusion Injury

Ischemic heart disease, also known as myocardial infarction (MI) is the most prevalent cardiac disease, accounting for more than 30 % of all global deaths. Despite the devastating consequences of this disease, current clinical treatments are highly limited, mainly due to the lack of adequate preclinical models to investigate cardioprotective or regenerative strategies. Most of these models are based on animal experiments, which have been widely recognized to fail in reliably predicting the actual human response. In this chapter, we start by introducing the current state of the art in preclinical models for myocardial infarction to then describe our proposal to model *in vitro* a cardiac ischemia-reperfusion injury (IRI) using a novel microfluidic device architecture to co-culture human pluripotent stem-cell derived cardiomyocytes (hPSC-CM) and primary human cardiac fibroblasts (hCF) in 3D. The devices were assembled by bonding polydimethylsiloxane (PDMS) replicates obtained from micromilled polymethyl methacrylate (PMMA) master moulds to ultra-thin glass coverslips. A preliminary screening using 2D hPSC-CM monolayers is presented to investigate the media composition and cycle of oxygen tension conditions that generate pathological levels of necrotic and apoptotic cell death. These conditions were then validated in the 3D cardiac tissues obtained in the microfluidic platform, showing a significant increase in both mechanisms of cell death. The response of cardiac fibroblasts to IRI was also investigated in both 2D and 3D assays, showing a significant increase in the expression of α-smooth muscle actin and collagen I deposition, two hallmark markers of the fibrotic response. Overall, these results show that the presented platform can be of great interest to enhance cardiovascular and regenerative medicine research.

5.1 Introduction to preclinical models for myocardial infarction

The process of cardiac damage in MI generally occurs in two steps: the first one is ischemia, which occurs when a plaque blocks a coronary artery, occluding the blood flow to the heart tissue, which prevents nutrients and oxygen from reaching cardiac cells and the accumulation of metabolic by-products [1]. Oxygen depletion switches CM metabolism from aerobic respiration to anaerobic glycolysis, a far less efficient method of producing adenosine triphosphate (ATP), which translates into an increase in ATP hydrolysis and therefore intracellular acidification [2]. Glycolysis also increases lactate production and the extrusion of protons through the lactate-proton cotransporter to balance the intracellular pH [3]. However, the lack of blood flow leads to an increase in metabolic products such as lactate, which prevents the correct outflux of this metabolite and increases intracellular acidosis [4]. To try to find alternative ways to compensate for the decrease in pH, CMs start using the sodium-hydrogen channels to pump protons out and increase sodium levels [5]. Nevertheless, the lack of ATP hampers sodium release, which makes this ionic channel function in reverse, which translates into higher calcium concentrations in the cytosol [6].

The second step in MI is reperfusion, which occurs when the coronary artery is unblocked by a therapeutic intervention such as thrombolytic drugs or percutaneous coronary intervention [1]. This can help recover the ischemic region by restoring the extracellular pH, but also results in an increase in cell death due to the drastic activation of the sodium-hydrogen channels, which starts pumping protons leading to a further accumulation of calcium [7]. This increases the production of reactive oxygen species (ROS), mitochondrial membrane permeability which leads to the failing of the electron transport chain, ATP production and eventually membrane rupture, which results in the release of apoptotic proteins to the cytosol [8]. These damage-associated proteins trigger the recruitment of immune cells to the infarcted region, which clears the dead cells and ECM debris and initiates a regenerative response [9]. This involves the recruitment of cardiac fibroblasts as well as their activation towards myofibroblasts, which are in charge of depositing ECM proteins (mostly collagen) to cover the injured region; and the triggering of neovascularization [10] (see **Fig.23-a**). When the fibrotic scar is completely formed, fibroblasts go back to their quiescent state and the neo vessels get surrounded by mural cells and transform into mature vessels [11].

Current preclinical models to study ischemia-reperfusion injury (IRI) primarily rely on animal models to test new therapeutic approaches. Nevertheless, some in vitro assays exist, which are based on the use of isolated CM, allowing for the direct control and manipulation of the various factors contributing to the IRI, which makes it easier to understand disease mechanisms and how therapeutic candidates may work. There is no standard protocol to study IRI *in vitro*, so the cell

source must be carefully considered [12]. Neonatal mouse CMs are the most widely used, due to the relatively easy isolation process and mid- to long-term viability in culture [13]. The main concern with their use is that they are more resistant to hypoxia than adult CM, which limits the translational potential of these studies [14]. Unfortunately, the isolation procedure for adult mouse CM is far more challenging and their viability after the extraction is highly limited [15]. This led to an increased interest in alternative models such as cell lines (H9C2 or HL-1) [16]. However, these cells fail in recapitulating the actual cardiac phenotype, as they are proliferative and have different apoptotic and bioenergetic pathways [17]. Alternative options include progenitor cells [18] or induced pluripotent stem cell-derived CM (iPSC-CM) [19,20], which are probably the most attractive model, as they have a human origin. Despite their promising potential, few studies have been carried out with these cells, and some concerns have arisen regarding their unmatured nature and non-physiologic responses [21].

To mimic the ischemic event, the most common approach is to use a dedicated incubator to replicate anoxic conditions (less than 1 % O_2, 5 % CO_2 and around 94 % N_2) and use a serum-free, glucose-free medium [1]. Additional modifications in cell media composition can be performed to mimic other physiological conditions such as hyperkalemia or acidosis [22]. The duration of hypoxia and reoxygenation also have to be carefully considered, as longer times than in vivo are required due to the different levels of maturity and oxygen dependency [23]. For animal experiments, 30 min is generally enough to elicit the ischemic response, but in vitro time intervals ranging from 90 min to 9 h have to be considered [24]. The most common variables measured in the in vitro models to assess the role of a certain therapeutic in increasing or protecting cells from IRI include cell viability, which is evaluated using methods such as LDH or propidium iodide to quantify cell survival and annexin V immunostaining to quantify apoptosis; mitochondrial membrane damage using tetramethyl-rhodamine methyl ester (TMRM) immunostaining and ROS production [20,25].

An alternative in vitro assay is the use of isolated perfused hearts, in which the heart of the animal (generally mice) is removed and infused with a physiological saline solution (generally a Krebs-Henseleit buffer) [26,27]. The most common technique to work with isolated hearts is the Langerdoff system, in which the heart is perfused through the coronary arteries with the saline solution, maintaining its viability for several hours [28]. Left-ventricular (LV) pressure is monitored to measure cardiac function in real-time. The injury can be then generated by completely stopping the perfusion (global ischemia) or performing a suture in a coronary artery (regional ischemia) during 20-40 min [29]. This method allows the evaluation of different parameters of the cardiac injury, such as contractile dysfunction using the LV-pressure sensor, cell death and infarct size using a triphenyltetrazolium chloride (TTC) staining or intracellular pH

monitoring using NMR spectroscopy [30]. Some of the disadvantages of this model is the possibility of generating a tissue edema, its limited stability or an excessive coronary flow, which may be not representative of the actual *in vivo* environment [12].

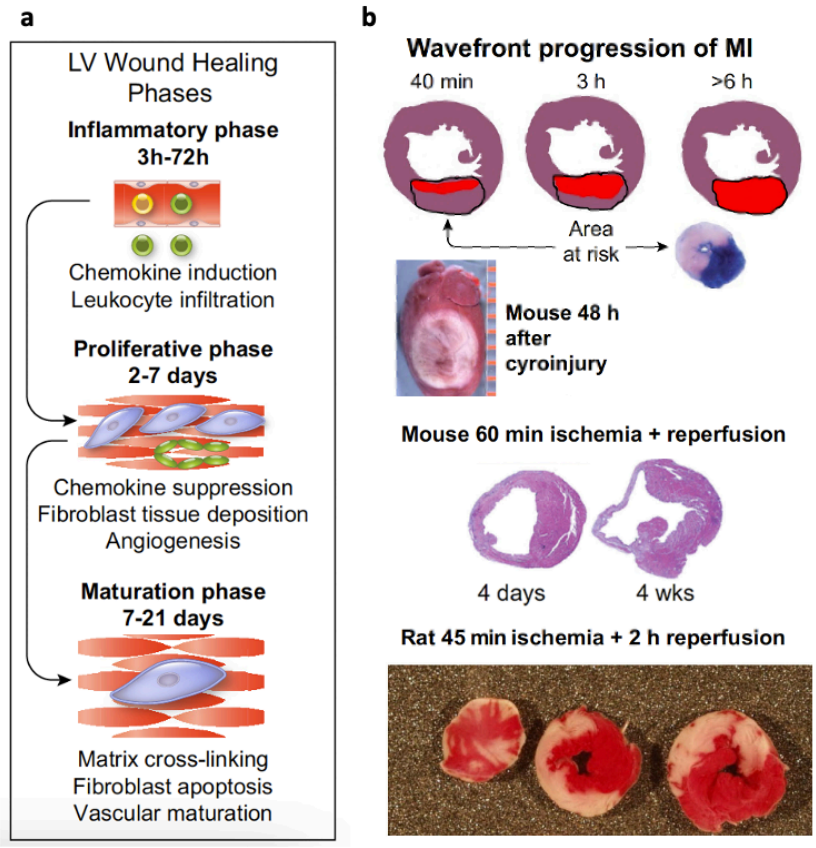

Figure 23 Myocardial infarction progression. (a) Different phases of the regeneration after an ischemia-reperfusion injury, including the inflammatory response, regenerative/proliferative stage and eventual maturation. **(b)** Progression of the ischemic injury in murine *in vivo* models with time. *Adapted from [12].*

Although *in vitro* models provide a simplified framework to study heart ischemia and identify new therapeutic targets, results are many times not predictive of the actual clinical response due to the simplistic approach, as, for instance, many of the CM interactions with non-cardiac cells (macrophages, endothelial cells, fibroblasts, etc.) are not accounted for, which have been demonstrated to have a huge impact in the actual heart microenvironment [31]. Therefore, *in vivo* assays are critical to validate any potential therapy. These studies consist in performing a suture to occlude the left descending coronary artery of the animal [17]. The occlusion can be permanent, to mimic patients that due to logistic issues con not receive successful reperfusion [32], or temporal (generally removed after 45-60 min), to model the growing population of patients that survive the event by being at risk of further complications due to the complications derived from heart remodelling [33,34]. This procedure is most commonly performed in rodent models [35,36] due to their lower costs compared to larger animal models (see **Fig.23-b**), although they are

considered a closer approximation to the clinical situation, especially in pigs as their heart rate and size is comparable to humans [37].

Results of MI are usually evaluated at two different time points: a first one during the first week to assess CM death and infarct size, inflammation, fibroblast activation and ECM deposition as well as neovascularization; and a second one during the 4-8 weeks post-infarction to gather information about long-term heart remodelling [38-40]. Several techniques are used to study cardiac tissue healing and remodelling: imaging techniques such as echocardiography or magnetic resonance (MRI) are used to obtain information about infarct size and geometry [41,42]. Histochemistry stainings are also used to characterize the response to MI: haematoxylin/eosin serves to identify areas of necrosis and inflammation, picrosirius red staining to characterize collagen deposition and other specific immunostainings (neutrophils, macrophages, fibroblasts, endothelial cells, etc.) are useful to evaluate vascularization, fibrosis and further aspects of inflammation [43].

Despite their many advantages in the analysis of MI, animal models have demonstrated limited success in translating therapeutic approaches to the clinic, due to their inherent differences from the human species [1]. For instance, rodents have a higher heart rates and basal metabolism as well as different electrophysiological profiles [44,45]. On top of that, the procedures are technically challenging and highly costly, which among other things reduce the statistical significance of the studies [12]. This is why in this chapter we report the development of a novel microfluidic platform to model IRI in a 3D human-derived tissue model and characterize both the cell death and fibrotic response. To achieve that, we present a novel microfluidic platform based on micropost technology for the formation of engineered heart tissues by the self-assembling of a suspension of human induced pluripotent stem cell-derived cardiomyocytes (hiPS-CM) with primary human cardiac fibroblasts (hCF). To obtain the platform, master moulds were designed and fabricated by milling polymethyl methacrylate (PMMA) substrates and PDMS replicates were generated from it and bonded to ultra-thin glass substrates. The devices were then used to investigate the optimal conditions to mimic an IRI in terms of media composition and cycle of oxygen tensions that maximize cell death (necrosis and apoptosis) and fibrosis both in 2D and 3D.

5.2 Materials and methods

5.2.1 Cell differentiation

The cardiomyocytes used in this work were obtained using a previously reported protocol [46]. Briefly, human pluripotent stem cells (hPSC) were seeded at a density of $25*10^3$ cells/cm^2 on Matrigel-coated 6-well plates in essential 8 medium (Thermo Fisher, US) on day -1. On day 0,

mesodermal differentiation was initiated by adding the Wnt activator CHIR99021 (1.5 µmol/l, Axon Medchem, US), Activin-A (20 ng/ml, Miltenyi, DE) and BMP4 (20 ng/ml, R&D Systems, US) in BPEL media. On day 3, Wnt is inactivated by adding XAV939 (5umol/l, R&D Systems, US) in BPEL. In all cases, Matrigel is added to the media (1:200) to facilitate cell adhesion. Cell cultures were refreshed on day 7 and 10 with BPEL. For most of the experiments, we used a double reporter line expressing green fluorescent protein (GFP) for NKX2.5 and mRubyII for ACTN2 gene (which encodes α-sarcomeric actinin). This dual reporter line was obtained using CRISPR-Cas9 mediated genome editing as previously reported [47], and from now on will be referred to as DRRAGN (Double Reporter of mRubyII-ACTN2 and GFP-NKX2.5).

5.2.2 Cell culture in 2D

To perform the ischemia-reperfusion experiments in 2D, the hPSC-CM were thawed and seeded in 96-well plates previously coated with 50 µl of vitronectin with Geltrex (ThermoFisher, US), both at 1:100 in Dulbecco's phosphate buffered saline solution (DPBS) for 1 h at 25 °C. After that, plates were incubated for additional 30 min at 37 °C with media composed of 87 % Dulbecco's Modified Eagle Medium/Nutrient Mixture F-12 (DMEM/F-12), 10 % fetal calf serum (FCS), 1 % GlutaMax supplement, 1 % penicillin/streptomycin, and 1 % of non-essential amino acids (all from ThermoFisher, US). Finally, cardiomyocytes were seeded at a density of $1.25*10^5$ cells/cm^2 per well and cultured in 150 µl of basal media, composed of maturation medium [46] with TDI: T3 hormone concentration of 100 nM, 100 ng ml^{-1} of IGF-1 (both from Sigma, DE) and 1 µM of dexamethasone (Tocris, UK). This media was also fully supplemented with D-glucose at 4.5 mM and sodium lactate at a concentration of 5 mM (both from Sigma, DE). Cells were kept in culture in an incubator with the environmental conditions set at 21 % O_2, 37 °C and 5 % CO_2 for 7 days with changes of media every 2 days to let them recover and reach confluence.

5.2.3 Design and fabrication of the microfluidic platform

The microfluidic platform design (see **Fig.24-a,b**) was obtained using computer-aided design software (SolidWorks 2020, Dassault Systèmes, FR) and consists of 4 cell culture chambers (6 mm x 1 mm x 1 mm) flanked by 2 culture media channels (1 mm x 1 mm). Each chamber has 2 hanging posts of 0.2 mm in diameter, height of 0.95 mm and separated 3 mm between them. Master molds were produced from a polymethylmethacrylate (PMMA) block using a micromilling machine (Datron Neo, Datron, DE). The input files for the milling machine were produced using computer-aided manufacturing software (HSM Works, Autodesk, US). Replicates in PDMS were obtained, cleaned, bonded and sterilized following the procedures previously described in section 3.2.2 (holes of 1 mm were used for the media channels).

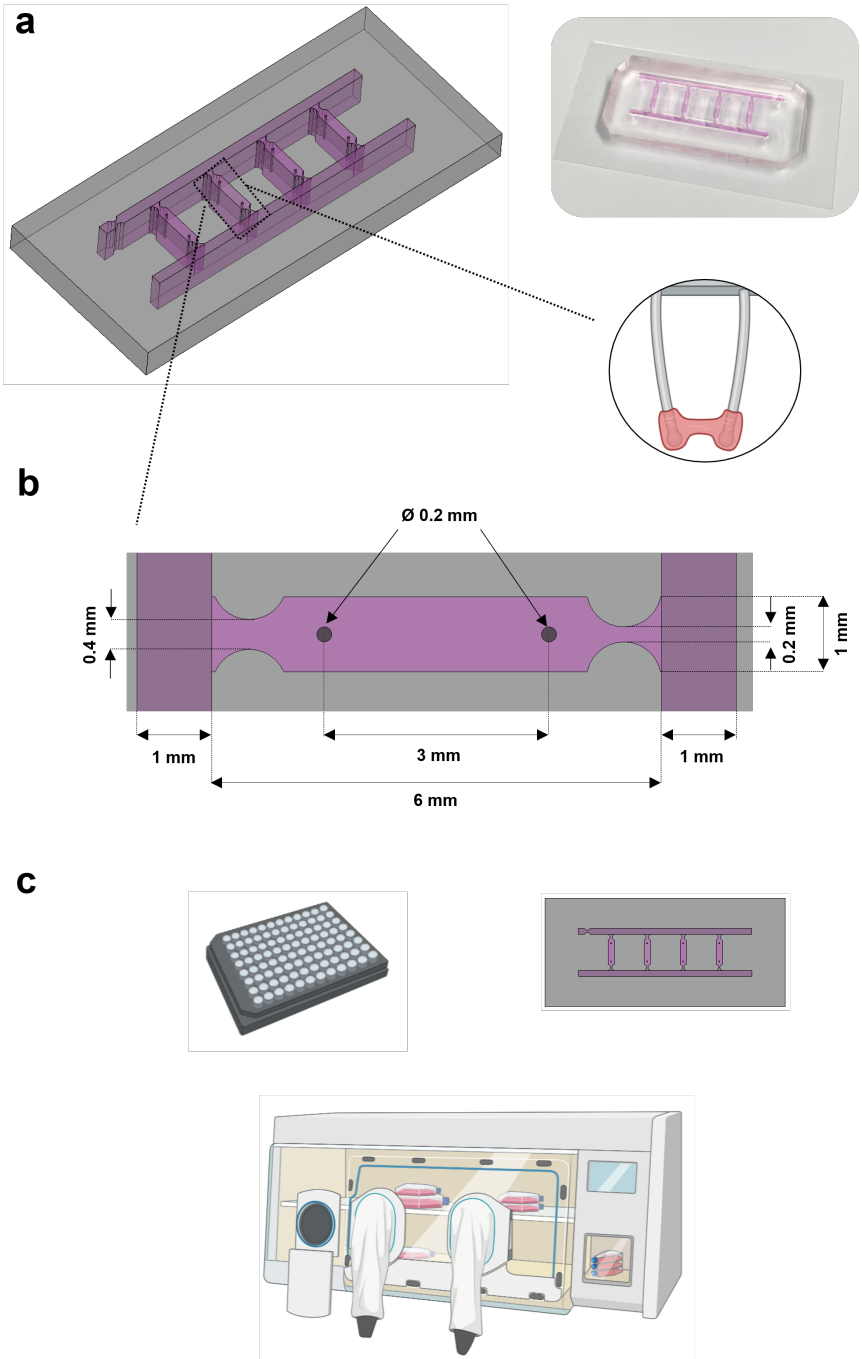

Figure 24 Design and cell culture conditions for the microfluidic platform aimed at generating the cardiac IRI. (**a**) Schematic representation of the microfluidic device with a detail of how the cardiac tissues assemble around the micropost structures and a photo of the actual device. (**b**) Detailed view of the microfluidic device including all the dimensions for the cell chamber, media channels and micropost structures. (**c**) Representation of the elements required to perform the ischemia-reperfusion experiments, including the 2D (96 well plates) and 3D (microfluidic device) platforms as well as the hypoxia workstation used to control the oxygen tensions.

5.2.4 Cell culture in 3D

To obtain the engineered cardiac tissues in 3D, the hPSC-CM were co-cultured inside the microfluidic platform with commercial human adult primary cardiac fibroblasts (hCF, Promocell

C-12375). To do so, both cell types were thawed, counted and mixed in a proportion of $5*10^5$ hPSC-cardiomyocytes to $5*10^4$ hCF. Cells were then resuspended in 48 µl of the fully supplemented media and mixed with 6 µl of Matrigel (ThermoFisher, US, concentration batch dependent), 6 µl of fibrinogen and 0.6 µl of thrombin (both from Sigma, DE) with a stock concentration of 20 mg/ml and 100 U/ml respectively in a solution of bovine serum albumin (BSA) at 0.1 % w/v in PBS. All procedures were carried out on ice to avoid the premature gelation of the hydrogel. The 60 µl of cell suspension was then injected into the upper channel of the microfluidic chip. Due to the restriction imposed by the capillary burst valve located at the end of the channel (section narrowing to 0.2 mm), it starts to progressively enter each of the 4 cell chambers. The same principle is applied to confine the cell suspension in the chambers (outlet section narrowing of 0.2 mm) and to retain the suspension when it is aspirated back in order to remove it from the upper channel (inlet section narrowing to 0.4 mm). Once all the cell chambers are loaded, the chips are incubated for 15 min at 25 ˚C to allow for the pre-polymerization of the gel and the start of cell compaction. After that time the channels are hydrated by placing two pipette tips with a filter on the two inlets of one side with 45 µl each and the other two on the other side with 150 µl each. Finally, the chips are placed in a rocket plate in the incubator (21 % O_2, 37 °C and 5 % CO_2) for 7 days to establish a flow driven by the pressure differences between the reservoirs. Media changes were performed every 2 days.

5.2.5 Ischemia-reperfusion experiments

Ischemia-reperfusion experiments started at day 8, in which three environmental conditions were considered: normoxia (21 % O_2 tension for 10 h), ischemia (0 % O_2 for 10 h) and ischemia/reperfusion (0 % O_2 for 8 h + 21 % oxygen tension for 2 h with fully supplemented media refreshment). For the latter two conditions, we considered two types of ischemic media: basal media + TDI (without nutrients) and an ischemic media composed of a HEPES solution in distilled water (pH = 6.4) supplemented with 119 mM NaCl, 12 mM KCl, 1.2 mM NaH_2PO_4, 1.3 $MgSO_4$, 0.5 $MgCl_2$, 0.9 $CaCl_2$, 20 mM of sodium lactate to mimic the conditions of the ischemic heart, characterized by hyperkalemia, high lactate concentrations and acidic pH due to metabolic waste accumulation [48,49]. The anoxic conditions were attained by placing the plates or the chips inside a hypoxia workstation (**Fig.24-c**).

5.2.6 Fluorescent staining and cell death quantification

To evaluate necrotic cell death, a live/dead staining was performed using a commercial kit (Thermo Fisher L3224, US). Briefly, after washing with sterile PBS, a solution of calcein at 1:2500 and ethidium homodimer-1 (EthD-1) at 1:500 in DPBS 1X was prepared and samples were incubated for 15 min at 37 ˚C. It is important to highlight that the hPSC-CMs used for live/dead experiments were not modified to express the double reporter line (DRRAGN) to avoid

the overlapping of the α-sarcomeric actinin fluorescent signal with EthD-1. For apoptosis, samples were washed with sterile PBS and then incubated for 15 min at room temperature with a solution of annexin V diluted in the buffer provided with the kit at 1:200 (Thermo Fisher A23204, US). After that, samples were washed with the commercial buffer and a final replacement of culture media was performed before imaging.

Fluorescent images were taken in both cases in an EVOS FL2 microscope (Thermo Fisher, US). A total of 2 pictures at 20x magnification were taken per sample (a total of 3 samples so 6 images per condition), except for the 2D live/dead assay, in which a 10x magnification was used. To obtain a quantitative score for cell death, all images were processed in Image J software [50] to calculate the positive area for each of the stainings. Briefly, this was achieved by converting the images to 8 bit, thresholding them and measuring the positive area covered by the marker of interest. To quantify the relative amount of necrotic cells, the EthD-1 signal area was divided by the calcein positive area, while to check for the number of apoptotic cells, the annexin V positive area was divided by the area covered by the α-sarcomeric actinin staining. In both cases, results for cell death are expressed as fold-changes with respect to the standard culture conditions, which correspond to fully supplemented cell culture media and 21 % O_2.

5.2.7 Immunostaining and evaluation of fibrotic response

To perform the immunostaining, samples were washed 3 times with sterile 1x PBS for 5 min and then fixed incubating with 4 % paraformaldehyde (Electron Microscopy Sciences, US) for 15 minutes in the case of the 2D cultures or 1 h for the 3D tissues. After that, 3 washes with sterile PBS were performed and tissues inside the microfluidic chips were transferred to a 96-well plate by separating the PDMS from the glass substrate and carefully removing with tweezers the cardiac tissues from the pillars. The next step involved the permeabilization of the samples by incubating with a solution of Triton-X-100 (Sigma, DE) at 0.3 % in 1x PBS: the 2D samples were incubated for only 10 min, while the 3D tissues were washed 3 times for 20 min. The samples were then incubated with the blocking solution consisting of bovine serum albumin (BSA from Sigma, DE) at 10 % w/v in 1x PBS to prevent non-specific antibody bindings (2 h for the 2D, overnight for the 3D) at 4 ˚C. Then, samples were incubated with the primary antibody solution consisting of mouse α human smooth muscle actin (αSMA from Sigma A2547, DE) and rabbit α human collagen I (Novus Bio NB600-408, US) both at 1:200 in PBS + BSA (1 % w/v) overnight at 4 ˚C in agitation. After this, samples were incubated with the secondary antibody solution consisting of rabbit α mouse Alexa Fluor 568 (Molecular Probes A11061, US) and goat α rabbit Alexa Fluor 647 (Thermo Fisher A21244, US) at 1:200 in PBS + BSA (1 % w/v) overnight at 4 °C. Finally, a counterstaining for cell nuclei was also performed by incubating DAPI (Thermo Fisher D1306,

US) (1:1000) in 1x PBS for 10 min (2D) or 1 h (3D) at room temperature. Samples were then rinsed three times in 1x PBS and maintained at 4 ºC in the same solution until image acquisition.

Imaging was performed on the EVOS FL2 microscope (Thermo Fisher, US) for the 2D cultures and a Zeiss LSM880 (Carl Zeiss, DE) for the 3D ones. A total of 2 pictures were taken per sample (a total of 3 samples so 6 images per condition) at 20x magnification for the 2D and 40x for the 3D. Protein expression scores were obtained from the acquired images using Image J software. Briefly, αSMA and collagen I images were processed by converting them to an 8-bit format, thresholding and measuring the positive area of each staining. This data was normalized by the number of cells, which was calculated from the DAPI images using the same procedure to threshold the images and then applying the *Analyze Particles* plugin with standard settings. In both cases, results for cell death are expressed as fold-changes with respect to the standard culture conditions, which correspond to fully supplemented cell culture media and 21 % O_2.

5.2.8 Statistical analysis

All data were statistically analyzed following the same procedure as presented in section 3.2.9.

5.3 Results and discussion

5.3.1 The ischemic solution produces a higher degree of cell death than nutrient deprivation alone in hPSC-CM cultures in 2D

To select the best conditions to mimic an ischemia-reperfusion injury in a 3D cardiac tissue, we screened the influence of the main environmental factors involved in causing cardiac cell death in 2D. The first factor to be evaluated was cell culture media composition without changing the environmental oxygen tension (set at normoxic conditions of 21 % O_2). We studied the levels of cell death using either cell culture media without any metabolic substrate (lactate or glucose) or an ischemic solution. We expressed the results as fold change with respect to the regular cell culture conditions with fully supplemented (FS) media (see **Fig.25,26-a,b**). We show that hPSC-CM are minimally affected by nutrient deprivation, with a significant increase in necrotic (1.37 ± 0.27 vs 1.00 ± 0.24) or apoptotic cell death (0.96 ± 0.29 vs 1.00 ± 0.38) after being cultured in basal media for 10 h. We even show (**Fig.27**) that hPSC-CMs remain viable after 3 days in basal media culture without any refreshment, as demonstrated by the minimal changes in the integrity of the α-sarcomeric actinin structures. This resistance to nutrient deprivation is probably due to fetal-like metabolism of the hPSC-CM, which is mainly based on glycolysis instead of oxidative phosphorylation of fatty acids [51]. On top of that, these cells have a much higher capacity for glucose uptake and subsequent glycogen storage than adult cardiomyocytes [52], which could explain how the cells can resist for several days without nutrients by obtaining energy through glycogenolysis.

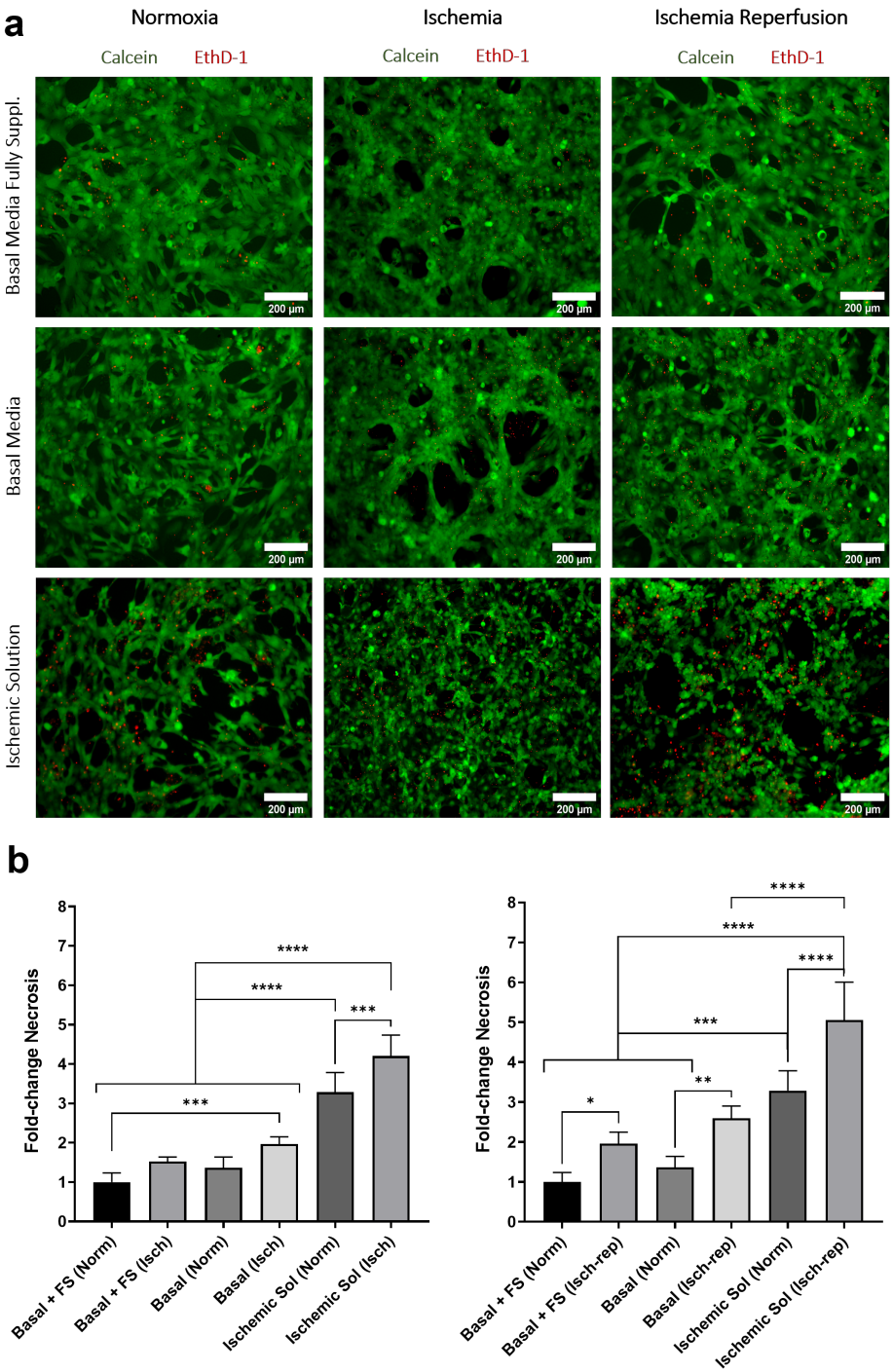

Figure 25 Evaluation of hPSC-CM necrotic cell death in 2D. (**a**) Fluorescent microscope images for a staining with calcein (green signal corresponding to live cells) and ethidium homodimer-1 (red signal corresponding to necrotic cells) of hPSC-CM cultured in 2D. Three different conditions were considered for media formulations (basal cell culture media, fully supplemented cell culture media and ischemic solution) and oxygen tensions (normoxia = 21 % O_2 for 10 h, ischemia = 0 % O_2 for 10 h and ischemia-reperfusion = 0 % O_2 for 8 h + 21 % O_2 for 2 h). Scale bar is 200 µm for all images. (**b**) Quantification of the necrosis levels as a ratio of the ethidium homodimer 1 respect to the calcein positive area. Data is normalized and expressed as fold-change respect to the standard culture conditions, which correspond to fully supplemented cell culture media and normoxia. Results are represented as mean ± standard deviation (n = 6) with *p < 0.05 (evaluated with Student's t-test).

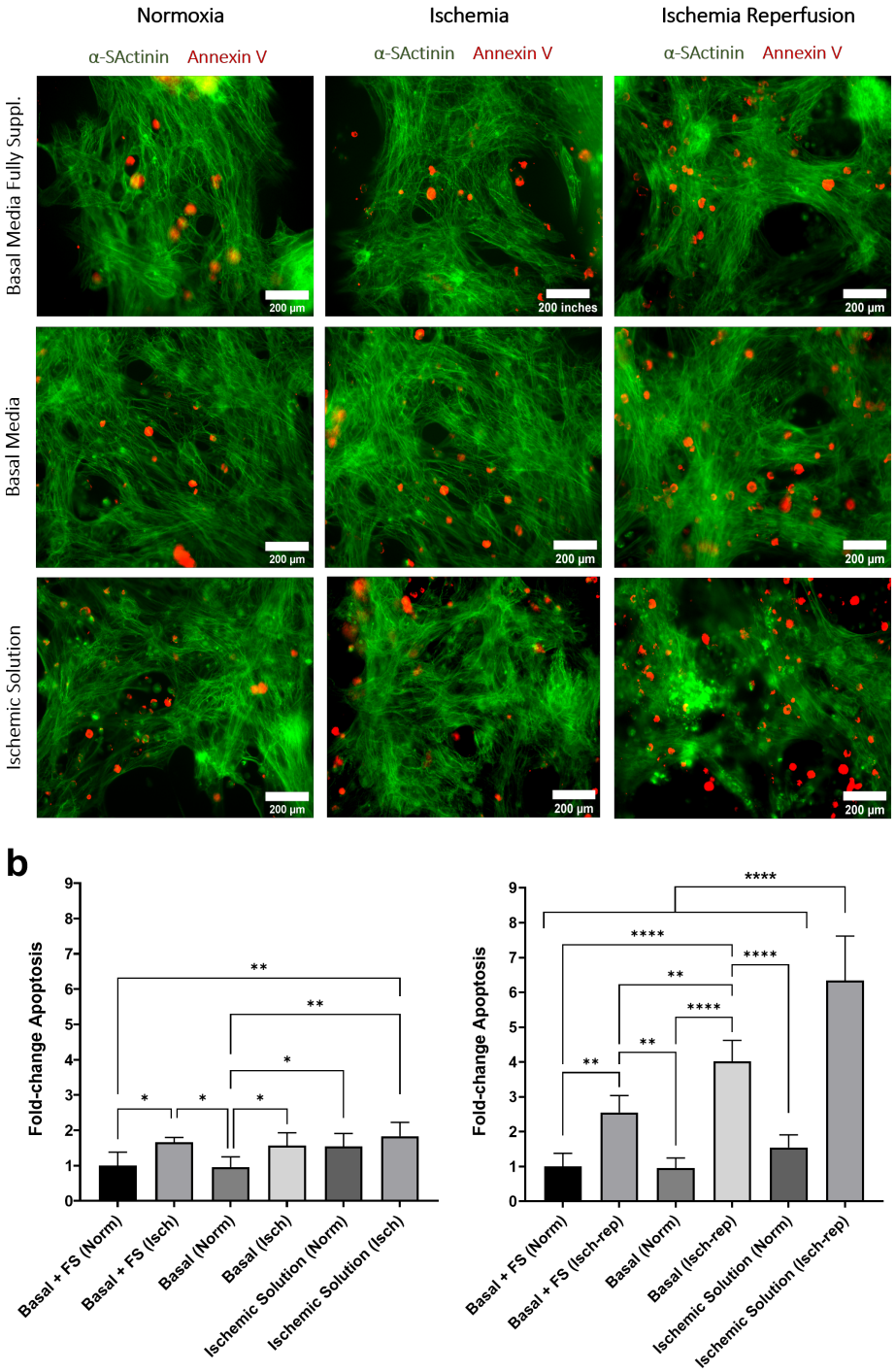

Figure 26 Evaluation of hPSC-CM apoptotic cell death in 2D. (**a**) Fluorescent microscope images for α-sarcomeric actinin protein expressed by the hPSC-CM DRRGN line (green signal) and annexin V staining (red signal corresponding to apoptotic cells) of hPSC-CM cultured in 2D. Three different conditions were considered for media formulations (basal cell culture media, fully supplemented cell culture media and ischemic solution) and oxygen tensions (normoxia = 21 % O_2 for 10 h, ischemia = 0 % O_2 for 10 h and ischemia-reperfusion = 0 % O_2 for 8 h + 21 % O_2 for 2 h). Scale bar is 200 µm for all images. (**b**) Quantification of the apoptosis levels as a ratio of the annexin V with respect to the α-sarcomeric actinin positive area. Data is normalized and expressed as fold-change with respect to the standard culture conditions, which correspond to fully supplemented cell culture media and normoxia. Results are represented as mean ± standard deviation (n = 6) with *p < 0.05 (evaluated with Student's t-test).

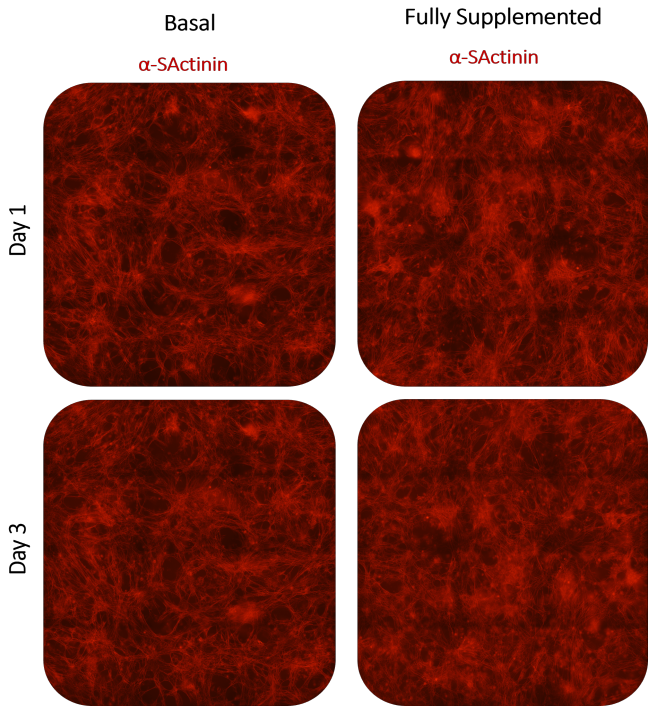

Figure 27 Monitoring of hPSC-CM long term viability (3 days) without media refreshment. Imaging of hPSC-CM (DRRGN line) expressing fluorescent α-sarcomeric actinin on day 1 and 3 in culture in both basal media and fully supplemented basal media without media changes.

In the case of using the ischemic solution, necrotic cell death is increased 3-fold compared to that observed using fully supplemented media (3.29 ± 0.50 vs 1.00 ± 0.24, $p < 0.0001$). Apoptosis is also significantly higher (1.55 ± 0.36 vs 1.00 ± 0.38, $p < 0.05$), but not to the same extent as necrosis. This increase in cell death can be explained because the ischemic solution is able to better recapitulate the microenvironment generated by the quick waste accumulation that occurs *in vivo* [1]. One of the main traits mimicked is the accumulation of lactate that occurs *in vivo* (concentration of 22 mM in the solution), which leads to a block in the efflux of lactate, glycolysis inhibition and an eventual decrease in the intracellular pH [2]. In order to compensate for it, CMs try to eject the excess of H^+ through the Na^+/H^+ exchanger, which in turn activates the Na^+/Ca^{2+} channels, eventually leading to an accumulation of intracellular Ca^{2+} that has been associated with protease activation and increased cell death [53,54]. This aspect of the ischemic microenvironment cannot be mimicked just by removing the nutrients from the cell culture media. Indeed, the ratio of media volume to cell surface area is so high that buffers all of these changes in the extracellular pH maintaining it around 7.4, while the ischemic solution allows it to directly obtain an acidic pH of 6.4.

5.3.2 Re-establishment of normoxic conditions with media refreshment after anoxia in ischemic media causes the highest degree of cell death in hPSC-CM

Besides media composition, we also analysed the influence of oxygen tensions on hPSC-CM death (see **Fig.25,26-a,b**). We observed that the drop of oxygen levels to 0 % did not significantly increase necrotic cell death compared to normoxic (21 %) conditions when cell culture media was used, either in fully supplemented media (1.52 ± 0.12 vs 1.00 ± 0.24) or basal media without nutrients (1.96 ± 0.19 vs 1.37 ± 0.27). This can be explained because, as we previously commented, hPSC-CM have a fetal-like metabolism that relies mainly on glycolysis, which means that they do not need oxygen to produce energy [51]. On the other hand, apoptotic cell death increased in a slight but significant way, both for the fully supplemented (1.66 ± 0.14 vs 1.00 ± 0.38, $p < 0.05$) and basal media (1.57 ± 0.36 vs 0.96 ± 0.29, $p < 0.05$). This behaviour can be explained by the fact that hypoxia has been shown to induce apoptosis in a variety of ways [47,55], such as increasing the permeability of the mitochondrial membrane or stimulating the release of hypoxia-inducible factor 1 (HIF-1), which has been correlated to the overexpression of the pro-apoptotic gene BNIP3 [56].

In the case of the ischemic solution, the combined effects of hyperkalemia, acidification and oxygen deprivation led to a significant increase in hPSC-CM necrosis (4.21± 0.53 vs 3.29 ± 0.50, $p < 0.001$). In the case of apoptosis, no significant differences were observed between anoxia and normoxia (1.83 ± 0.39 vs 1.55 ± 0.36). We hypothesized that, in this case, the difference between both conditions is not significant because the low intracellular pH already increases apoptotic levels, and probably the lack of oxygen is not a sufficient stimulus to increase them further. When reperfusion is added after the anoxia, there is a significant increase in cell death in all conditions. When hPSC-CM are cultured in fully supplemented media, the necrotic death increases from 1.00 ± 0.24 to 1.96 ± 0.29 ($p < 0.05$) and the apoptosis from 1.00 ± 0.38 to 2.55 ± 0.49 ($p < 0.01$), while for the basal media without nutrients the values rise from 1.37 ± 0.27 to 2.60 ± 0.30 ($p < 0.01$) for necrosis and from 0.96 ± 0.29 to 4.02 ± 0.60 ($p < 0.0001$) for apoptosis. This drastic increase in hPSC-CMs' death is due to the burst in the production of reactive oxidative species (ROS) because of the recovery of normoxic oxygen levels. The accumulation of ROS leads to the opening of mitochondrial transition pores (MPTP) that eventually lead to a failure in ATP production and swelling of mitochondria, whose membrane eventually breaks, releasing apoptotic proteins to the cytosol [57]. This rise in cell death is even more pronounced when using the ischemic solution, with necrosis increasing from 3.29 ± 0.50 to 5.06 ± 0.95 ($p < 0.0001$) and apoptosis from 1.55 ± 0.36 to 6.34 ± 1.27 ($p < 0.0001$). This condition produces the highest level of cell death, and we believe that it is the one that better recapitulates the process occurring in the actual cardiac tissue microenvironment, in which ROS production caused by reoxygenation is combined with a normalization of the extracellular pH (from 6.4 to 7.4) that creates a gradient that has to be compensated again, leading to an intracellular calcium overload that further increase the opening of MPTP [58,59].

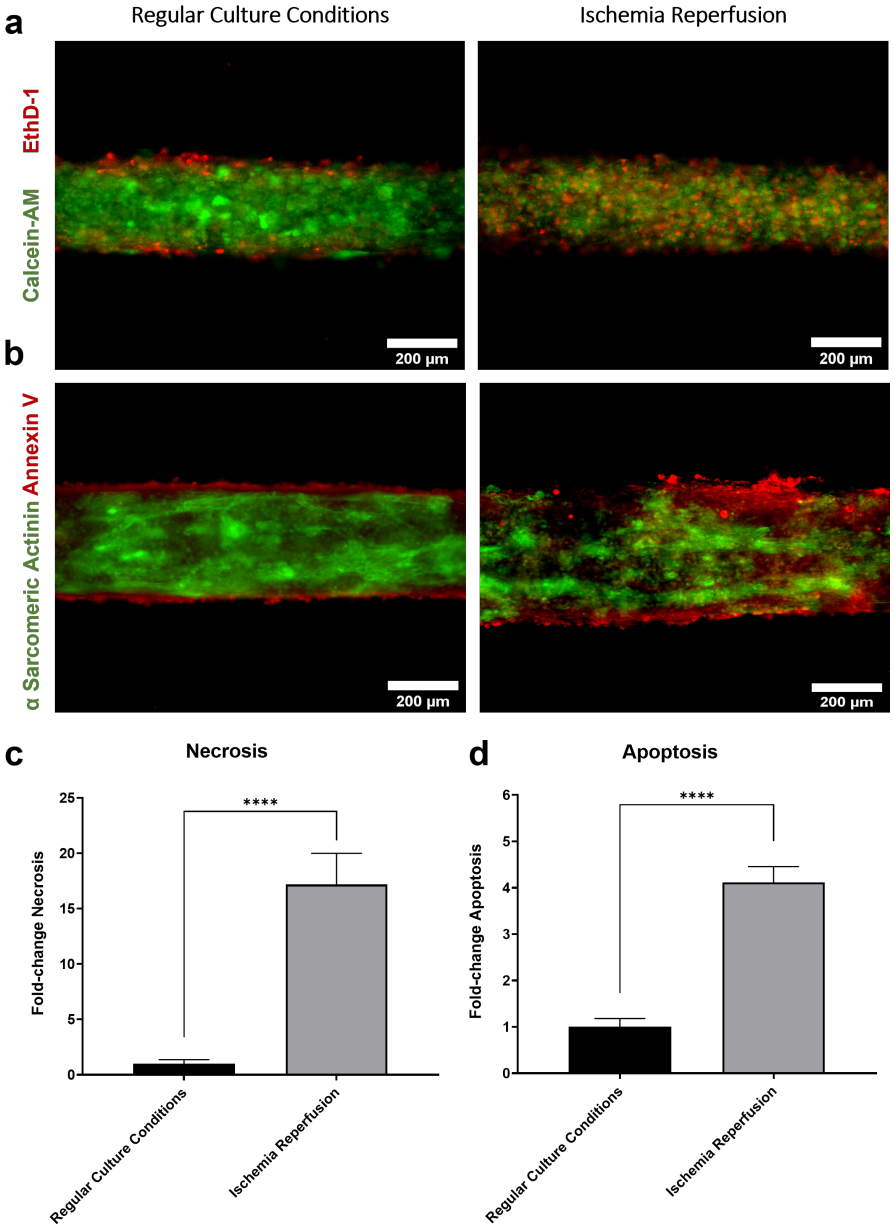

Figure 28 Evaluation of necrosis and apoptosis for 3D engineered heart tissues. (**a**) Fluorescent microscope images for a staining with calcein (green signal corresponding to live cells) and ethidium homodimer-1 (red signal corresponding to necrotic cells) of hPSC-CM co-cultured in 3D with adult CF in our microfluidic platform. (**b**) Fluorescent microscope images for α-sarcomeric actinin protein expressed by the hPSC-CM DRRGN line (green signal) and annexin V staining (red signal corresponding to apoptotic cells) of hPSC-CM co-cultured in 3D with adult CF in our microfluidic platform. Two different conditions were considered: regular culture conditions, corresponding to fully supplemented cell culture media and normoxia (21 % O_2), and ischemia-reperfusion, corresponding to a combination of the ischemic solution and anoxia (0 % O_2) for 8 h followed by a refreshment with fully supplemented media and recovery of normoxia (21 % O_2) for 2 h. Scale bar is 200 µm for all images. (**c**) Quantification of the necrosis levels as a ratio of the ethidium homodimer 1 with respect to the calcein positive area. (**d**) Quantification of the apoptosis levels as a ratio of the annexin V with respect to the α-sarcomeric actinin positive area. In both cases, data is normalized and expressed as fold-change with respect to the regular culture conditions. Results are represented as mean ± standard deviation (n = 6) with *$p < 0.05$ (evaluated with Student's t-test).

5.3.3 3D engineered cardiac tissues are more susceptible to ischemia-reperfusion injury than 2D cultures

Based on the previously described 2D experiments, we selected the conditions of culturing in anoxia (0 % O_2) with the ischemic solution followed by a return to normoxia (21 % O_2) and refreshment with fully supplemented media after 8 h as the ones that better recapitulate an IRI. We then decided to study how these conditions would affect a more realistic model based on engineered heart tissue technology (EHT), which has been widely used to obtain highly biomimetic 3D organoids of human cardiac tissue [60]. From the several strategies available to generate them, our platform is based on the compaction and self-assembly of a co-culture of hPSC-CM + hCF (suspended within a hydrogel) around flexible micropost structures that exert a passive mechanical tension that makes the cardiac cells align in a particular direction. We observed that subjecting these tissues to IRI resulted in a drastic increase in necrosis (17.17 ± 2.82 vs 1.00 ± 0.12, $p < 0.0001$), triplicating the values obtained for the 2D assay (5.06 ± 0.95) (**Fig.28-a,c**). The values for apoptosis are also significantly higher (4.11 ± 0.34 vs 1.00 ± 0.18, $p < 0.0001$), but surprisingly lower than the value obtained for the 2D assays (6.34 ± 0.52) (**Fig.28-b,d**).

We consider that the response obtained with the EHT is much more physiologically relevant, as it has been demonstrated that the maturation degree of these organoids is higher than in 2D monolayers. On the one hand, co-culture of hPSC-CM with cardiac fibroblasts in a hydrogel provides a more biomimetic environment, in terms of 3D architecture, stiffness of the substrate, matrix remodelling, and heterocellular communication that affects, for instance, the distribution of gap junction proteins and propagation of electrical signals. The results are: more synchronous and stronger contractions [61,62]. It has been also suggested that the presence of non-cardiomyocytic cells such as fibroblasts can significantly reduce apoptosis [63], which can be a possible explanation of why lower values are observed for the 3D constructs compared to the 2D monolayers, consisting only of pure hPSC-CMs. Another important factor is the passive mechanical stimulation derived from the auxotonic contractions of the tissue anchored to the microposts, which has been shown to drive tissue organization and maturation proportionally to the time in culture [64,65].

5.3.4 IRI model is able to recapitulate hallmarks of the fibrotic response

The evaluation of IRI should not only be limited to the evaluation of cell death-related phenomena but should also consider the triggering of specific hCF pathological responses to the microenvironmental changes [66]. This response is generally referred to as fibrosis and in its early phase, it is mainly featured by a phenotypic transition of quiescent hCF to myofibroblasts, a contractile cell line expressing alpha-smooth muscle cell (αSMA) protein on top of actin stress

fibres, and an unbalanced production of collagen I to generate a collagen scar in replacement of the damaged tissue [67].

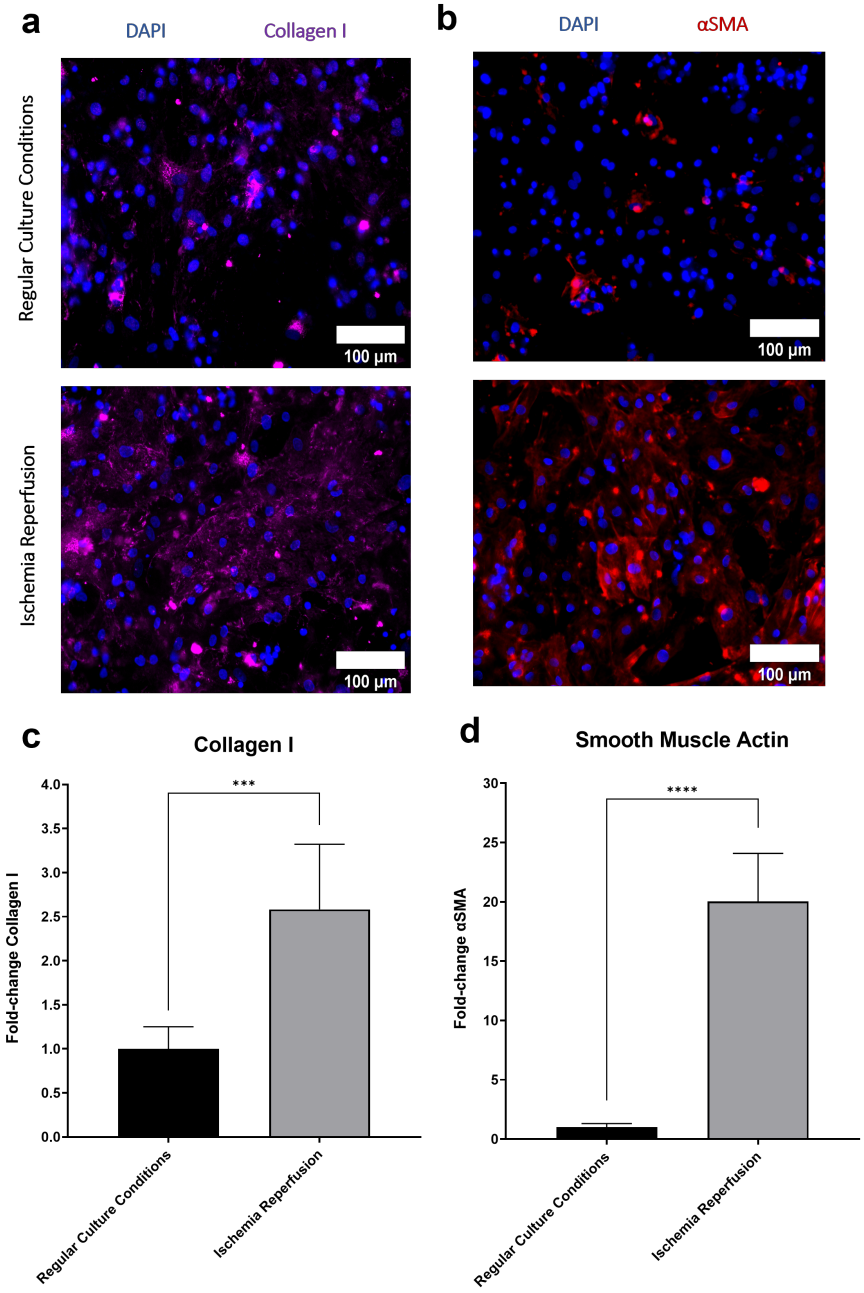

Figure 29 Evaluation of the fibrotic response for co-cultures of hPSC-CM with adult CF in 2D. (**a**) Fluorescence microscope images for the α-smooth muscle actin (red signal) and cell nuclei (blue signal) immunostaining of the co-culture of hPSC-CM with adult CF in 2D. (**b**) Fluorescence microscope images for the collagen I (purple signal) and cell nuclei (blue signal) immunostaining of the co-culture of hPSC-CM with adult CF in 2D. In both cases, two conditions were evaluated: regular culture conditions, corresponding to fully supplemented cell culture media and normoxia (21 % O_2), and ischemia-reperfusion, corresponding to a combination of the ischemic solution and anoxia (0 % O_2) followed by a refreshment with fully supplemented media and recovery normoxia (21 % O_2). Scale bar is 100 µm for all images. (**c**) Quantification of α-smooth muscle actin expression as a ratio of the positive area for this staining with respect to the number of cell nuclei. (**d**) Quantification of collagen I expression as a ratio of the positive area for

this staining with respect to the number of cell nuclei. In both cases data is normalized and expressed as fold-change with respect to the regular culture conditions. Results are represented as mean ± standard deviation (n = 6) with *p < 0.05 (evaluated with Student's t-test).

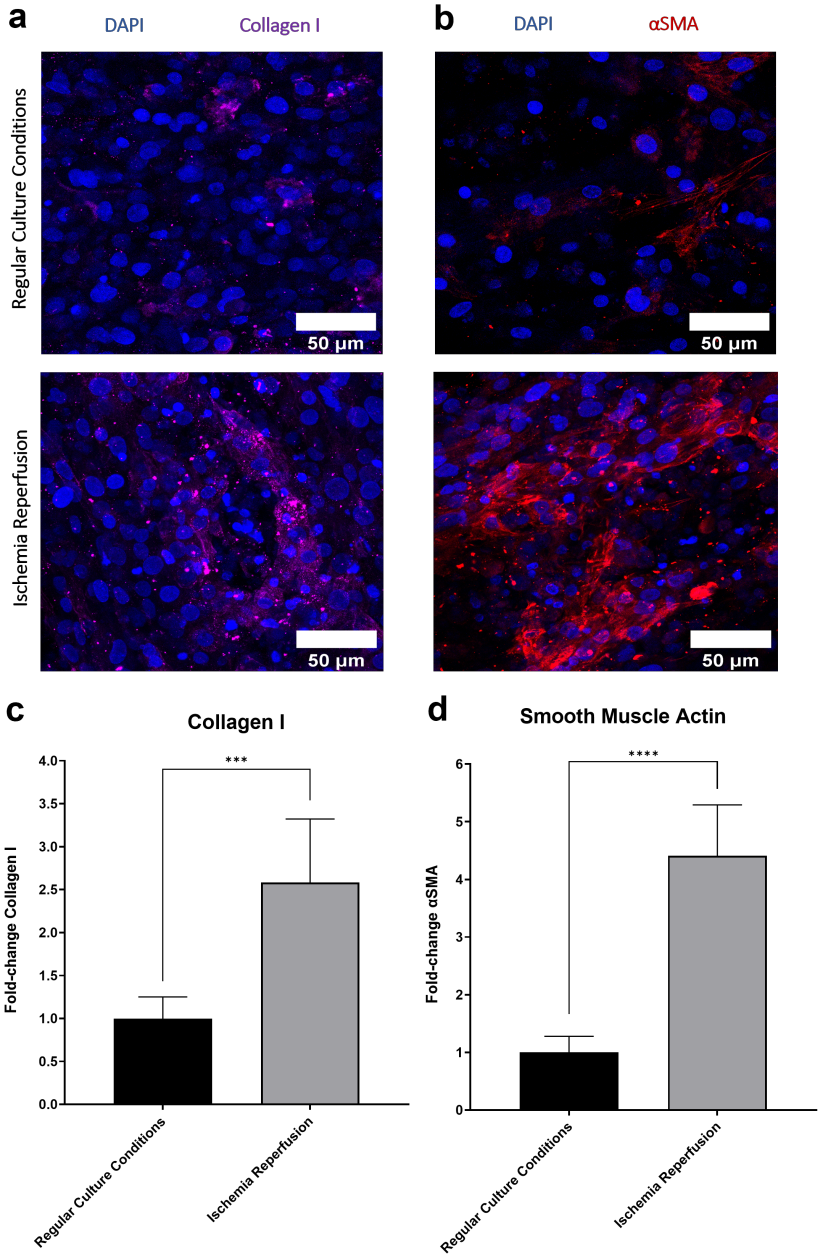

Figure 30 Evaluation of the fibrotic response for the 3D engineered heart tissues. (**a**) Fluorescence microscope images for the α-smooth muscle actin (red signal) and cell nuclei (blue signal) immunostaining of the co-culture of hPSC-CM with adult CF in 3D. (**b**) Fluorescence microscope images for the collagen I (purple signal) and cell nuclei (blue signal) immunostaining of the co-culture of hPSC-CM with adult CF in 3D. In both cases, two conditions were evaluated: regular culture conditions, corresponding to fully supplemented cell culture media and normoxia (21 % O_2), and ischemia-reperfusion, corresponding to a combination of the ischemic solution and anoxia (0 % O_2) followed by a refreshment with fully supplemented media and recovery normoxia (21 % O_2). Scale bar is 50 µm for all images. (**c**) Quantification of α-smooth muscle actin expression as a ratio of the positive area for this staining with respect to the number of cell nuclei. (**d**) Quantification of collagen I expression as a ratio of the positive area for this staining with

respect to the number of cell nuclei. In both cases data is normalized and expressed as fold-change with respect to the regular culture conditions. Results are represented as mean ± standard deviation (n = 6) with *p < 0.05 (evaluated with Student's t-test).

We first examined the expression of collagen I production in 2D assays (**Fig.29-a,c**), observing a significant increase in collagen I production (2.58 ± 0.74 vs 1.00 ± 0.25, p < 0.0001). This is in line with previous 2D in vitro assays that show that hypoxic oxygen tensions are able to upregulate the secretion of this ECM protein [68,69]. Regarding αSMA (**Fig.29-b,d**), we observed a drastic increase in its expression for the 2D cultures (20.03 ± 4.05 vs 1.00 ± 0.30, p < 0.0001) that was not reported in previous studies analysing the effect of the oxygen tension on the cardiac fibrotic response [68,70]. However, one important difference is that the hCFs used for those experiments were only subjected to hypoxia and not to the full cycle of ischemia-reperfusion, which has been suggested to drastically increase the production of TGF-β through ROS-related pathways [71,72]. This molecule is closely linked to hCF transdifferentiation to the myofibroblast lineage [73], which explains the high levels observed in our experiments.

Regarding the 3D culture experiments, a significant increase was observed for collagen I (3.30 ± 0.53 vs 1.00 ± 0.44, p < 0.0001) (**Fig.30-a,c**), which is slightly higher than in 2D cultures but around the same range. On the other hand, a significant but more moderate increase was observed in the expression of αSMA (4.41 ± 0.88 vs 1.00 ± 0.28, p < 0.0001) (**Fig.30-b,d**) compared to the 2D conditions. We believe that this increase is more physiologically relevant than the one obtained for the 2D, in which there is probably an important interactive effect of the increase in TGF-β production with the high stiffness of the substrate, which has been shown to play an important role in stimulating the differentiation towards myofibroblasts [73,74]. To the best of our knowledge, there is only one previous study that evaluated cardiac fibrosis in a 3D tissue model [70]. There, researchers also reported a significant increase in the expression of αSMA, although, as in the 2D studies, they only evaluated hypoxic conditions (1 % O_2). Overall, these results are indicative of a fibrotic response, although further experiments would be required to have a full characterization such as the analysis of hCF proliferation, the expression of different metalloproteinases (MMP-2 and MMP-3), or the secretion of inflammatory and pro-fibrotic cytokines.

5.4 Conclusions

In this work, we presented a 3D model of cardiac IRI by subjecting a 3D co-culture of hPSC-CM and adult hCF in a microfluidic-based device to a cycle of ischemia-reperfusion. The first process was characterized by culturing the cells for 8 h in anoxic conditions (0 % O2) with an ischemic solution recapitulating the acidic and hyperkalemic conditions observed in vivo. The reperfusion step was modelled by bringing back the cells to normoxic conditions (21 %) and fully

supplemented cultured media for 2 h. To select these parameters and culture conditions, we performed different 2D studies to perform a screening of the conditions that maximized cell death, both in terms of apoptosis and necrosis. We also demonstrated that our model is able to recapitulate some hallmarks of the fibrotic responses observed in vivo, namely the upregulation of αSMA (indicative of differentiation of hCF towards myofibroblasts) and collagen I deposition, both in 2D and 3D. Although further improvements should be added to increase the biomimicry of the model (such as the creation of a spatial gradient of oxygen or the incorporation of endothelial and immune cells), we believe that the presented microphysiological system can be of great use to advance preclinical cardiovascular studies focused on ischemic heart disease.

5.5 References

[1] Chen T and Vunjak-Novakovic G 2018 In vitro models of ischemia-reperfusion injury *Regen. Eng. Transl. Med.* **4** 142–153.

[2] Vaghy P L 1979 Role of mitochondrial oxidative phosphorylation in the maintenance of intracellular pH *J. Mol. Cell. Cardiol.* **11** 933–940.

[3] Robergs R A, Ghiasvand F and Parker D 2004 Biochemistry of exercise-induced metabolic acidosis *Am. J. Physiol. - Regul. Integr. Comp. Physiol.* **287** 56–63.

[4] Halestrap A P, Wang X, Poole R C, Jackson V N and Price N T 1997 Lactate transport in heart in relation to myocardial ischemia *Am. J. Cardiol.* **80** 17–25.

[5] Theroux P, Chaitman B R, Danchin N, Erhardt L, Meinertz T, Schroeder J S, Tognoni G, White H D, Willerson J T and Jessel A 2000 Inhibition of the sodium-hydrogen exchanger with cariporide to prevent myocardial infarction in high-risk ischemic situations: main results of the GUARDIAN trial *Circulation* **102** 3032–8.

[6] Marban E, Kitakaze M, Kusuoka H, Porterfield J K, Yue D T and Chacko V P 1987 Intracellular free calcium concentration measured with 19F NMR spectroscopy in intact ferret hearts *Proc. Natl. Acad. Sci. U. S. A.* **84** 6005–9.

[7] Qian T, Nieminen A L, Herman B and Lemasters J J 1997 Mitochondrial permeability transition in pH-dependent reperfusion injury to rat hepatocytes *Am. J. Physiol. - Cell Physiol.* **273** 42–56.

[8] Baines C P 2009 The mitochondrial permeability transition pore and ischemia-reperfusion injury *Basic Res. Cardiol.* **104** 181–188.

[9] Frangogiannis N G 2014 The immune system and the remodeling infarcted heart: cell biological insights and therapeutic opportunities *J. Cardiovasc. Pharmacol.* **63** 185–195.

[10] House S L, Castro A M, Lupu T S, Weinheimer C, Smith C, Kovacs A and Ornitz D M 2016 Endothelial fibroblast growth factor receptor signaling is required for vascular remodeling following cardiac ischemia-reperfusion injury *Am. J. Physiol. - Hear. Circ. Physiol.* **310** 559–571.

[11] Zymek P, Bujak M, Chatila K, Cieslak A, Thakker G, Entman M L and Frangogiannis N G 2006 The role of platelet-derived growth factor signaling in healing myocardial infarcts *J. Am. Coll. Cardiol.* **48** 2315–23.

[12] Lindsey M L, Bolli R, Canty J M, Du X J, Frangogiannis N G, Frantz S, Gourdie R G, Holmes J W, Jones S P, Kloner R A, Lefer D J, Liao R, Murphy E, Ping P, Przyklenk K, Recchia F A, Longacre L S, Ripplinger C M, Van Eyk J E and Heusch G 2018 Guidelines for experimental models of myocardial ischemia and infarction *Am. J. Physiol. - Hear. Circ. Physiol.* **314** 812–838.

[13] Negoro S, Kunisada K, Fujio Y, Funamoto M, Darville M I, Eizirik D L, Osugi T, Izumi M, Oshima Y, Nakaoka Y, Hirota H, Kishimoto T and Yamauchi-Takihara K 2001 Activation of signal transducer and activator of transcription 3 protects cardiomyocytes from hypoxia/reoxygenation-induced oxidative stress through the upregulation of manganese superoxide dismutase *Circulation* **104** 979–981.

[14] Ostadal B, Ostadalova I, Kolar F, Charvatova Z and Netuka I 2009 Ontogenetic development of cardiac tolerance to oxygen deprivation - possible mechanisms *Physiol. Res.* **58** 1–12.

[15] Ostadalova I, Ostadal B, Kolar F, Parratt J R and Wilson S 1998 Tolerance to ischaemia and ischaemic preconditioning in neonatal rat heart *J. Mol. Cell. Cardiol.* **30** 857–865.

[16] Zhu H L, Wei X, Qu S L, Zhang C, Zuo X X, Feng Y S, Luo Q, Chen G W, Liu M D, Jiang L, Xiao X Z and Wang K K 2011 Ischemic postconditioning protects cardiomyocytes against ischemia/reperfusion injury by inducing MIP2 *Exp. Mol. Med.* **43** 437–445.

[17] He X, Li S, Liu B, Susperreguy S, Formoso K, Yao J, Kang J, Shi A, Birnbaumer L and Liao Y 2017 Major contribution of the 3/6/7 class of TRPC channels to myocardial ischemia/reperfusion and cellular hypoxia/reoxygenation injuries *Proc. Natl. Acad. Sci. U. S. A.* **114** 4582–91.

[18] Bauer M, Kang L, Qiu Y, Wu J, Peng M, Chen H H, Camci-Unal G, Bayomy A F, Sosnovik D E, Khademhosseini A and Liao R 2012 Adult cardiac progenitor cell aggregates exhibit survival benefit both in vitro and in vivo *PLoS One* **7** 491-501.

[19] Canfield S G, Sepac A, Sedlic F, Muravyeva M Y, Bai X and Bosnjak Z J 2012 Marked

hyperglycemia attenuates anesthetic preconditioning in human-induced pluripotent stem cell-derived cardiomyocytes *Anesthesiology* **117** 735–744.

[20] Brodarac A, Saric T, Oberwallner B, Mahmoodzadeh S, Neef K, Albrecht J, Burkert K, Oliverio M, Nguemo F, Choi Y H, Neiss W F, Morano I, Hescheler J and Stamm C 2015 Susceptibility of murine induced pluripotent stem cell-derived cardiomyocytes to hypoxia and nutrient deprivation *Stem Cell Res. Ther.* **6** 1–19.

[21] Guo L, Abrams R M C, Babiarz J E, Cohen J D, Kameoka S, Sanders M J, Chiao E and Kolaja K L 2011 Estimating the risk of drug-induced proarrhythmia using human induced pluripotent stem cell-derived cardiomyocytes *Toxicol. Sci.* **123** 281–289.

[22] Maddaford T G, Hurtado C, Sobrattee S, Czubryt M P and Pierce G N 1999 A model of low-flow ischemia and reperfusion in single, beating adult cardiomyocytes *Am. J. Physiol. - Hear. Circ. Physiol.* **277** 46–52.

[23] Sedmera D, Kucera P and Raddatz E 2002 Developmental changes in cardiac recovery from anoxia-reoxygenation *Am. J. Physiol. - Regul. Integr. Comp. Physiol.* **283** 52–62.

[24] Portal L, Martin V, Assaly R, D'Anglemont De Tassigny A, Michineau S, Berdeaux A, Ghaleb B and Pons S 2013 A model of hypoxia-reoxygenation on isolated adult mouse cardiomyocytes: characterization, comparison with ischemia-reperfusion, and application to the cardioprotective effect of regular treadmill exercise *J. Cardiovasc. Pharmacol. Ther.* **18** 367–375.

[25] Date T, Belanger A J, Mochizuki S, Sullivan J A, Liu L X, Scaria A, Cheng S H, Gregory R J and Jiang C 2002 Adenovirus-mediated expression of p35 prevents hypoxia/reoxygenation injury by reducing reactive oxygen species and caspase activity *Cardiovasc. Res.* **55** 309–319.

[26] Liao R, Podesser B K and Lim C C 2012 The continuing evolution of the Langendorff and ejecting murine heart: new advances in cardiac phenotyping *Am. J. Physiol. - Hear. Circ. Physiol.* **303** 156-167.

[27] Bell R M, Mocanu M M and Yellon D M 2011 Retrograde heart perfusion: the Langendorff technique of isolated heart perfusion *J. Mol. Cell. Cardiol.* **50** 940–950.

[28] Sutherland F J and Hearse D J 2000 The isolated blood and perfusion fluid perfused heart *Pharmacol. Res.* **41** 613–627.

[29] Neely J R, Liebermeister H, Battersby E J and Morgan H E 1967 Effect of pressure development on oxygen consumption by isolated rat heart *Am. J. Physiol.* **212** 804–814.

[30] Steenbergen C, Perlman M E, London R E and Murphy E 1993 Mechanism of

preconditioning: ionic alterations *Circ. Res.* **72** 112–125.

[31] Galaup A, Gomez E, Souktani R, Durand M, Cazes A, Monnot C, Teillon J, Le Jan S, Bouleti C, Briois G, Philippe J, Pons S, Martin V, Assaly R, Bonnin P, Ratajczak P, Janin A, Thurston G, Valenzuela D M, Murphy A J, Yancopoulos G D, Tissier R, Berdeaux A, Ghaleb B and Germain S 2012 Protection against myocardial infarction and no-reflow through preservation of vascular integrity by angiopoietin-like 4 *Circulation* **125** 140–149.

[32] Gharacholou S M, Alexander K P, Chen A Y, Wang T Y, Melloni C, Gibler W B, Pollack C V., Ohman E M, Peterson E D and Roe M T 2010 Implications and reasons for the lack of use of reperfusion therapy in patients with ST-segment elevation myocardial infarction: findings from the CRUSADE initiative *Am. Heart J.* **159** 757–763.

[33] Heusch G, Libby P, Gersh B, Yellon D, Bohm M, Lopaschuk G and Opie L 2014 Cardiovascular remodelling in coronary artery disease and heart failure *Lancet* **383** 1933–43.

[34] Heusch G 2016 The coronary circulation as a target of cardioprotection *Circ. Res.* **118** 1643–58.

[35] Michael L H, Entman M L, Hartley C J, Youker K A, Zhu J, Hall S R, Hawkins H K, Berens K and Ballantyne C M 1995 Myocardial ischemia and reperfusion: a murine model *Am. J. Physiol. - Hear. Circ. Physiol.* **269** 38–46.

[36] Michael L H, Ballantyne C M, Zachariah J P, Gould K E, Pocius J S, Taffet G E, Hartley C J, Pham T T, Daniel S L, Funk E and Entman M L 1999 Myocardial infarction and remodeling in mice: effect of reperfusion *Am. J. Physiol. - Hear. Circ. Physiol.* **277** 46–52.

[37] Heusch G, Skyschally A and Schulz R 2011 The in-situ pig heart with regional ischemia/reperfusion - ready for translation *J. Mol. Cell. Cardiol.* **50** 951–63.

[38] Ma Y, Iyer R P, Jung M, Czubryt M P and Lindsey M L 2017 Cardiac fibroblast activation post-myocardial infarction: current knowledge gaps *Trends Pharmacol. Sci.* **38** 448–458.

[39] Jung M, Ma Y, Iyer R P, DeLeon-Pennell K Y, Yabluchanskiy A, Garrett M R and Lindsey M L 2017 IL-10 improves cardiac remodeling after myocardial infarction by stimulating M2 macrophage polarization and fibroblast activation *Basic Res. Cardiol.* **112** 622-648.

[40] Francis Stuart S D, De Jesus N M, Lindsey M L and Ripplinger C M 2016 The crossroads of inflammation, fibrosis, and arrhythmia following myocardial infarction *J. Mol. Cell. Cardiol.* **91** 114–122.

[41] Klotz L, Norman S, Vieira J M, Masters M, Rohling M, Dube K N, Bollini S, Matsuzaki F, Carr C A and Riley P R 2015 Cardiac lymphatics are heterogeneous in origin and

respond to injury *Nature* **522** 62–67.

[42] Mayorga M, Kiedrowski M, Shamhart P, Forudi F, Weber K, Chilian W M, Penn M S and Dong F 2016 Early upregulation of myocardial CXCR4 expression is critical for dimethyloxalylglycine-induced cardiac improvement in acute myocardial infarction *Am. J. Physiol. - Hear. Circ. Physiol.* **310** 20–28.

[43] Whittaker P, Kloner R A, Boughner D R and Pickering J G 1994 Quantitative assessment of myocardial collagen with picrosirius red staining and circularly polarized light *Basic Res. Cardiol.* **89** 397–410.

[44] O'Hara T and Rudy Y 2012 Quantitative comparison of cardiac ventricular myocyte electrophysiology and response to drugs in human and nonhuman species *Am. J. Physiol. - Hear. Circ. Physiol.* **302** 1023-30.

[45] Gibbs C L 2003 Cardiac energetics: sense and nonsense *Clin. Exp. Pharmacol. Physiol.* **30** 598–603.

[46] Ribeiro M C, Slaats R H, Schwach V, Rivera-Arbelaez J M, Tertoolen L G J, van Meer B J, Molenaar R, Mummery C L, Claessens M M A E and Passier R 2020 A cardiomyocyte show of force: A fluorescent alpha-actinin reporter line sheds light on human cardiomyocyte contractility versus substrate stiffness *J. Mol. Cell. Cardiol.* **141** 54–64.

[47] Tanaka M, Ito H, Adachi S, Akimoto H, Nishikawa T, Kasajima T, Marumo F and Hiroe M 1994 Hypoxia induces apoptosis with enhanced expression of Fas antigen messenger RNA in cultured neonatal rat cardiomyocytes *Circ. Res.* **75** 426–433.

[48] Chen T and Vunjak-Novakovic G 2019 Human Tissue-Engineered Model of Myocardial Ischemia-Reperfusion Injury *Tissue Eng. Part A* **25** 711–724.

[49] Hidalgo A, Glass N, Ovchinnikov D, Yang S K, Zhang X, Mazzone S, Chen C, Wolvetang E and Cooper-White J 2018 Modelling ischemia-reperfusion injury (IRI) in vitro using metabolically matured induced pluripotent stem cell-derived cardiomyocytes *APL Bioeng.* **2** 102-116.

[50] Schindelin J, Arganda-Carreras I, Frise E, Kaynig V, Longair M, Pietzsch T, Preibisch S, Rueden C, Saalfeld S, Schmid B, Tinevez J Y, White D J, Hartenstein V, Eliceiri K, Tomancak P and Cardona A 2012 Fiji: an open-source platform for biological-image analysis *Nat. Methods 2012 97* **9** 676–82.

[51] Ulmer B M and Eschenhagen T 2020 Human pluripotent stem cell-derived cardiomyocytes for studying energy metabolism *Biochim. Biophys. Acta. Mol. Cell Res.* **1867** 471-482.

[52] Fajardo V M, Feng I, Chen B Y, Perez-Ramirez C A, Shi B, Clark P, Tian R, Lien C L, Pellegrini M, Christofk H, Nakano H and Nakano A 2021 GLUT1 overexpression enhances glucose metabolism and promotes neonatal heart regeneration *Sci. Reports 2021 111* **11** 1–12.

[53] Coles J G, Boscarino C, Takahashi M, Grant D, Chang A, Ritter J, Dai X, Du C, Musso G, Yamabi H, Goncalves J, Kumar A S, Woodgett J, Lu H and Hannigan G 2005 Cardioprotective stress response in the human fetal heart *J. Thorac. Cardiovasc. Surg.* **129** 1128-36.

[54] Li Y-Z, Lu D-Y, Tan W-Q, Wang J-X and Li P-F 2008 p53 Initiates Apoptosis by Transcriptionally Targeting the Antiapoptotic Protein ARC *Mol. Cell. Biol.* **28** 564–74.

[55] Greijer A E and Van Der Wall E 2004 The role of hypoxia inducible factor 1 (HIF-1) in hypoxia induced apoptosis *J. Clin. Pathol.* **57** 1009-14.

[56] Guo K, Searfoss G, Krolikowski D, Pagnoni M, Franks C, Clark K, Yu K T, Jaye M and Ivashchenko Y 2001 Hypoxia induces the expression of the pro-apoptotic gene BNIP3 *Cell Death Differ. 2001 84* **8** 367–76.

[57] Raedschelders K, Ansley D M and Chen D D Y 2012 The cellular and molecular origin of reactive oxygen species generation during myocardial ischemia and reperfusion *Pharmacol. Ther.* **133** 230–55.

[58] Griffiths E J and Halestrap A P 1995 Mitochondrial non-specific pores remain closed during cardiac ischaemia, but open upon reperfusion. *Biochem. J.* **307** 93-98.

[59] Kalogeris T, Baines C P, Krenz M and Korthuis R J 2012 Cell biology of ischemia/reperfusion injury *Int. Rev. Cell Mol. Biol.* **298** 229–317.

[60] Tzatzalos E, Abilez O J, Shukla P and Wu J C 2016 Engineered heart tissues and induced pluripotent stem cells: Macro- and microstructures for disease modeling, drug screening, and translational studies *Adv. Drug Deliv. Rev.* **96** 234–244.

[61] Hall C, Gehmlich K, Denning C and Pavlovic D 2021 Complex Relationship Between Cardiac Fibroblasts and Cardiomyocytes in Health and Disease *J. Am. Heart Assoc.* **10** 1–15.

[62] Doppler S A, Carvalho C, Lahm H, Deutsch M A, Dreßen M, Puluca N, Lange R and Krane M 2017 Cardiac fibroblasts: more than mechanical support *J. Thorac. Dis.* **9** 36–51.

[63] Guo F, Zhang C C, Yin X H, Li T, Fang C H and He X B 2020 Crosstalk between cardiomyocytes and noncardiomyocytes is essential to prevent cardiomyocyte apoptosis

induced by proteasome inhibition *Cell Death Dis. 2020 119* **11** 1–13.

[64] Feric N T and Radisic M 2016 Maturing human pluripotent stem cell-derived cardiomyocytes in human engineered cardiac tissues *Adv. Drug Deliv. Rev.* **96** 110–34.

[65] Ruan J L, Tulloch N L, Saiget M, Paige S L, Razumova M V., Regnier M, Tung K C, Keller G, Pabon L, Reinecke H and Murry C E 2015 Mechanical Stress Promotes Maturation of Human Myocardium From Pluripotent Stem Cell-Derived Progenitors *Stem Cells* **33** 2148–57.

[66] Shinde A V. and Frangogiannis N G 2014 Fibroblasts in myocardial infarction: a role in inflammation and repair *J. Mol. Cell. Cardiol.* **70** 74–82.

[67] Baum J and Duffy H S 2011 Fibroblasts and myofibroblasts: what are we talking about? *J. Cardiovasc. Pharmacol.* **57** 376–379.

[68] Ugolini G S, Pavesi A, Rasponi M, Fiore G B, Kamm R and Soncini M 2017 Human cardiac fibroblasts adaptive responses to controlled combined mechanical strain and oxygen changes in vitro *Elife* **6** 847-867.

[69] Tamamori M, Ito H, Hiroe M, Marumo F and Hata R I 1997 Stimulation of collagen synthesis in rat cardiac fibroblasts by exposure to hypoxic culture conditions and suppression of the effect by natriuretic peptides *Cell Biol. Int.* **21** 175–80.

[70] Veldhuizen J, Chavan R, Moghadas B, Park J G, Kodibagkar V D, Migrino R Q and Nikkhah M 2022 Cardiac ischemia on-a-chip to investigate cellular and molecular response of myocardial tissue under hypoxia *Biomaterials* **281** 336-350.

[71] Flores-Vergara R, Olmedo I, Aránguiz P, Riquelme J A, Vivar R and Pedrozo Z 2021 Communication between cardiomyocytes and fibroblasts during cardiac ischemia/reperfusion and remodeling: roles of TGF-β, CTGF, the renin angiotensin axis, and non-coding RNA molecules *Front. Physiol.* **12** 721-737.

[72] Frangogiannis N G 2017 The role of transforming growth factor (TGF)-β in the infarcted myocardium *J. Thorac. Dis.* **9** 52–63.

[73] Elson E L, Qian H, Fee J A and Wakatsuki T 2019 A model for positive feedback control of the transformation of fibroblasts to myofibroblasts *Prog. Biophys. Mol. Biol.* **144** 30–40.

[74] Zhao H, Li X, Zhao S, Zeng Y, Zhao L, Ding H, Sun W and Du Y 2014 Microengineered in vitro model of cardiac fibrosis through modulating myofibroblast mechanotransduction *Biofabrication* **6** 450-461.

6

General Conclusions

During this PhD dissertation, we have put forward three different microphysiological systems architectures, based on the combination of microfluidic technology with cell culturing, to provide relevant models of complex tissue processes (mainly bone vascularization and cardiac ischemia-reperfusion). This research effort was motivated by the lack of adequate preclinical models to study complex regeneration processes with instructive biomaterials, as traditional *in vitro* models are generally too simplistic to recapitulate complex interactions taking place in the real cell microenvironment (mechanical and electrical cues, spatial distribution, etc.) and the *in vivo* counterparts are complex, expensive, genetically different from humans and ethically questionable.

In **chapter 3** we presented a novel 3D microfluidic assay that allows us to study the effect of soluble cues (such as ions or proteins) released by bioactive biomaterials in the recruitment of EPC, a key step in the overall vascularization process of a biomaterial. We showed a proof of concept of the device for bone regeneration applications, using a co-culture environment with BM-MSC and rigid calcium-releasing scaffolds based on electrospun fibers. We showed using finite element modelling supported with experimental validation that the presented microfluidic device can be used to generate gradients of ions (such as calcium) or growth factors (such as VEGF or osteopontin) either dissolved in the media or released from supporting stromal cells cultured in a separate chamber. We evaluated the biological relevance of the gradients generated in the device by studying the effects of dissolved calcium in the media (10 mM) on the proliferation and migration of rat bone marrow-derived EPC and MSC in 3D. We showed that this ion is able to stimulate both processes in the latter case while it has no apparent effect on the first cell type.

After this, we demonstrated that our device can be used to evaluate the different responses of rEPC to calcium-releasing scaffolds in a co-culture microenvironment with BM-rMSC. We compared an electrospun composite made of PLA with calcium phosphates nanoparticles with a regular PLA control, showing that the first one elicited a higher migratory response on the rEPC and the upregulation of several pro-inflammatory and pro-angiogenic proteins. These results are in good agreement with previous *in vivo* observations obtained with this composite material in our group. We further used the platform to study the effects of the bone sialoprotein osteopontin (OPN) on the rEPC migratory response in a co-culture environment with BM-rMSC. Our results suggest that this protein has an important role in mediating EPC recruitment to a calcium-rich microenvironment, as its neutralization drastically reduced this response. Overall, we believe that the presented assay could be of great interest to the tissue engineering community as a platform to study the optimal strategy to stimulate endothelial cell recruitment in bone biomaterials. Future work should focus on the incorporation of perfusion in the device, to improve cell function and viability in long term cultures, as well as allowing to maintain a stable gradient over time, something that cannot be achieved with the current approach. Moreover, a more physiologically relevant human model should be developed using iPSC-derived endothelial cells in combination with mesenchymal stem cells or osteoblasts cultured in a stiffer matrix that better recapitulates the bone tissue environment (for instance combining fibrin with hydroxyapatite).

In **chapter 4,** we presented a microfluidic system to generate highly biomimetic cardiac tissues in 2D by combining topographical and electrical cues in a low cost and easy to use platform. We presented a method to nanopattern the substrate of the chips by depositing PLA electrospun fibers on glass coverslips and showed how we can control the cell anisotropy on the chip depending on the spatial orientation of the fibers during deposition. We also introduced a simple, cost effective method to incorporate electrical stimulation in the platform using biocompatible stainless steel rod electrodes. We provided an experimentally validated finite element analysis of electrical field to show that it is possible to obtain comparable results to gold standard approach that uses a much more complex and expensive method based on metal deposition on the substrate. We co-cultured neonatal mouse CM and CF in the platform and stimulated them with this electrode configuration, showing that higher maturation levels can be attained in terms of higher expression of the tight junction protein Cx-43, as well as the upregulation of several key genes involved in conductive and structural cardiac properties. Future work on this platform should focus on changing the material of the electrospun fibers from stiff PLA to a more compliant substrate such as collagen in order to prevent excessive CF proliferation and allow for a higher degree of CM contraction and matrix remodelling, which would result in higher mechanical stimulation and maturation levels.

Finally, in **chapter 5** we presented an innovative model of cardiac IRI using a novel microfluidic architecture to co-culture hPSC-CM and primary hCF in 3D. A preliminary study was performed using 2D monolayers of hPSC-CM to establish the best environmental conditions in terms of media composition and cycle of oxygen tensions to generate biomimetic levels of IRI-associated cell death. We showed that culturing these cells in anoxic conditions (0 % O_2) for 8 h in combination with an ischemic solution that replicates the acidic and hyperkalemic conditions of the ischemic heart before going back to normoxic conditions produces the highest levels of necrosis and apoptosis. These results were validated using 3D cardiac organoids obtained by the self-assembling of a co-culture of hPSC-CM with hCF in a fibrin-based hydrogel around micropost structures. This resulted in even higher levels of cell death, probably due to the increased maturity of these constructs caused by the 3D architecture and passive mechanical stimulation resulting from the auxotonic tissue contractions against microposts. Finally, we also characterized the response of cardiac fibroblasts to IRI in both 2D and 3D configurations. We were able to observe a significant increase in the expression of α-smooth muscle actin and collagen I deposition, two hallmark markers of the fibrotic response *in vivo*. Future work should be mainly focused on implementing a microfluidic circuit that would allow producing a gradient of oxygen tensions from physiological (6 % O_2 for cardiac tissue) to hypoxic (< 1% O_2) levels within the same tissue instead of relying on whole tissue oxygen changes as in the current platform. This could be achieved for instance by implementing two extra channels in the platform, one to flow liquid (PBS for instance) at normoxic tensions while in the other we would use an oxygen scavenger (such as sodium sulfite) dissolved in that same liquid. Another possible improvement would be to better characterize the fibrotic response by analyzing more cell mechanisms such as increased cell proliferation, secretion of pro-inflammatory factors and expression of metalloproteinases.